Optimal Design of Medical Illuminants Spectrum for Observation of Blood Circulation Status

February 2021

Yoko Kurabuchi

Graduate School of Science and Engineering

CHIBA UNIVERSITY

(千葉大学審査学位論文)

Optimal Design of Medical Illuminants Spectrum for Observation of Blood Circulation Status

February 2021

Yoko Kurabuchi

Graduate School of Science and Engineering

CHIBA UNIVERSITY

Contents

Chapter 1 Introduction

This chapter describes the background, basic theory for the thesis, and the objective of the study. Section 1.1 introduces visual diagnosis during surgery, the way to optimize surgical illuminant, and the study's target spectral characteristics. In Section 1.2 capturing method and metamerism are shown. Absorbing substances in organisms, especially oxyhemoglobin and deoxyhemoglobin, are explained in Section 1.3. Finally, the structure of this thesis is given in Section 1.4.

1.1 Background

1.1.1 Visual diagnosis during surgery

In open surgery, identification of the site of interest and diagnosis of its conditions by visual inspection are essential factors for a successful surgery. For example, it is necessary to determine blood vessel structures, nerve crossings, and organ blood circulations during surgery. However, it is difficult to distinguish these areas because the color differences between the target region and the surrounding region are subtle. Recently, spectral analysis has used for these purposes [1-5]. Spectral reflectance refers to the spectral characteristics of an object, and it provides color information that is difficult to detect by the naked eye. In particular, spectral reflectance analysis using reflected light is expected to be utilized in the medical fields because of its non-contact capability. The use of a hyperspectral camera is an effective way of acquiring spectral information. A hyperspectral camera is an instrument that can acquire spectral images. The improvement of surgical precision using the target region's detailed spectral information by using spectral images has conducted. However, hyperspectral cameras are expensive, and the imaging system is too large to conduct surgical procedures. In addition, the lack of real-time imaging makes it challenging to use in surgical procedures.

1.1.2 Optimization of surgical illuminant

We focused on illumination because it is the only device we can modify to improve visual observation process during surgery. Generally, a conventional surgical illuminant has halogen light sources, but recently they have been replaced by white light emitting diodes (LEDs). However, the light sources are selected based on the similarity of the

color to the sunlight. Since these light sources used currently have broadband spectrum characteristics, surgical illuminants have still room for improvement of spectral design. Therefore, illumination spectrum design for magnifying subtle color differences is essential for supporting the visual diagnosis. The human recognizes color information by capturing reflected light from the target samples and processing these stimuli in brain (Figure 1.1). The degree of light reflection at each wavelength is called spectral reflectance, a physical specific property to each object. In this study, we designed an optimal illuminant spectrum that can enhance the slight color difference.

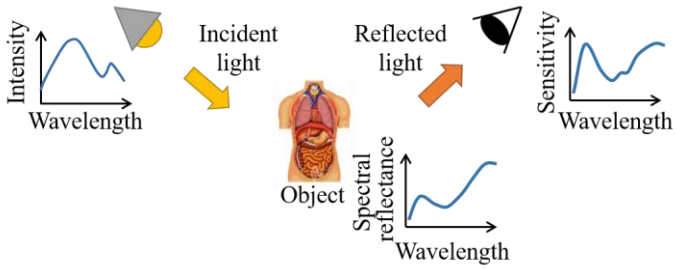

Figure 1.1: Color recognition system

First, we focused on the illuminant spectra for visual diagnosis by using illuminant metamerism. Illuminant metamerism is a phenomenon caused by human visual characteristics. Since the human vision mechanism uses only three spectral cones to perceive colors, there can exist innumerable light spectra that give us similar color perception. Therefore, we apply illuminant metamerism to realize an illuminant spectrum. The desired illuminant spectrum is the one that provides observers with color perception equivalent to the conventional illuminant and at the same time enhances slight color differences of target objects. This study focused on the utilization of LEDs which has various types of peak wavelength in the visible range. Compared with conventional halogen surgical illuminant, LED illuminants' spectra have narrower spectral band. We designed illuminant spectra by combining these LEDs to optimize them. Prior research projects have designed optimal illuminant spectra by computer simulation [6-11]. However, these studies have limitations because the evaluation has not been conducted in the actual clinical environment. In [12-16], the spectrally tunable light source that enables various kinds of illuminant spectral distributions was constructed. The system was developed to examine illuminants through quantitative measurement of color differences and subjective evaluations. Since these research projects focused only on the tissue characteristics, the evaluations for diseases or health conditions are not enough to introduce these systems in clinical fields.

Second, we developed a camera-illuminant combined system for the quantitative

evaluation of spectral characterization. Since color cameras generally have only three color channel sensors (red, green, blue), color information of these cameras is limited. Therefore, we focused on the system design, because even with a color camera, we can acquire detailed spectral characteristics with optimally designed illuminant spectra.

Target of the study

In this research, we first set organ blood circulation as an optimization target. We focused on the gastrointestinal surgery, especially its reconstruction procedures using small intestine or other parts of organs. This technique is a procedure in which a diseased region is resected, and healthy organs are transplanted into the region. In this case, blood circulation status of the transplanted organ and anastomosis part between the transplanted organ and the surrounding area can affect the patient's prognosis. When the condition of blood circulation becomes poor, blood flow is congested by oxygenated hemoglobin (HbO_2) and deoxygenated hemoglobin (Hb). The color of poor circulation part in organ turns darker compared with that of healthy part. However, since the color changes due to poor blood circulation are subtle, it is difficult to visually judge the status, and decision depends on the surgeon's experience and subjectivity.

Besides, we have also conducted narrow-band illuminant observation for vascular structure enhancement. Similar to the optimal illuminant for blood circulation, the illuminant color was limited to white. Skin flap necrosis was selected as a target of this study. Skin flap surgery is a plastic surgery technique that uses skin and subcutaneous tissue with blood flow in the defective area due to injury or reconstruction caused by surgery. The surgery involves vascular anastomosis between the grafted skin flap and the target region and inadequate anastomosis of the grafted skin flap can cause necrosis of the region. We designed and evaluated a light source for the early detection of necrotic regions for visual diagnosis. Moreover, we developed a color camera-illuminant combined system for early detection of necrosis.

1.2 Spectral characteristic and basic theory

1.2.1 Spectral reflectance measurement

Spectral reflectance is a physical property of an object surface, represented in ratio of reflected light to incident light for each wavelength. Since spectral reflectance is material-specific, the color appearance of objects depends on the spectral reflectance, spectral characteristics of the illuminant, and observation direction. Figure 1.2 shows the spectral reflectance measurement system. In general, spectral reflectance is

measured using a measuring device capable of acquiring spectral characteristics by calculating the ratio of the reflected light to the incident light [17].

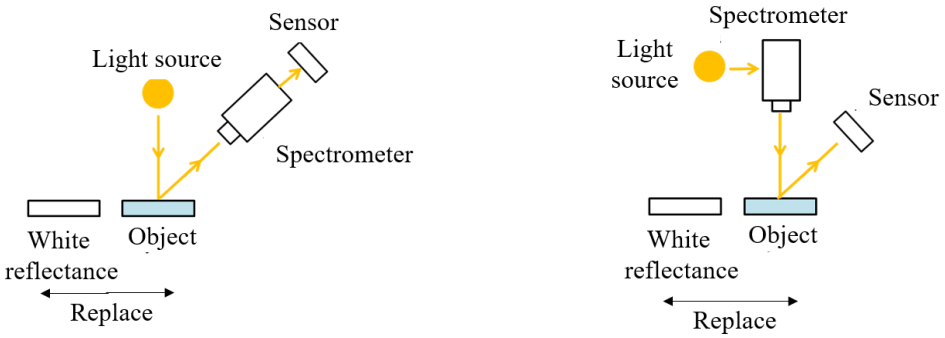

(a) (b)

Figure 1.2: Spectral reflectance measurement: overview.

The same spectral reflectance values are captured by these measurement settings shown in Figure 1.2 (a) and (b) if the target samples are non-fluorescent materials. In the measurement step, after a standard white reflector and an object are measured, $\rho_w(\lambda)$, $\rho_o(\lambda)$ values proportional to the spectral radiance is obtained. If the spectral reflectance of a standard white reflector is set to $S_w(\lambda)$, the object's spectral reflectance $S_O(\lambda)$ is shown in (1-1):

$$S_O(\lambda) = S_S(\lambda)\frac{\rho_o(\lambda)}{\rho_w(\lambda)}. \qquad (1\text{-}1)$$

Since spectral reflectance depends on the positional relationship between the incident light and the reflected light from the object, CIE (Commission international del'eclairage) has guideline on measuring a reflective object. According to its guideline, it is recommended to define an illuminant and light-receiving system for comparing values to each other [14]. Figure 1.3 shows the four geometric systems for spectral reflectance measurement. In the setting of Figure1.3 (c) and (d), a shading plate prevents irradiation and reflection light from light source.

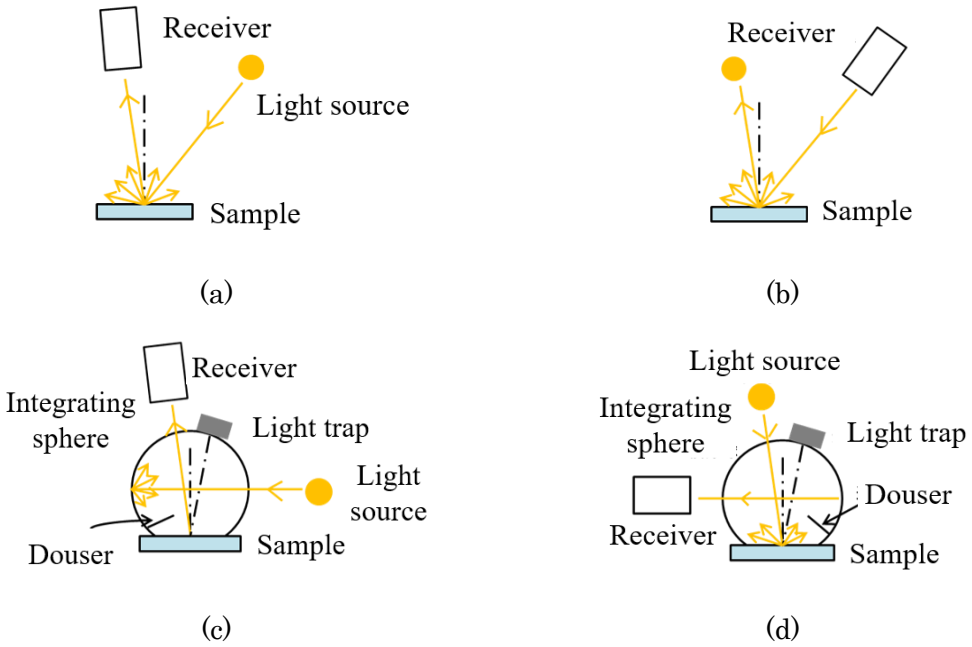

Figure 1.3: Geometric conditions for measuring a reflective object: (a) (45°/0) light illuminating direction makes 45° ± 2 angle and the reflected light receiving directing makes angle 10° or less with the normal of the object surface. (b) (0/45°) Illumination angle is 10 degrees or less and the reflection angle is 45 ± 2 degree, both with the normal of the object surface. (c) (d/0) The object is diffusely irradiated by incident light and received reflected light at an angle of 10 degrees or less relative to the normal of the object surface. (d) (0/d) Illuminant is irradiated normal to the object sample, and an integrating sphere collects the reflected light.

1.2.2 Metamerism

The human acquires visual information by accepting reflected light, a product of illuminant distribution, and the spectral reflectance of objects. The color information is perceived by stimuli obtained in three types of cones, R cone, M cone, and S cone. Therefore, the color information is changed by illuminant distribution $E(\lambda)$ and spectral reflectance $R(\lambda)$. The XYZ color system is expressed by the following equation(1-2):

$$\begin{aligned} X &= \int \overline{x(\lambda)} E(\lambda) R(\lambda) d\lambda \\ Y &= \int \overline{y(\lambda)} E(\lambda) R(\lambda) d\lambda \\ Z &= \int \overline{z(\lambda)} E(\lambda) R(\lambda) d\lambda \end{aligned} \qquad (1\text{-}2)$$

Here $\overline{x(\lambda)}$, $\overline{y(\lambda)}$, $\overline{z(\lambda)}$ are the isochromatic functions defined by CIE, and $R(\lambda)$ is the spectral

reflectance of the target region. If these stimuli have the same value, we perceived it as the same color. However, since these values are represented as three components: isochromatic functions, the illuminant distribution, and sample reflectance, some combinations of these values may be perceived as the same color stimuli even though their properties are not the same. These phenomena are called metamerism. There are four types of metamerism: illumination metamerism, object color metamerism, geometric metamerism, and observer metamerism. Illumination metamerism is a phenomenon in which objects with two different spectral reflectance appears to have same color under certain lighting condition. Object color metamerism is a phenomenon in which a certain spectral reflectance combination produces the same color perception. Geometric metamerism is a phenomenon that occurs when spectral reflectance is not constant with an illuminant distribution. Observer metamerism occurs when the sensitivity characteristics of the observers' vision are different.

1.3 Absorbing substances in organism

1.3.1 Absorption characteristics of Hemoglobin and deoxygenated hemoglobin

Oxygen is essential for metabolism that takes place in the cells of the body. Humans take in oxygen through respiration in lung, dissolve oxygen into blood, and release carbon dioxide in alveoli. Red blood cells (RBCs), one of the blood's antibiotics, play a part in carrying oxygen into the body. One of the principal components of RBCs is hemoglobin. We call oxygenated hemoglobin (HbO_2), combined with oxygen and deoxygenated hemoglobin (Hb) [18]. Absorption characteristic of HbO_2 and Hb causes high oxygen saturation; blood color is bright red, and low oxygen saturation blood color is dark red. Figure 1.4 shows the absorption coefficient of Hb and HbO_2. HbO_2 and Hb have isosbestic points around 450 nm and 525 nm, and there are significant differences between 450-520 nm and 580-800 nm. These differences cause differences in organ color changes due to the oxygen saturation level. Therefore, these characteristics allow optimal illuminant to use a difference in the spectral characteristic of organ.

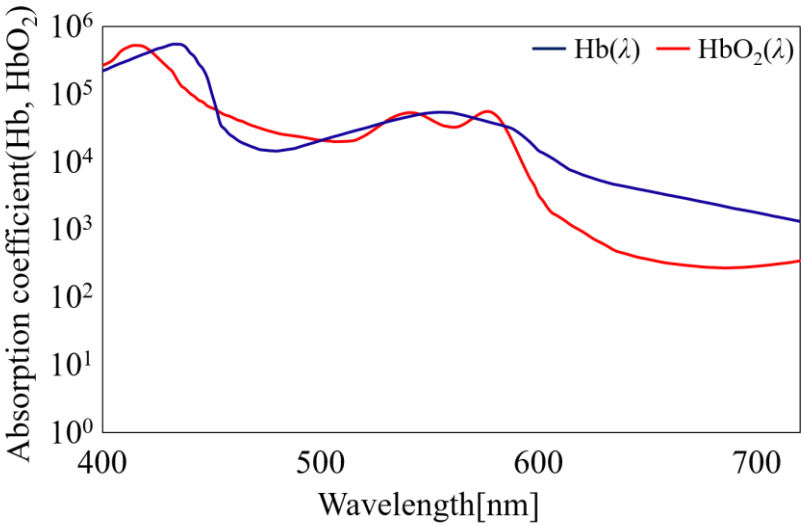

Figure 1.4: Absorption coefficient of Hb and HbO_2

1.3.2 Congestion and ischemia

Various factors may contribute to poor blood circulation but they can be divided into two categories: congestion and ischemia. Congestion is a condition that occurs when drainage of blood has some problems, and low oxygen saturation blood accumulates in the tissue. In contrast, ischemia is inhibited blood flow status due to a decrease in arterial blood flow. These conditions must be detected and treated as early as possible because of their harmful tissue affects.

1.4 Structure of this thesis

The thesis is structured with the contents as follows:

- Our developed illuminant device, a spectrally tunable light source that can produce multiple spectral distributions for evaluation experiment for optimally designed illuminant spectra, is described in Chapter 2.

- To evaluate the effectiveness of the optimal illuminants, we used animal models to construct blood circulation conditions. We used the rat blood blocked model and skin flap necrosis model described in Chapter 3.

- As the first target for the optimal illuminant, the organ's blood circulation model is explained in Chapter 4.

- Chapter 5 presents the blood vessel structure as second target for the optimal illuminant.

- We focused on a camera-illuminant combined system as a developing verification. The model of skin flap necrosis was set as a target of the optimization. The detail of this topic is described in Chapter 6.

- Finally, concluding remarks and future works are given in Chapter 7.

Chapter 2 Spectrally tunable light source and basic optimal illuminant design method

In this research, we developed the spectrally tunable light source to clarify the effectiveness of optimal illuminants. As shown in Chapter 1, the spectrally tunable light source is the lighting device that can irradiate multiple patterns of illuminant to target regions. This device allows us to reproduce simulated illuminant spectra for verifications of experimental environments. There are some research projects involving spectrally tunable light source by using a digital micro mirror device [19], or light emitting diodes (LEDs) [20-27].

To construct the device that can reproduce variable light distributions, we focused on LEDs. In this chapter, LED devices that were used in this system are described in Section 2.1. Section 2.2 shows the device controlling system. The prototype system developments are explained in Sections 2.3 and 2.4, respectively. In Section 2.5, the basic theory of the optimization method is described.

2.1 LED devices

To irradiate the calculated optimal illuminant in the experimental verification environment, we constructed a spectrally tunable light source by combining some LEDs. Commercially available high-brightness LEDs, TO-66 (USHIO Inc.), were selected for the device. Table 2.1 shows the peak wavelength and FWHM of the LEDs. The spectral distributions were measured by using a spectral radiance meter (SR-LEDW, Topcon Co.). Figure 2.1 shows the spectral distributions of the LEDs. Since the intensity of each LED distribution varies with each other, some LEDs (peak wavelength: 565 nm and 590 nm) were located twice as much as the other LEDs. Furthermore, each LED intensity was controlled for desired simulated spectra after homogenized intensities by using a controlling unit.

Table 2.1: LED Peak Wavelength and Full-With Half-Maximum

Peak wavelength [nm]	420	430	450	470	505	525	565	590
FWHM [nm]	16	16	30	20	30	30	15	13

Peak wavelength [nm]	620	630	645	660	680	700	720
FWHM [nm]	20	15	20	16	20	30	30

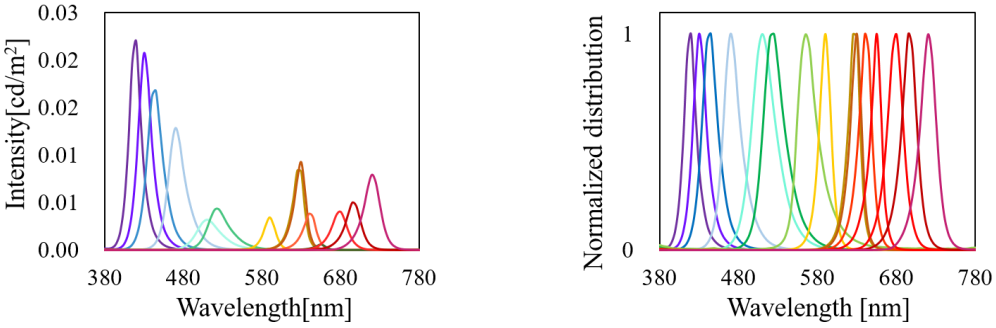

(a) (b)

Figure 2.1: LED distributions: (a) Measured spectral distributions of LEDs, and (b) Normalized spectral distributions of LEDs.

2.2 Controlling unit

For the required specification of the spectrally tunable light source, intensity of each LED wavelength had to be controlled independently. We have two ways to control LED intensities: to change the input current and to control pulse width modulation (PWM). However, intensity modulation by changing the input current causes spectral distribution changes. Therefore, PWM control was selected for this study. Figure 2.2 shows the overview of PWM control. High-speed switching of the input voltage controlled the output intensity. For the spectrally tunable light source, we used Arduino Uno R3 (Arduino Inc.) and a 16-channel 12-bit PWM servo shield (Adafruit Co.).

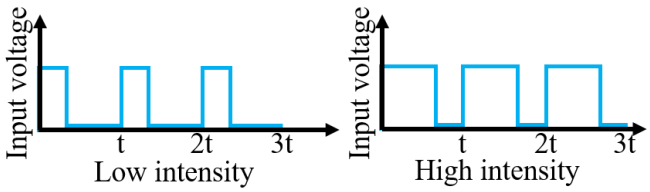

Figure 2.2: Overview of PWM Control

Arduino UNO R3 is a microcontroller board (Figure 2.3 (a)) with an open-source platform that can be operated in a various control environment. This device has an AVR microcontroller and input/output ports, and we can control this device by Arduino IDE (similar to C++). Although Arduino UNO R3 has 6 PWM outputs, the system required 15 kinds of PWM signal outputs. Therefore, a 16-channel 12-bit PWM servo shield (Figure 2.3 (b)) was used for the system. The regulator IC was additionally processed to change the output signal voltage to use the servo shield. Figure 2.4 shows processed part for the servo shield.

PWM outputs input the constant current high power LED driver module for rectification to stabilize the irradiation of LEDs. Figure 2.5 shows the constant current high power LED driver module and additional processing to enable PWM signal input from the ADJ terminals in the constant-current high power LED driver module.

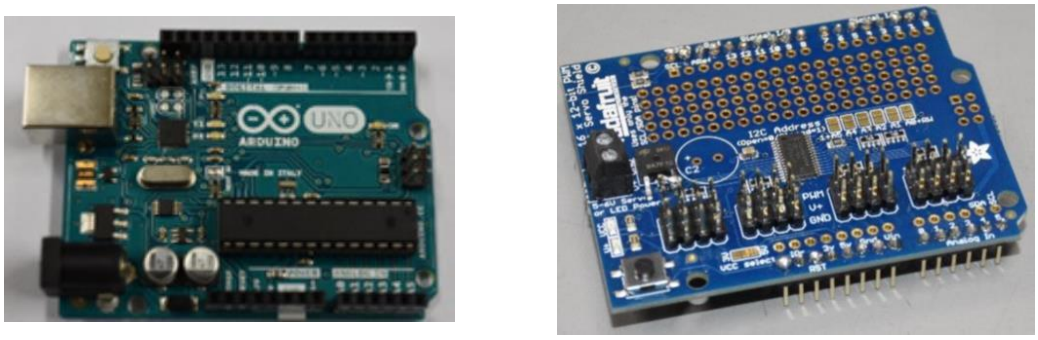

(a) (b)

Figure 2.3: Controlling units: (a) Arduino UNO R3, and (b)PWM servo shield.

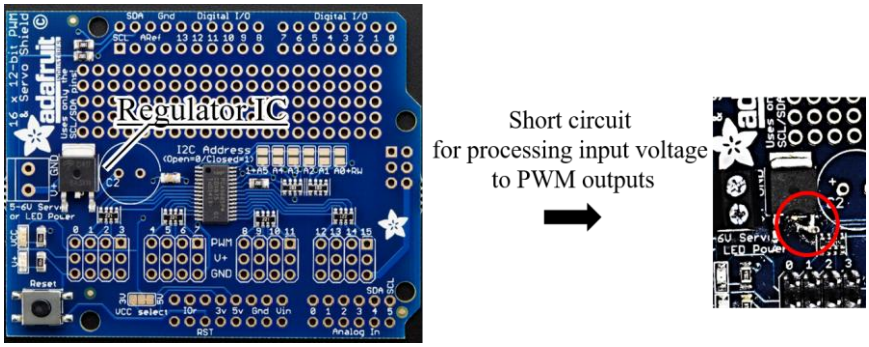

Figure 2.4: Servo-shield additional processing for controlling output regulator IC.

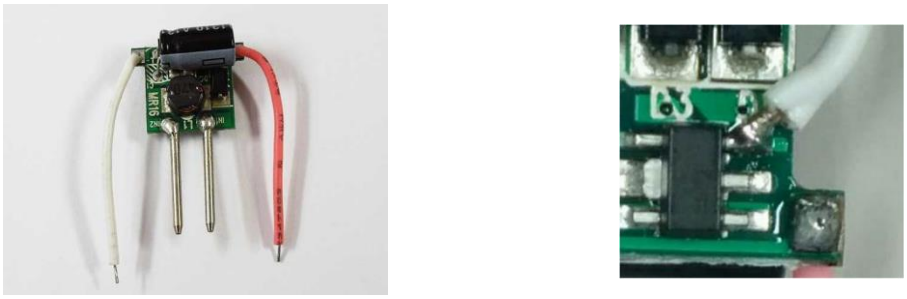

(a) (b)

Figure 2.5: Constant current high power LED driver: (a) overview of the driver, and (b) additional processing for the driver.

2.3 Construction of the spectrally tunable light source: first generation

The spectrally tunable light source is broadly classified into two parts: an illuminant part, mainly LEDs, and a control unit. Figure 2.6 (a) shows the configuration of the LED lighting part, and Figure 2.6 (b) shows the controlling unit. In the lighting section, 12-heat sinks (YH-3020, Ainex Co.,) and four cooling fans (DC fan 24V, MELCO TECHNOREX Co., Ltd.) were set to dissipate heat from LED devices toward outside. To fix the positions of heatsinks, a fixing frame was created using thermoplastic resin. We confirmed that the device satisfied the requirement for the reproduction of desired spectral distributions.

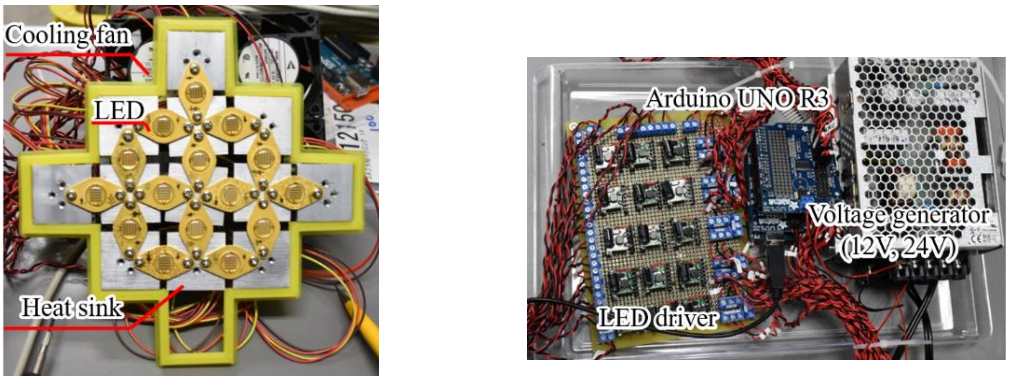

(a) (b)

Figure 2.6: The spectrally tunable light source: (a) LED unit, and (b) controlling unit.

Spectral distributions irradiated by the spectrally tunable light source should be approximately uniformed in experimental fields. Therefore, we evaluated the uniformity of the distributions of lighting, which depended on the LED position. Intensity distribution images of illumination were generated based on the distribution of illumination images. The distribution images were captured when the target region was illuminated from 30 cm above from the LEDs, which implemented in the spectrally tunable light source. Figure 2.7 (a) shows the experimental environment to evaluate of the uniformity of the spectrally tunable light source. Figure 2.7 (b) shows the LED arrangement diagram. The numbers show the order of the LEDs from short-wavelength to long-wavelength. We assumed that the LED is a point light source, and the illumination intensity is linearly attenuated with the angle between the illumination part and the target region. The attenuation was defined based on the LED data sheet, and the half-value angle was assumed 60 degrees. Based on the factors above, the attenuation degree is defined with the distance value *Dis* [cm] from the LED position by the following equation (2-1) .

$$pixelValue = 1 - 5/6 \tan^{-1}(Dis/30) \qquad (2\text{-}1)$$

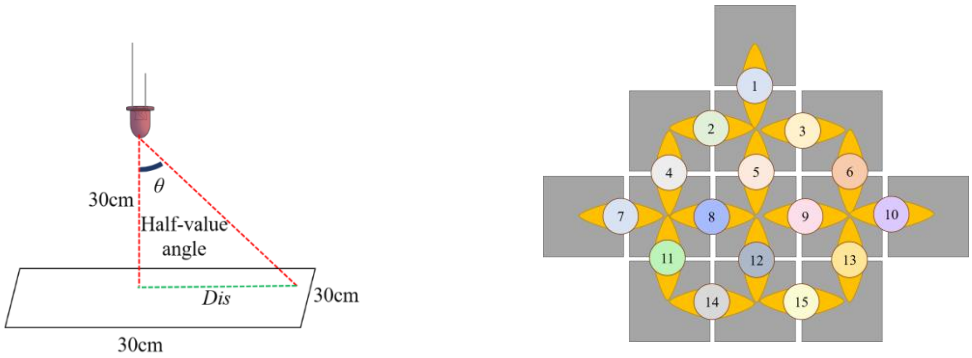

(a) (b)

Figure 2.7: Evaluation environment: (a) Experimental settings for the uniformity of the system, and (b) LED arrangement diagram for the spectrally tunable light source: first generation.

Figure 2.8 shows the intensity distribution images of illumination, which were generated based on the distribution of the illumination images. A monochromatic camera (VC-23 M, Baumer Co., Ltd.) captured these images. The standard deviation images for each pixel position within the target region were obtained by the captured images. Figure 2.9 shows the standard deviation map (highest standard deviation:

0.045). Based on the factors above, the lighting intensity attenuation due to the position of LEDs was almost uniformed. We confirmed the device met the requirement of the specifications for evaluation experiments.

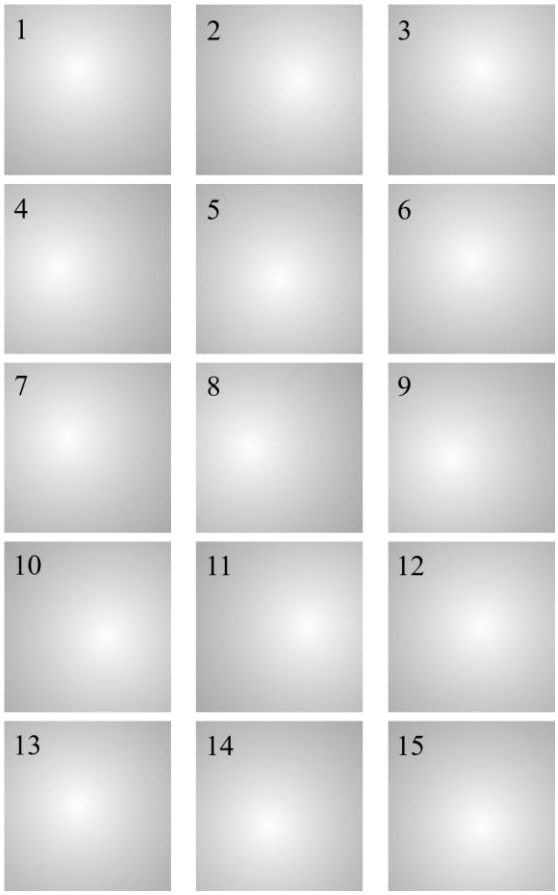

Figure 2.8: Intensity distribution image. The numbers show the LED positions of the spectrally tunable light source.

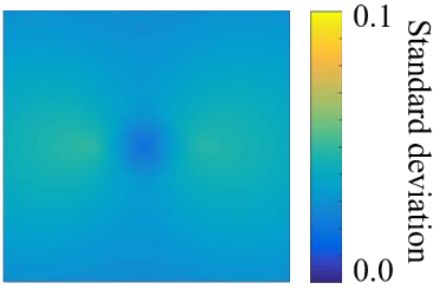

Figure 2.9: Standard deviation image for the evaluation of the uniformity of the spectrally tunable light source: first generation.

2.4 Construction of the spectrally tunable light source: second generation

The spectrally tunable light source described in Section 2.3 was designed to realize a variable-spectral-distribution light source. However, the illumination intensity was insufficient for subjective evaluation experiments because of the intensity variability at the LED wavelength. Therefore, we have developed a device so that the number of LEDs with weak intensity increases by placing more LEDs to mitigate each wavelength's variation and to enhance the intensities. Figure 2.10 shows the LED position and fixing frame design for the illuminant device. These numbers show the LED orders from short-to-long-wavelength. For the second generation device, we used 14 kinds of LEDs, which were the same as the first-generation device except for peak wavelength: 620 nm due to the peak wavelength proximity. In this device, LEDs were set as round shapes to insert the camera to its center position. LED positions were arranged to ensure that the lighting uniformity illumination. Figure 2.11 shows an overview of the device.

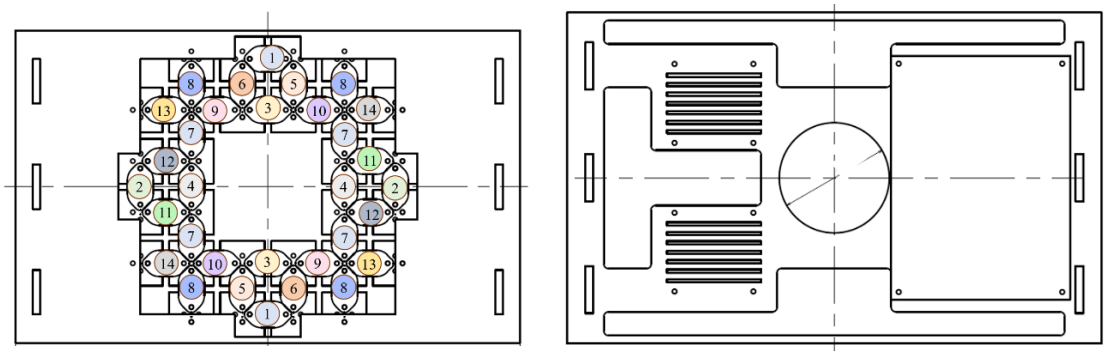

(a) (b)

Figure 2.10: Fixing frame and LED position for the spectrally tunable light source: second generation: (a) LED Position and frame and (b) heat sink frame.

$$F(x,y)=\sqrt{\frac{\sum_{l=1}^{l=14}\left(I_l(x,y)-I(x,y)\right)^2}{14}} \qquad (2\text{-}2).$$

We captured intensity images for each LED, which were implemented in the device for uniformity evaluation. Figure 2.12 shows intensity images for each LED. The device

illuminated a piece of white paper and the images were captured by a monochromatic camera (VC-23M, Baumer Co., Ltd.). The target region was 20 cm square centered directly under the device. Using these images, we calculated standard deviations by calculating $F(x,y)$ for each pixel. The equation (2-2) was used in this experiment.

Figure 2.13 shows the standard deviation image and we confirmed the uniformity of the second generation device.

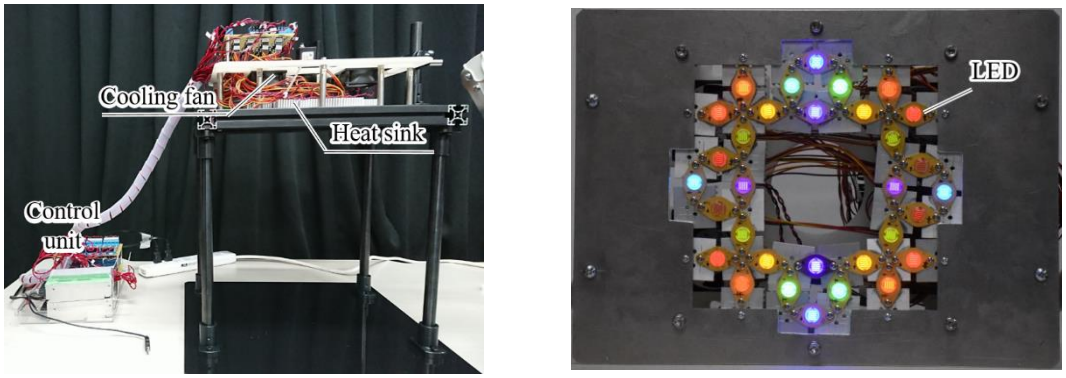

(a) (b)

Figure 2.11: The overview of spectrally tunable light source: second generation. (a) LED irradiation part, and (b) overview of illuminant device.

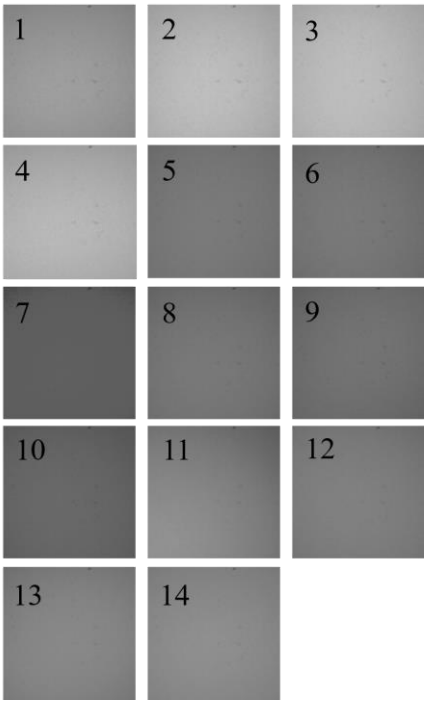

Figure 2.12: Captured image for each LED. The numbers show the LED orders of the spectrally tunable light source: second generation.

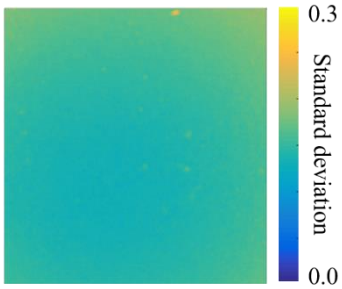

Figure 2.13: Standard deviation for whole LEDs of the uniformity of the spectrally tunable light source: second generation.

2.5 Basic concept of optimization of illuminants

The optimal illuminant design assumes the use of LEDs, which has narrow-bandwidth characteristics. LED is a lighting device that has been widely used in various fields in recent years due to its low cost and long life. By combining multiple LEDs whose peak wavelength is located in visible ranges and controlling each intensity, we can establish various kinds of spectral patterns of illuminant distribution. Figure 2.14 shows a conceptual diagram for controlled LED intensities and various kinds of spectral distributions [29].

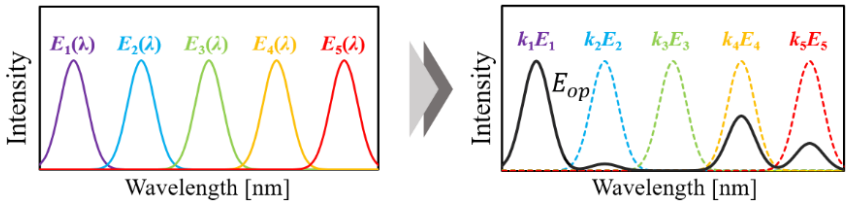

Figure 2.14: Conceptual diagram of LED weighting control.

The distributions of optimal illuminants are expressed by the following equation (2-3) by using known LED distributions ($E_n(\lambda)$, n =1…N) and emission intensities of each LED (k_n , n=1…N).

$$E_{op}(\lambda) = \sum_{n=1}^{N} k_n E_n(\lambda) \qquad (2\text{-}3)$$

The spectral distributions of the optimal illuminants can be obtained by optimally designed emission intensity k_n of each LED. Figure 2.15 shows the calculation flow for the illuminant optimization. In this study, normalized LED distributions implemented in the spectrally tunable light source were used for the optimization.

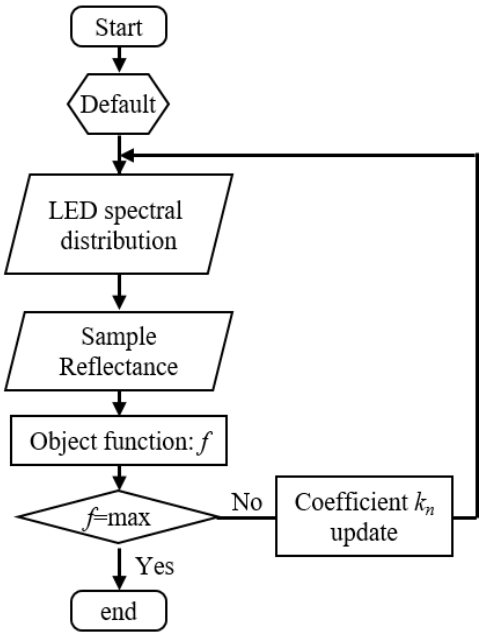

Figure 2.15: Optimization flow for simulation of the optimal illuminant.

XYZ stimulus values, which simulated human visual stimuli, were calculated using the following equation (2-4) for the evaluation of the optimal illuminant:

$$\begin{aligned} X &= k\int \overline{x(\lambda)} E_{op}(\lambda) R(\lambda) d\lambda \\ Y &= k\int \overline{y(\lambda)} E_{op}(\lambda) R(\lambda) d\lambda \\ Z &= k\int \overline{z(\lambda)} E_{op}(\lambda) R(\lambda) d\lambda \\ k &= \frac{100}{\int \overline{y(\lambda)} E_{op}(\lambda) R(\lambda) d\lambda} \end{aligned} \qquad (2\text{-}4)$$

Here $\overline{x(\lambda)}, \overline{y(\lambda)}, \overline{z(\lambda)}$ are the isochromatic functions defined by CIE, and $R(\lambda)$ is the spectral reflectance of the target region. Figure 2.16 shows XYZ isochromatic functions. The evaluation index was calculated by transforming XYZ stimulus values into a

suitable color space for the assumed environment.

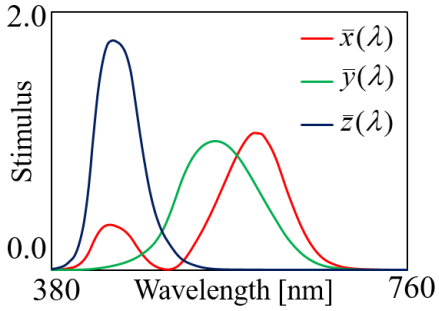

Figure 2.16: XYZ isochromatic functions.

For a camera-illuminant combined system, we calculated RGB signals for the evaluation index. Equation (2-5) shows RGB signal functions. $r(\lambda)$, $g(\lambda)$, $b(\lambda)$ are sensor sensitivities of RGB camera and $R(\lambda)$ is the spectral reflectance of target region.

$$\begin{aligned} R &= \int E_{op}(\lambda) r(\lambda) R(\lambda) d\lambda \\ G &= \int E_{op}(\lambda) g(\lambda) R(\lambda) d\lambda \\ B &= \int E_{op}(\lambda) b(\lambda) R(\lambda) d\lambda \end{aligned} \qquad (2\text{-}5)$$

Using these values, we calculate the optimal illuminant for our system. We used particle swarm optimization [30] as an optimization method to design intensity of each LED.

Chapter 3 Material preparation for illuminant design and evaluation

For the optimization and the evaluation of illuminant distributions, several kinds of rat models were prepared. First, we focused on organ blood circulation by blocking the blood flow shown in Section 3.1. For detailed information from organs, the blood vessel structures are essential factors for surgeons. For example, narrow-band imaging is widely used for digestive system cancer [30, 31]. Therefore, we used the blood vessel structures for supporting surgeons to find distinct regions in also Section 3.1. As a detailed evaluation, we used cattle blood samples whose oxygen saturation was measured before the evaluation in Section 3.2. Finally, in Section 3.3, we set the target as a skin flap model for developing verification.

3.1 Rat cecum with blocked blood flow

A rat (SLC: Wistar, 10-14 week, male) was used for this experiment. The cecum was chosen for blocking the blood flow and measuring spectral reflectance with a hyperspectral camera. After the abdomen of the rat under anesthesia was opened, the cecum was pulled out and fixed on the board without blocking the blood flow so as not to be inhibited by body motion. The rat body was placed on an electric carpet (Yukapet EX, Kainuma-Sangyo, temperature: 38 ± 2 ℃) to keep the body temperature stable. We defined the target as blood circulation. We set this state as “Normal” for the evaluation. Forceps inhibited the blood flow in the cecum to mimic the poor circulation state. This status was defined as “Poor”. In “Poor” status, both arterial blood flow and vein blood flow are blocked, and oxygen saturation levels in the cecum worsen. Spectral reflectance of this region was measured after 3 minutes from blocking the blood flow. Figure 3.1 shows the fixed cecum before and after blocking the blood flow, respectively. Target region for sampling normal status and poor status were selected manually.

For evaluation of the effect of vascular structure enhancement, we used “Normal” sample for the evaluation experiment. Blood vessel regions were manually selected after capturing hyperspectral images. Evaluation experiment using this rat model is described in Chapter 4.

(a) (b)

Figure 3.1: Rat cecum model for blocking blood flow: (a) Normal blood circulation status, and (b) poor blood circulation status.

3.2 Validation with oxygen saturation sample

3.2.1 Cattle blood sample

For detailed evaluation such as subjective evaluation, it is effective to use blood samples whose oxygen saturation was already measured by a blood gas analysis apparatus, i-stat (Abbot Laboratories). As the first step of the evaluation experiment, we used a glass cell sample, which contained cattle blood samples, whose liquid thickness was 5 mm. Oxygen saturations were controlled before the experiments. Figure 3.2 shows the glass cell samples we prepared for the experiment.

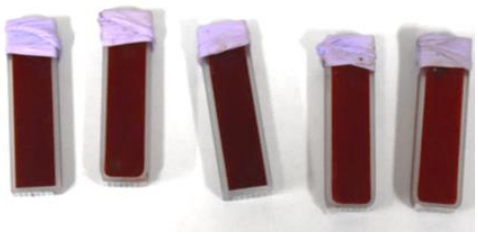

Figure 3.2: Glass cell samples

3.2.2 Cattle blood coveted with vascular endothelial tissue

Since blood flow inside vessel, blood is observed over tissue during surgery. For simulate organs or blood vessels by using oxygen saturation-controlled blood, tissue extracted from animal samples should cover blood samples to mimic the organs or vessels contains blood. Figure 3.3 (a) shows schematic view of model construction. We used vascular endothelial tissue peel off from a main artery of cattle. Figure 3.3 (b) shows vascular endothelial tissue extract from a cattle. The blood sample was injected

under the endothelial tissue by using an injector. Figure 3.3 (c) shows constructed model for the experiment. The blood sample was measured before the experiment, the same as Section 3.2.1.

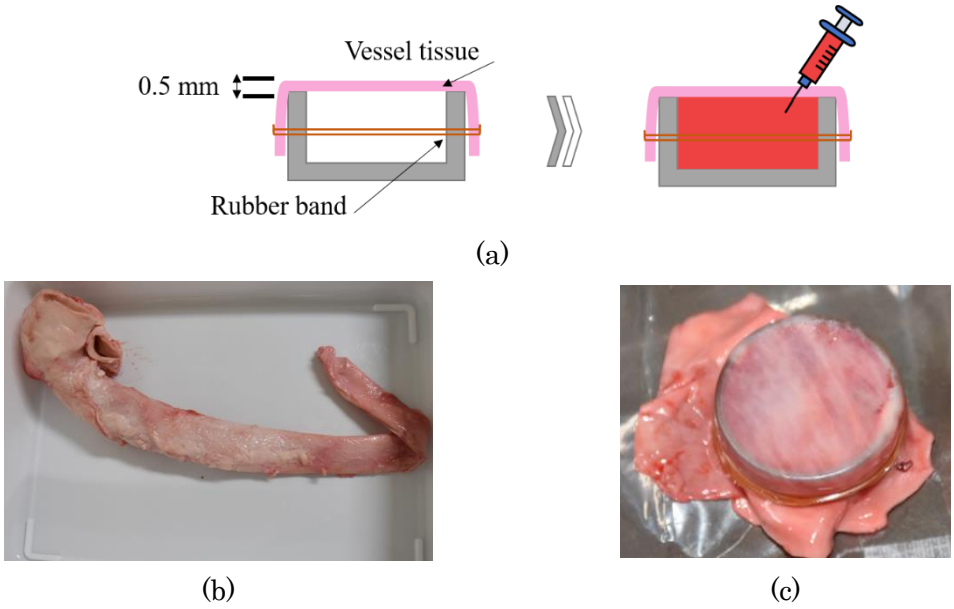

Figure 3.3: Tissue covered sample: (a) Schematic image of created sample, (b) the cattle main artery used in the experiment, and (c) the sample image created for the experiment.

3.3 Skin flap model

3.3.1 Based method

We constructed a model of skin flap necrosis for early diagnosis of skin flap necrosis. In the previous method, a skin flap model was produced by elevating a skin flap to the rat's dorsal side with necrosis proceedings from the opposite side of the blood flow maintained area [32]. However, this method has limitations in their usefulness because of the difficulty of controlling arterial or venous insufficiency. Our evaluation experiments used the new method that elevates skin flaps in the rat's abdomen that underwent reverse U-shaped bipedicled superficial epigastric arteries [33]. Figure 3.4 shows a schematic image of a skin flap model. The left superficial epigastric vessels were maintained.

On the other hand, right superficial epigastric artery or vein was ligated for the ischemia model or the congestion model. An anti-adhesive film was inserted between a skin flap and muscular layer to prevent the blood flow from resumed. Figure 3.5 shows ischemia model and congestion model constructed by the method.

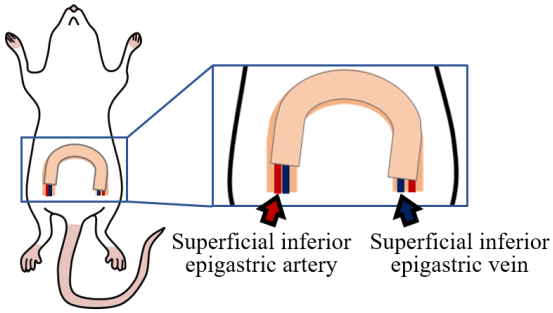

Figure 3.4: Basic skin flap model construction.

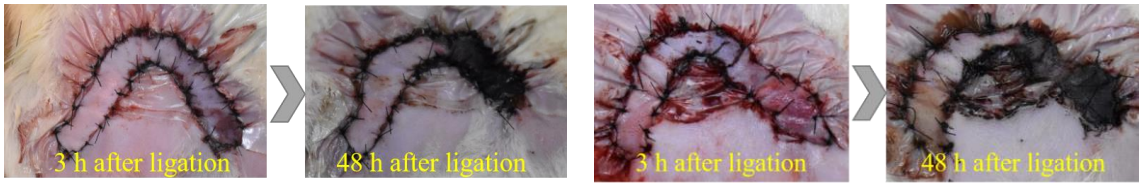

(a) (b)

Figure 3.5: Skin flap model construction based on prior research: (a) Ischemia and (b) congestion model 3 hours and 48 hours after blocking blood flow.

3.3.2 Skin flap chamber

We have to capture spectral reflectance by using a hyperspectral camera for the optimal illuminant design. However, it usually takes a few seconds to capture a full wavelength range. Using a skin flap model refers to Section 3.3.1, it is challenging to capture hyperspectral images due to the body movement caused by breathing. Therefore, we developed a skin chamber for capturing stable hyperspectral images. The U-shaped skin flap, shown in Section 3.3.1, makes it challenging to perform the procedure when the skin flap is fixed to the chamber because of its curved shapes. Therefore, the skin flap's shape was redesigned easy to fit the skin flap chamber [34, 35]. Figure 3.6 shows the initial design model. Figure 3.6 (a) shows a chamber model setting for abdominal region of rat. The second layer flame fixes the skin flap region in the middle of the chamber. The first layer of the chamber was embedded to connect the rat body and the second layer of the chamber. Two layers of the chambers were fixed by M3 screw. We designed the chamber by computer-aided application and constructed it by titanium particles (Figure 3.6 (c)). The first layer of the chamber was fixed the skin flap by using 5-0 nylon thread.

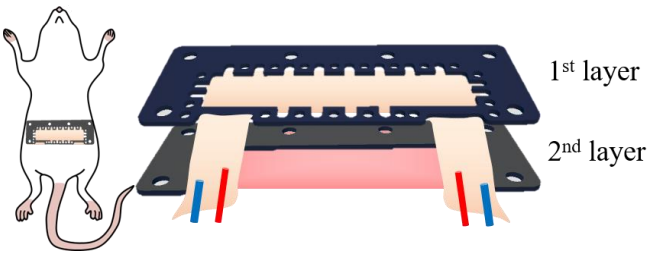

(a)

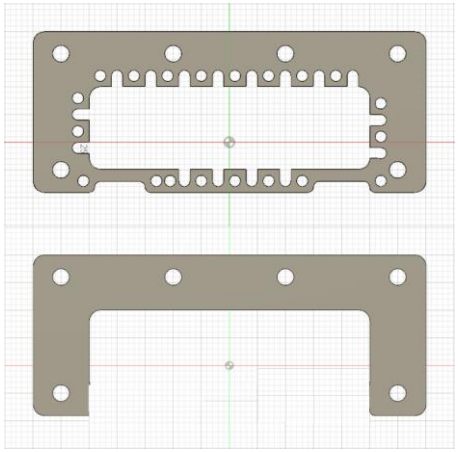

(b)

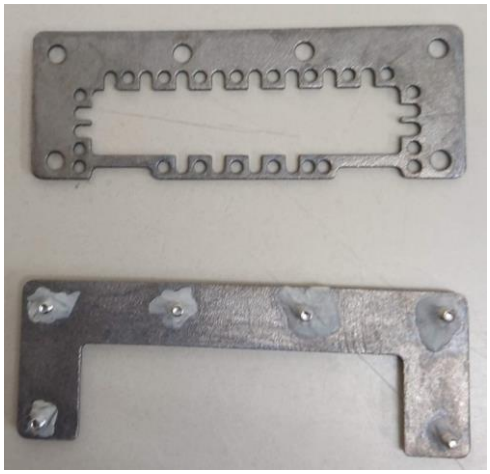

(c)

Figure 3.6: Chamber design: first generation. (a) 3D-cad model. (b) Constructed by titanium particles.

We hold the chamber region by commercially available clips for the hyperspectral image capturing system. Using this chamber, we can capture both skin flap hyperspectral images and blood vessel structures' images located in the skin flap mucosal layer. Each chamber layer has 1 mm thickness for stable fixation.

For stable measurement, skin flap chamber: the first generation was heavy, and there was a possibility for chamber-induced blood flow inhibition. Therefore, we improved the chamber design to reduce the chamber weight. The thickness of each layer was changed from 1 mm to 0.5 mm to reduce the weight. In addition, the parts that are not related to the measurement were reduced by making them hollow. Because of these updates, the weight of the skin flap, which has two layers, became 3 g in the second generation model which was 16 g in the first-generation model. Figure 3.7 shows the second generation chamber design and it's constructed model.

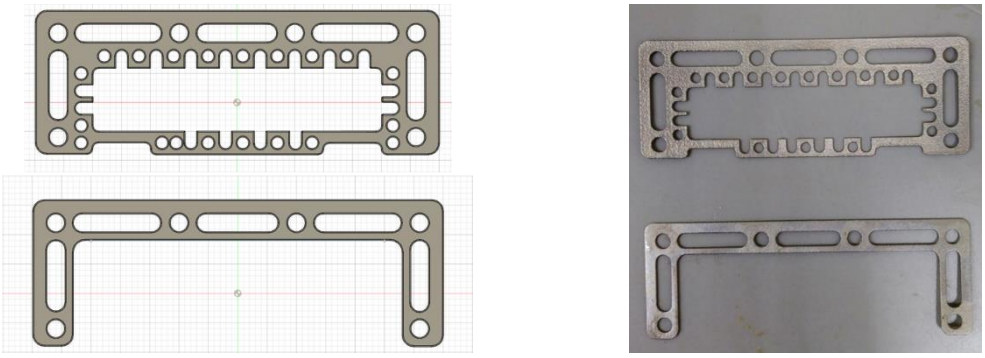

(a) (b)

Figure 3.7: Chamber design: second generation: (a) 3D-cad model and (b) constructed by titanium particles.

3.3.3 Skin flap model construction by using skin flap chamber: first generation

The skin flap model was constructed by using a skin flap chamber: first generation. First, the skin flap region was marked by the following landmarks shown in Figure 3.8 (a). After marking the region (Figure 3.8 (b)), the skin flap was elevated and fixed to the first layer of the chamber (Figure 3.8 (c)). The right side of superficial inferior epigastric artery or vein was ligated after fixing the skin flap to the chamber. In the congestion status, alginate dressing was used to block the blood loss. The skin flap region was fixed to the rat body using the second layer of the chamber shown in Figure 3.8 (d). Before fixing the chamber's first layer to the second layer, an anti-adhesion film was tucked between two chambers not to restart blood flow. During the monitoring of the skin flap region rats were awakening and free feeding.

We constructed the ischemia and the congestion model with a designed skin flap chamber. The designed skin flap chamber makes it possible to capture two sides of skin flap images, surface side image, and mucous side image, in stable status. Figure 3.9 and 3.10 show the congestion model monitoring results from surface sides and mucous sides. In congestion status, the flap color was changed slightly after half a day, but finally, the ligation side's skin flap color turned to dark violet due to lack of arterial blood. On the mucous side, the color changing occurred sooner than surface sides.

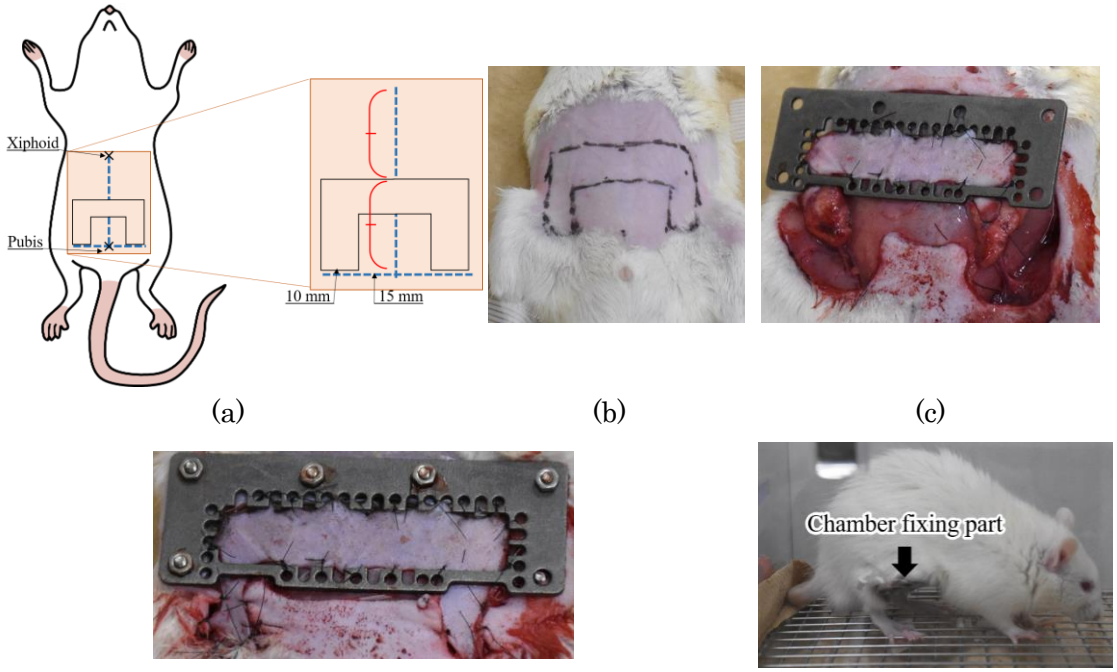

Figure 3.8: Skin flap model construction by using skin flap chamber: first generation: (a) landmarks used when designing the skin flap, (b) guide the skin flap region before fixing the chamber, (c) fixing the skin flap region to the chamber, (d) sutured the chamber and surrounding area and (e) under the awaking status.

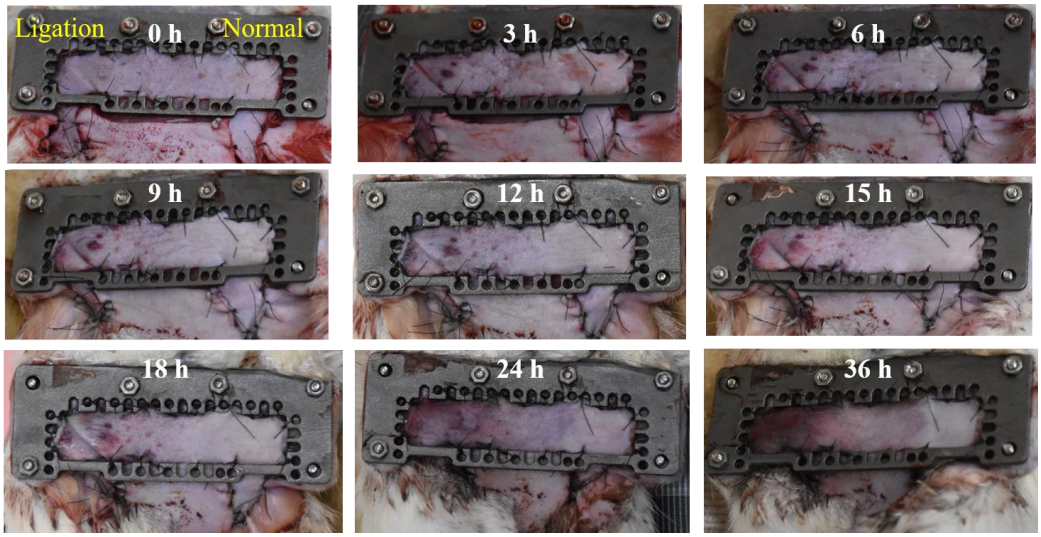

Figure 3.9: Skin flap region / surface side (ishcmeia model) monitored after several time periods.

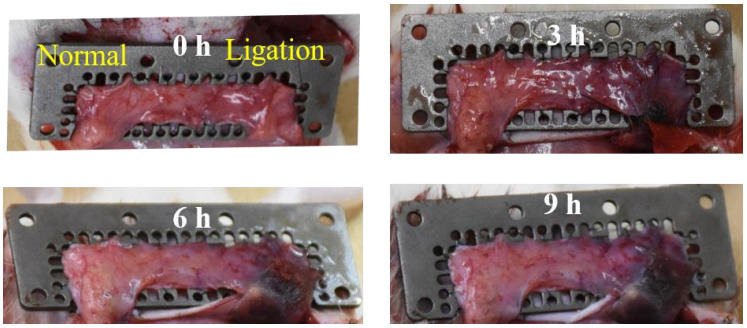

Figure 3.10: Skin flap region / mucous side (ishcmeia model) monitoring with time.

In Figure 3.11 and Figure 3.12, the skin flap congestion model in surface side and mucous side. The flap color was changed sooner than the ischemic model due to a drastic change of blood volume in the region caused by the vein's ligation. In the mucous side, the tissue color turned to dark caused by venous blood. We confirmed the stable monitoring environment using the skin flap chamber: first generation through these model constructions.

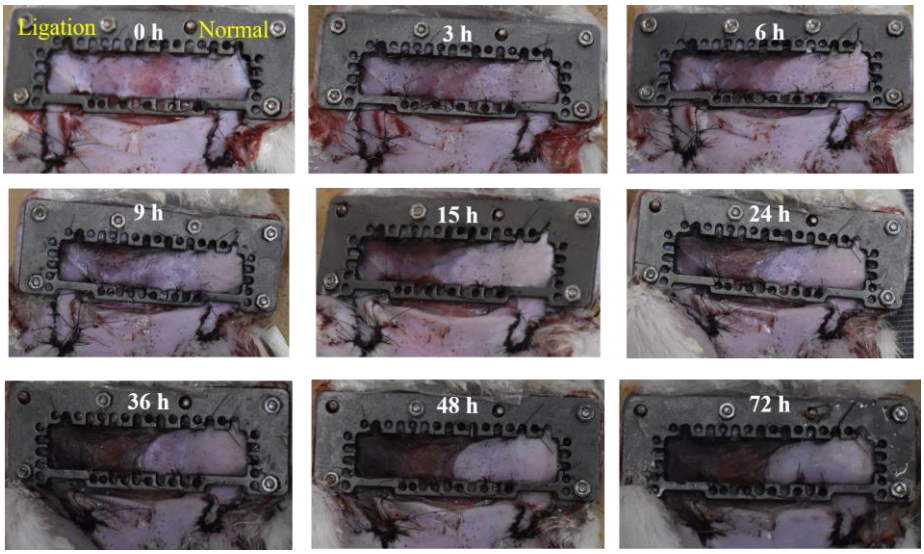

Figure 3.11: Skin flap region / surface side (congestion model) monitored after several time periods.

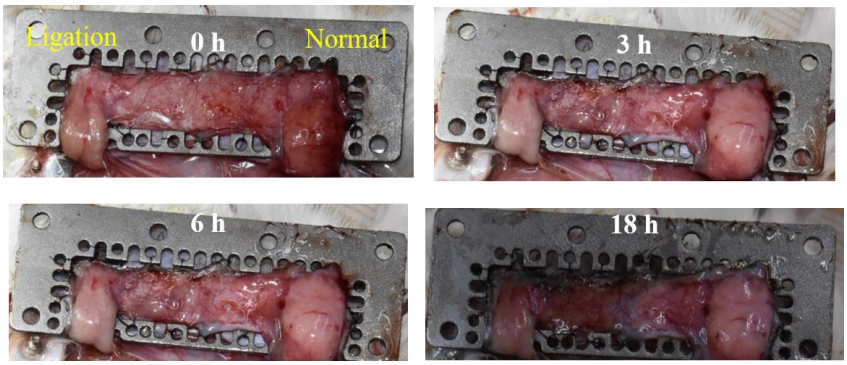

Figure 3.12: Skin flap region / mucous side (congestion model)monitored after several time periods.

3.3.4 Skin flap model construction by using skin flap chamber: second generation

We used the skin flap chamber: second generation for updating the experiment procedures as a second step for the model construction. The experimental procedures were almost as same as the skin flap chamber: first generation. Figure 3.13 and Figure 3.14 shows the ischemia model and Figure 3.15 and Figure 3.16 shows the congestion model. Both models show a similar tendency to the skin flap chamber: first generation. We confirmed the stability for the model construction process by thickness and lightness of the chamber: second generation. We used the skin flap chamber: second generation in a subsequent experiment. To investigate the negative effect of the skin flap chamber, we also constructed normal status without blocking vein or arterial blood flow. Since there was no necrosis region occurred in the observed area, we confirmed no inhibition of blood flow by the designed chamber: second generation. Figure 3.17 shows normal status model.

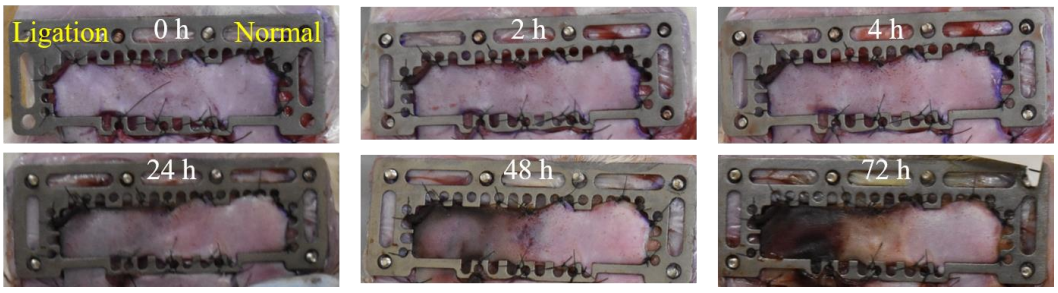

Figure 3.13: Skin flap region / surface side (ishcmeic model) monitoring with time, skin flap region: second generation.

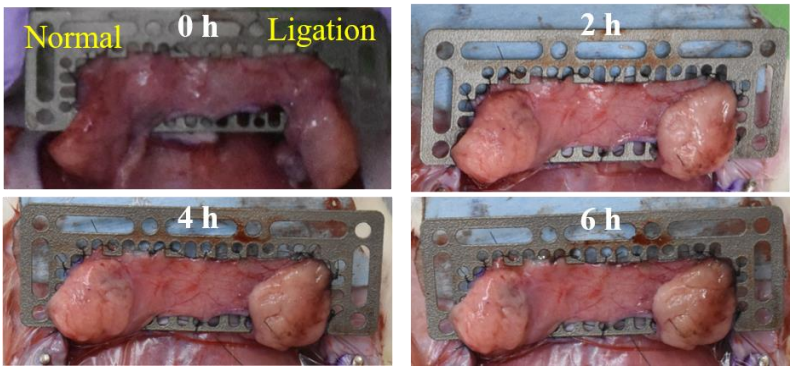

Figure 3.14: Skin flap region / mucous side (ishcmeia model) monitoring with time, skin flap chamber: second generation.

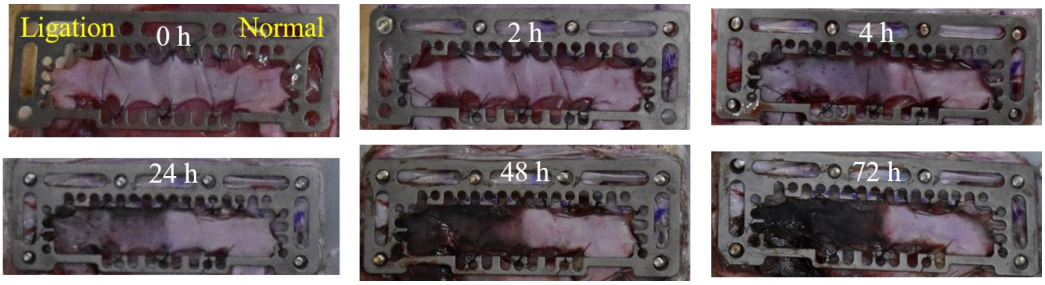

Figure 3.15: Skin flap region / surface side (congestion model) monitoring with time, skin flap region: second generation.

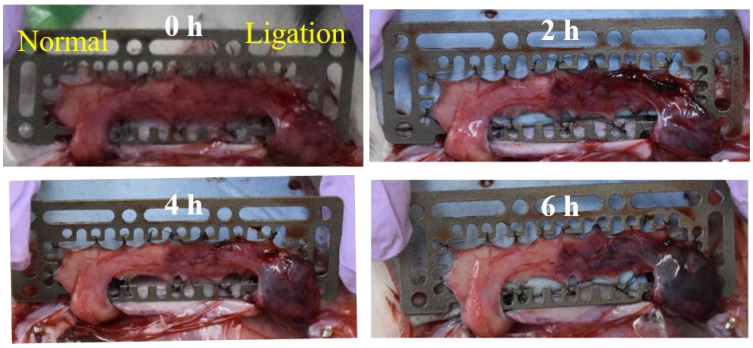

Figure 3.16: Skin flap region / mucous side (congestion model) monitoring with time, skin flap chamber: second generation.

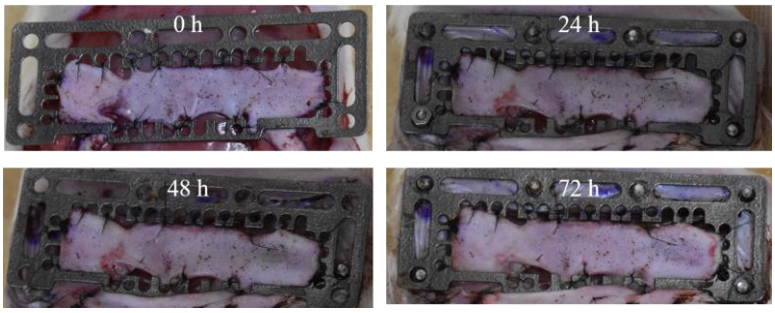

Figure 3.17: Skin flap region / surface side (normal model) monitoring with time, skin flap region: second generation.

3.3.5 Histopathologic analyses for the skin flap model

Histopathologic analysis evaluated the validity of the skin flap model, ischemic model and congestion model with the designed chamber. The histopathologic samples were constructed by using necrosis sides, border between normal and necrosis sides, and normal sides. Necrosis sides were defined as the area that color turned to black. The border sides' sample were extracted from the area that faced to the necrosis sides. The normal sides were extracted from the normal-skin-colored region. Each sample was extracted, stained with hematoxylin and eosin, and observed under magnification 80 × (low-power field) and 400 × (high-power field).

In the ischemic model, intravascular area in the normal regions was filled mildly with red blood cells. In contrast, red blood cells were rarely observed in the intravascular area in the border region. By contrast, in the congestion model, intravascular areas in the border region were fully filled with red blood cells compared to that in the normal region. In necrosis region, hemocytolysis were observed caused by blood circulation inferiority. Since these phenomena were observed in the reference model [33], we confirmed the validity of the skin flap necrosis model with the skin flap chamber. Figure 3.18 shows the skin flap model samples for the histopathologic analysis and Figure 3.19 to Figure 3.21 shows histopathologic images for the ischemia model and the congestion model.

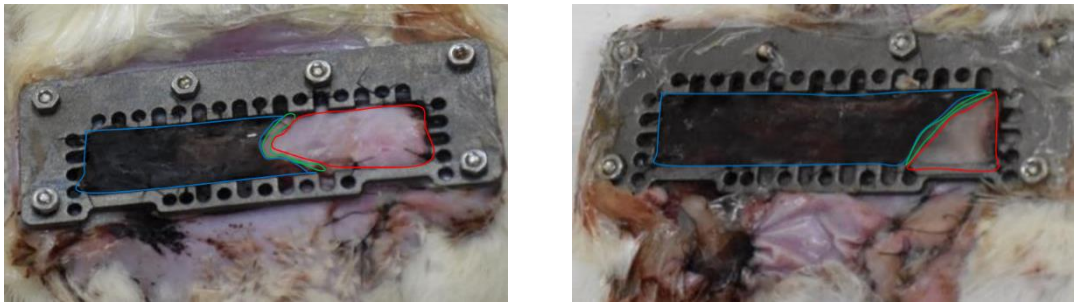

(a) (b)

Figure 3.18: The skin flap model for histopathologic analysis. Necrosis region: Surrounded by blue line. Border region: Surrounded by green line. Normal region: Surrounded by red line: (a) ischemic model, (b) congestion model.

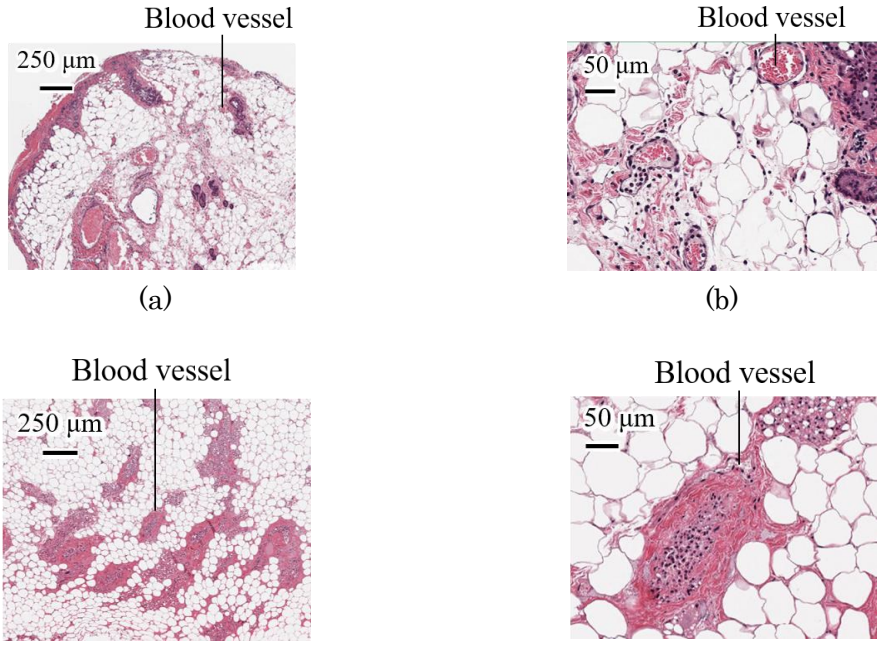

(a) (b)

(c) (d)

Figure 3.19: Histopathologic images for normal region for ischemic model: (a) low-power field (80 ×) and (b) high-power field (400 ×), and border region for ischemic model: (c) low-power field (80 ×) and (b) high-power field (400 ×).

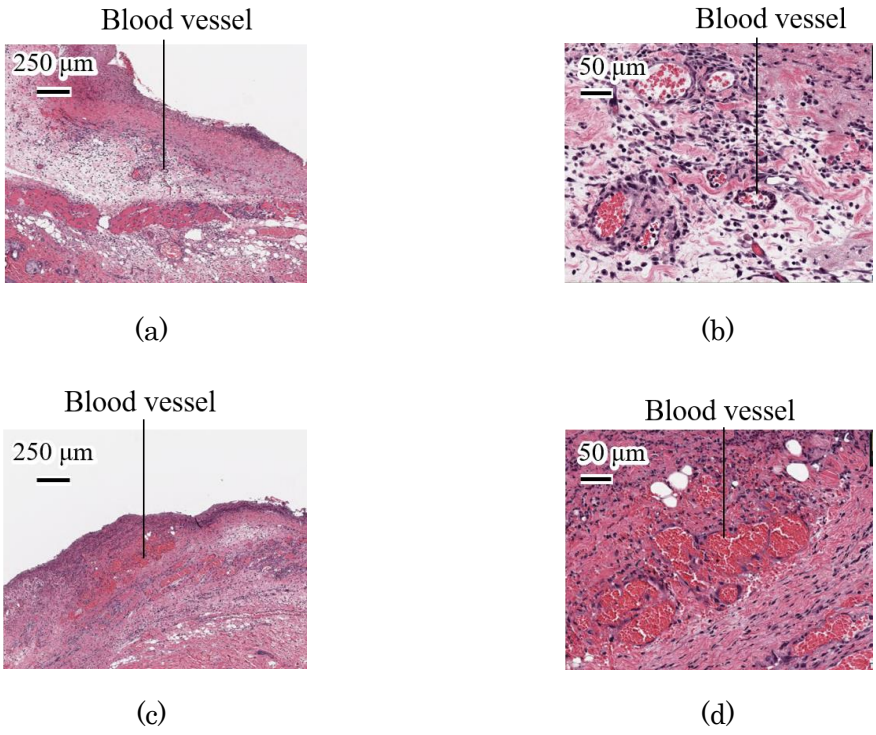

Figure 3.20: Histopathologic images for normal region for congestion model: (a) low-power field (80 ×) and (b) high-power field (400 ×), and border region for ischemic model: (c) low-power field (80 ×) and (b) high-power field (400 ×).

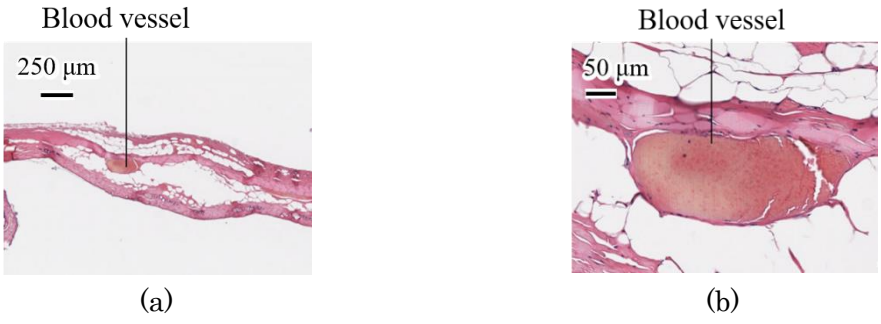

Figure 3.21: Histopathologic images for necrosis region for ischemic model: (a) low-power field (80 ×) and (b) high-power field (400 ×).

3.4 Ethical permission during animal experiments

All animal experiments described in Section 3.1 and Section 3.3 were performed in conformity with the Institutional Animal Care and Use Policy of Chiba University. Authorization numbers for Section 3.1 are 30-161, 1-200, Chiba University. The authorization number for Section 3.3 is 2-46 Chiba University. During these experiments, the heat mat (Yukapet, Kainuma-sangyo, temperature: 38 ± 2 ℃) was used for heat-retention of rats' bodies. The surgical vital signs, i.e., the heart rate and oxygen saturation, were conducted during the experiment.

Chapter 4 Surgical illuminant optimization for organ blood circulation

This chapter details the optimal illuminant for blood oxygen saturation enhancement. The optimization method for blood circulation condition enhancement is shown in Section 4.1. We used color difference based on CIECAM02 to consider illuminant conditions changing. Section 4.1.1 shows the calculation method, and the evaluation index for optimization of the illuminant is given in Section 4.1.2. As an initial consideration, we used a rat cecum for the simulation of the optimal illuminant. The evaluation experiment describes in Section 4.2. In Section 4.3, cattle blood samples with known oxygen saturation are used for the subjective evaluation for the optimal illuminant. Finally, in Section 4.4, we focus on the model of skin flap necrosis for the evaluation as a disease model.

4.1 Optimization method

4.1.1 Color difference: Evaluation index

We used color difference based on CIECAM02 color appearance model [36, 37] recommended by CIE in 2002 for the optimization of the illuminant. This model establishes to quantify the target color, taking the brightness and illuminant color into consideration. Therefore, this model is thought to be a useful method for evaluating colors in different observation environments, such as different displays and printed papers.

The color difference based on CIECAM02 was used to evaluate the enhancement effect by calculating the color difference between normal and poor circulation regions. Illuminant color difference between the conventional illuminant and the calculated illuminant was also calculated by using the color difference to evaluate the illuminant color uniformity.

The three kinds of parameters, c, N_C, F, were calculated by using brightness value

S_R. The brightness value S_R is defined as ratio of L_{SW} to L_{DW}, which represents the luminance of the illuminant and the surroundings, respectively. The S_R value is expressed by the following equation (4-1):

$$S_R = L_{SW} / L_{DW} \qquad (4\text{-}1)$$

When S_R value is greater than 0.2, surrounding environment is named as the average. When S_R is less than 0.2, surrounding environment is named as dim surroundings, and when S_R is equal to 0, it is defined as dark surroundings. Table 4.1 shows the surrounding parameters for CIECAM02.

Table 4.1: Surrounding parameters for CIECAM02

Surroundings	c	N_C	F
average(S_R>0.2)	0.69	1.0	1.0
dim(S_R<0.2)	0.59	0.9	0.9
dark (S_R=0)	0.525	0.8	0.8

The adaptive luminance value L_A is obtained by dividing the illuminance of the target by 5π. The long, medium and short-wavelength cones are the values converted from *XYZ* stimulus values as follows:

RGB signals, which related to long, medium, and short-wavelength range, are calculated by converted XYZ stimuli as follows.

$$\begin{bmatrix} R \\ G \\ B \end{bmatrix} = \mathbf{M}_{CAT02} \begin{bmatrix} X \\ Y \\ Z \end{bmatrix}$$
$$\mathbf{M}_{CAT02} = \begin{bmatrix} 0.7328 & 0.4296 & -0.1624 \\ -0.7036 & 1.6975 & 0.0061 \\ 0.0030 & 0.0136 & 0.9834 \end{bmatrix} \qquad (4\text{-}2)$$

The adaption factor *D,* which shows the adaption degree from equal-energy white to illuminant color is given by the following equation (4-3). If the *D* value equals to 1, which means the full adaptation to the illuminant color and if the *D* value equals to zero, it means no adaptation to the illuminant color. The minimum value for the generous visual environment is 0.6.

$$D = F\left[1 - \frac{1}{3.6}\mathrm{e}^{\left(\frac{-(L_A+42)}{92}\right)}\right] \qquad (4\text{-}3)$$

Using adaptation factor *D*, the cone response given in (4-2) are applied to the color adaptation by equation (4-4):

$$\begin{aligned} R_C &= \left[(Y_W \cdot D / R_W) + (1-D)\right]R \\ G_C &= \left[(Y_W \cdot D / G_W) + (1-D)\right]G \\ B_C &= \left[(Y_W \cdot D / B_W) + (1-D)\right]B \end{aligned} \qquad (4\text{-}4)$$

R, G, and *B* are the cone response values of the object and R_W , G_W , B_W are the cone response values of the illuminant. F_L , n , N_{bb} , N_{cb} are used as coefficients, which depend on the observation condition.

$$k = 1/\left(5L_A + 1\right) \qquad (4\text{-}5)$$

$$F_L = 0.2k^4\left(5L_A\right) + 0.1\left(1-k^4\right)^2\left(5L_A\right)^{1/3} \qquad (4\text{-}6)$$

$$n = Y_b / Y_w \qquad (4\text{-}7)$$

$$N_{bb} = N_{cb} = 0.7125\left(1/n\right)^{0.2} \qquad (4\text{-}8)$$

Y_b is *Y* stimulus value in background, and Y_w is *Y* stimulus value in reference light source. The following equation (4-9) and (4-10) are used to simulate the input-output characteristics of the cone responses:

$$\begin{bmatrix} R' \\ G' \\ B' \end{bmatrix} = \mathbf{M}_{HPE}\mathbf{M}_{CAT02}^{-1}\begin{bmatrix} R_C \\ G_C \\ B_C \end{bmatrix}$$

$$\mathbf{M}_{HPE} = \begin{bmatrix} 0.38971 & 0.68898 & -0.07868 \\ -0.22981 & 1.18340 & 0.04641 \\ 0.00000 & 0.00000 & 0.00000 \end{bmatrix} \quad (4\text{-}9)$$

$$\mathbf{M}_{CAT02}^{-1} = \begin{bmatrix} 1.096124 & -0.278869 & 0.182745 \\ 0.454369 & 0.473533 & 0.072098 \\ -0.009268 & -0.005698 & 1.015326 \end{bmatrix}$$

$$R'_a = \frac{400\left(F_L R'/100\right)^{0.42}}{27.13+\left(F_L R'/100\right)^{0.42}} + 0.1$$

$$G'_a = \frac{400\left(F_L G'/100\right)^{0.42}}{27.13+\left(F_L G'/100\right)^{0.42}} + 0.1 \quad (4\text{-}10)$$

$$B'_a = \frac{400\left(F_L B'/100\right)^{0.42}}{27.13+\left(F_L B'/100\right)^{0.42}} + 0.1$$

The color coordinates *a*, *b* and *h* (frequency) for the eccentricity and perceptual attributes' definition are calculated using the following equation (4-11):

$$\begin{aligned} a &= R_a' - 12G'_a/11 + B'_a/11 \\ b &= (1/9)\left(R_a' + G_a' - 2B_a'\right) \\ h &= \tan^{-1}(b/a) \end{aligned} \quad (4\text{-}11)$$

The eccentricity e_t is obtained by using *h*:

$$e_t = 1/4\cos\left[\left(h\frac{\pi}{180}+2\right)+3.8\right] \quad (4\text{-}12)$$

The achromatic response of the object *A* and illuminant A_W is given by the following equation(4-13):

$$A = \left[2R_a' + G_a' + (1/20)B_a' - 0.305\right]N_{bb} \quad (4\text{-}13)$$

Brightness value J is obtained by using A and A_w :

$$J = 100\left(A / A_W\right)^{c(1.48+\sqrt{n})} \quad (4\text{-}14)$$

Chroma C, colorfulness M are calculated by using t, which is calculated by following (4-15):

$$t = \frac{(50000/13) N_c N_{cb} e_t \left(a^2 + b^2\right)^{1/2}}{R_z^{'} + G_z^{'} + (21/20) B_z^{'}} \quad (4\text{-}15)$$

$$C = t^{0.9} \sqrt{J/100} \left(1.64 - 0.29^n\right)^{0.73} \quad (4\text{-}16)$$

$$M = C F_L^{0.25} . \quad (4\text{-}17)$$

Table 4.2 sets the parameters for the degree of color difference for calculation of color differences. The degree of color difference is defined as Large Color Difference (LCD), Small Color Difference (SCD), and Uniform Color Difference (UCD) to represent color differences.

Table 4.2: Parameters for calculation of color differences

Version	LCD	SCD	UCS
K_L	0.77	1.24	1.00
c_1	0.007	0.007	0.007
c_2	0.0053	0.0363	0.0228

By using (4-18) to (4-22), color difference $\Delta E'$ is calculated as follows:

$$J' = \frac{\left(1 + 100 c_1\right) J}{1 + c_1 J} \quad (4\text{-}18)$$

$$M' = (1/c_2)\ln(1 + c_2 M) \quad (4\text{-}19)$$

$$a_M^{'} = M'\cos(h) \quad (4\text{-}20)$$

$$b_M^{'} = M'\sin(h) \quad (4\text{-}21)$$

$$\Delta E' = \sqrt{(\Delta J' / K_L)^2 + \Delta a_M^{'} + \Delta b_M^{'}}\ . \quad (4\text{-}22)$$

4.1.2 Optimization index

In this research, we designed a surgical illuminant distribution that can emphasize the subtle difference between target and peripheral regions for supporting visual discrimination. Surgeons perform surgery under high-luminance white lights, called a shadow less lamp, which does not cast shadows in the operation field. Therefore, the optimal illuminant condition shall maintain the illuminant color's whiteness, while keeping illuminant color the same as the conventional surgical illuminant. Keeping illuminant color whiteness will allow surgeons to become accustomed to conventional illuminants and make them less likely to feel fatigued. We focused on metamerism characteristics shown in Section 1.2.2. Illuminant metamerism makes it possible to achieve the optimization that can emphasize the target region while maintaining the illuminant color whiteness as same as a conventional surgical illuminant using these characteristics.

In this chapter, we focus on the optimal illuminant that can enhance the blood circulation of organs. We assumed that the surgeons used the optimal illuminant only to determine the blood circulation, even if the illuminant color is the same as the conventional illuminant for considering the possibility for the changing surgical field's color environment. The optimal illuminant overview is shown in Figure 4.1. For illuminant optimization, we assumed to use LEDs implemented in the spectrally tunable light source: first generation shown in Chapter 2.

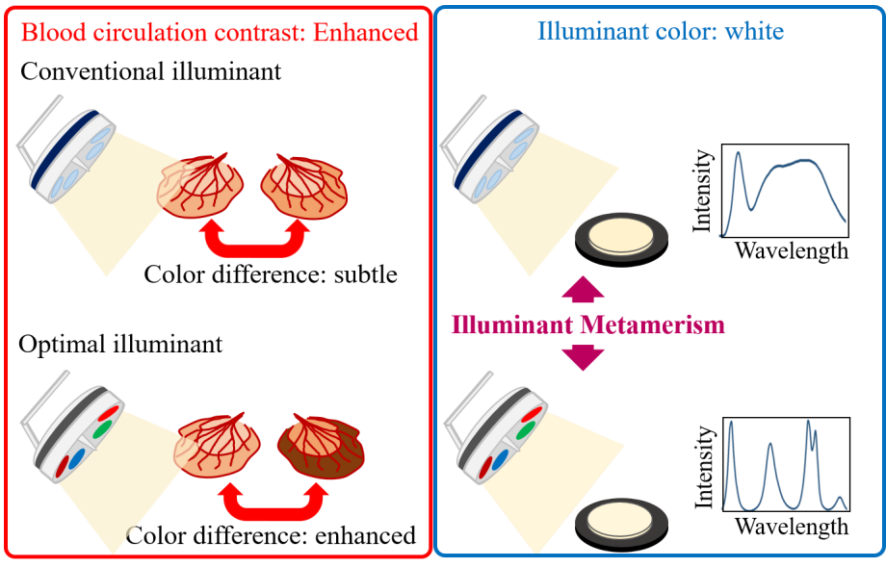

Figure 4.1: Optimization overview of the illuminant.

We used the method shown in the basic concept of optimization of illuminants in Section 2.5 for illuminant optimization. To be compatible with illuminant whiteness and enhancement of organ blood circulation state, we used two indexes for the evaluation: index α, which represents the difference between poor and normal circulation regions under the calculated illuminant, and index β, which represents the whiteness of the illuminant color between the conventional illuminant color and the calculated illuminant color under the conventional illuminant color. For establishing two purposes we mention above, the optimization index is defined as follows by maximizing f value:

$$f\left(E_{\text{opt}}(\lambda)\right)=\alpha\left(E_{\text{opt}}(\lambda)\right)-\gamma\cdot\beta\left(E_{\text{opt}}(\lambda)\right). \tag{4-23}$$

The parameter γ can control the balance between enhancement level α and illuminant whiteness value β. The larger γ value makes the optimal illuminant color more similar to the conventional illuminant color. The smaller γ value establishes to make apparently enhanced the difference between two conditions under the less illuminant color white. Figure 4.2 shows the flow of calculation of evaluation index.

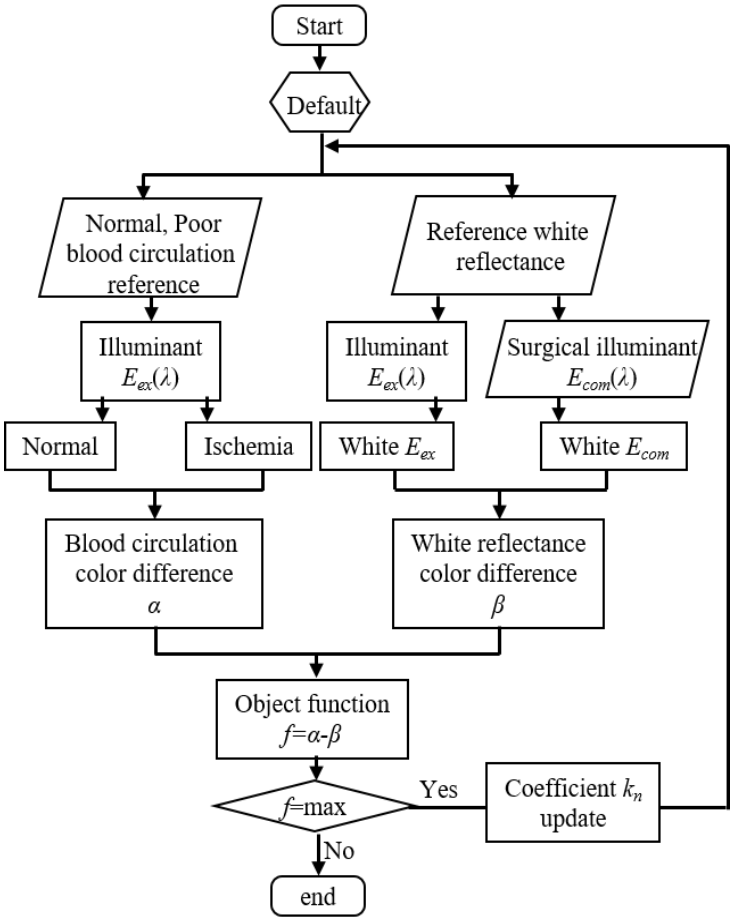

Figure 4.2: Evaluation index for the optimal illuminant: Blood circulation enhancement.

4.2 Quantitative evaluation experiment: Rat organ sample

4.2.1 Data collection

In this experiment, a rat was used to evaluate the effectiveness of the optimal illuminant that enhances the difference between the normal and the poor circulation region. The rat cecum setting was described in Section 3.1. We captured hyperspectral images and calculated spectral reflectance to evaluate the spectral characteristics of blood circulation conditions. The camera we used was NH-8 (EBA JAPAN Co.), with 1200×1024 pixels, 12 bits per pixel, and covers the spectral range from 380 nm to 1000 nm with 5 nm intervals. Xenon light was irradiated directly above the target region, and the images were captured from the 45° direction (based on CIE recommendation,

Figure 1.3 (b)). Figure 4.3 shows the geometry for capturing the hyperspectral images. As a first step, a hyperspectral image was captured before blocking the blood flow. We can get the "Normal" characteristics from this image. Next, "Poor" characteristics were captured by blocking blood flow for 3 minutes using a bulldog cramp. Figure 4.4 shows the rat's cecum image, "Normal" status and "Poor" status, captured by the hyperspectral camera. The conventional surgical light source (Skylux Crystal, Yamada Shadowless Lamp Co. Ltd.) was used for simulating the RGB images. To evaluate spectral characteristics, the region of interest (ROI) was set in the middle of the target region. Figure 4.5 shows the spectral reflectance of "Normal" and "Poor" and the absorption coefficient of Hb and HbO_2. Two spectral references are remarkably different between 600-720 nm, while 550-600 nm were similar trends.

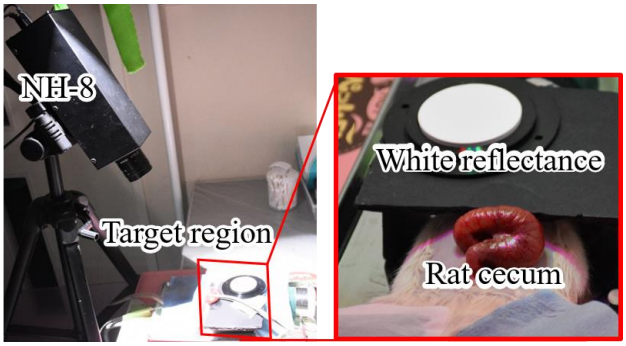

Figure 4.3: Image capturing geometry.

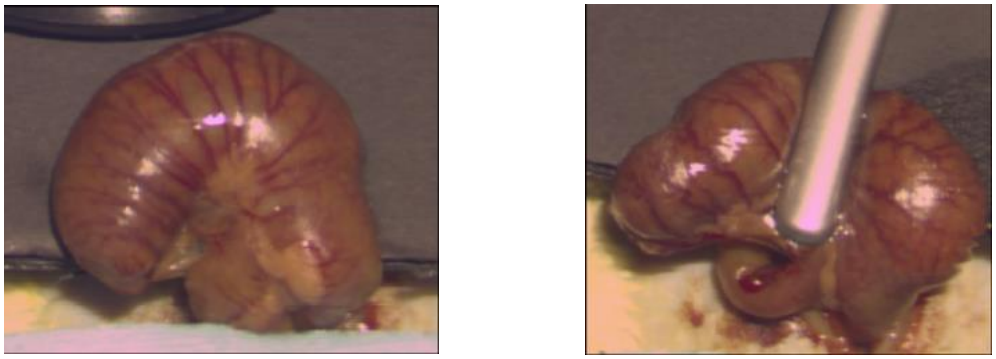

(a) (b)

Figure 4.4: Captured target images: (a) Before blocking the blood flow and (b) after blocking the blood flow (3 min) .

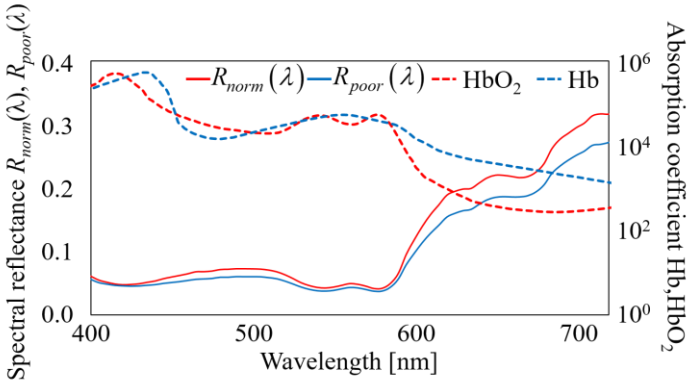

Figure 4.5: Spectral reflectance of blood circulation (solid line) and spectral absorption of Hb and HbO_2 (dashed line).

4.2.2 Simulation of the optimal illuminant

For the illuminant design, we used spectral reflectance shown in Figure 4.5 and LED distributions shown in Figure 2.1. As a conventional illuminant spectrum, we used LED surgical illuminant, Skylux Crystal (Yamada Shadowless Lamp Co. Ltd.), as a reference illuminant spectrum. Figure 4.6 shows the illuminant distribution of Skylux Crystal and reproduced the illuminant spectrum by using the spectrally tunable light source: first generation. The reproduced spectrum of the conventional illuminant was set by the least squared method. We calculated three types of the optimal illuminants to enhance the blood circulation condition using the evaluation index (4-23). The illuminant whiteness controlling index γ were set as $\gamma = 0.5, 1, 1.5$. Figure 4.7 shows the designed illuminant spectra.

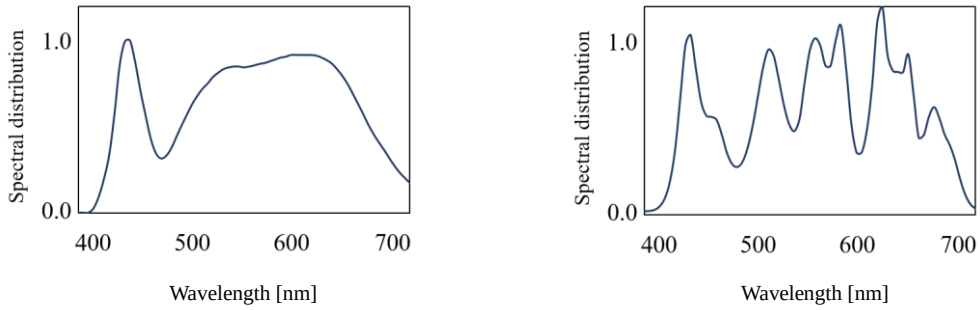

Figure 4.6: Conventional illuminant spectrum: (a) Skylux Crystal and (b) reproduced illuminant spectrum combined with LED distributions implemented in the spectrally tunable light source: first generation.

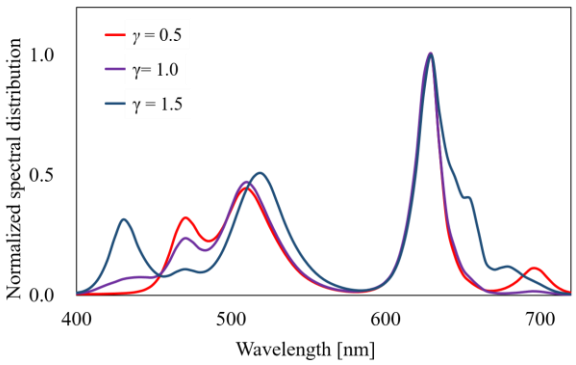

Figure 4.7: Simulated illuminant spectra for enhance blood circulation condition.

The largest spectrum peak was around 600-650 nm and the second largest peak was around 450-550 nm. These two peaks were located on the remarkable differences between normal and ischemic status regions. The illuminant spectrum $\gamma = 0.5$ was almost similar to that $\gamma = 1.0$ except a small peak located on 700 nm. This tendency may be caused by enhancing long-wavelength differences at the expense of illuminant whiteness. Comparing two illuminant spectrum $\gamma = 0.5$ and $\gamma = 1.0$, the illuminant spectrum $\gamma = 1.5$ has broaden distribution. Since γ value related to the illuminant color whiteness, it is assumed that the whiteness of the illuminant is related to the broadness of the illumined distribution.

Table 4.3 shows the color difference between normal and poor status and the illuminant color difference between simulated illuminant and the conventional illuminant. The color difference between normal and ischemic status in smaller γ value were acquired. The larger γ values related to smaller color difference between the designed illuminant spectra and the conventional illuminant.

Table 4.3: Evaluation index ΔE' for under the conventional illuminant and optimal illuminant for the illuminant optimization. Target color difference: between normal and ischemia status. Illuminant color difference: between the simulated illuminants and the conventional illuminant.

	Conventional illuminant (Skylux Crystal)	Optimal illuminant		
		$\gamma = 0.5$	$\gamma = 1.0$	$\gamma = 1.5$
Color difference ΔE' (Normal-Ischemia)	1.54	2.84	2.76	2.24
Color difference ΔE' (Whiteness)	0.00	0.70	0.45	0.21

4.2.3 Evaluation experiment

We evaluated the simulated illuminant effect by using rat ceca (the number of samples: 3) for the illuminant spectrum for $\gamma = 1.0$. The conventional illuminant spectrum, Skylux Cristal (Yamada Shadowless lamp Co. Ltd) was reproduced by using the spectrally tunable light source: first generation that is shown in Figure 4.6 for comparison. The rat ceca were set as same as the data collection part shown in Section 3.1. Reflected light from the target region were measured by spectral radiance meter, SR-LEDW (Topcon Co.). Figure 4.8 shows the experimental setup for the evaluation experiment.

Figure 4.8: Experimental setup for the evaluation experiment.

For evaluation of effect of the optimal illuminant, color differences between before-block-blood-flow and after-block-blood-flow under two illuminant condition, the conventional and the optimal illuminant were calculated by using spectral distributions of the samples.

Furthermore, color samples for each sample under two kinds of illuminants were reproduced by using captured spectral distributions. Figure 4.9 shows color differences and color samples under two illuminant conditions. The color differences under the optimal illuminant were larger than those under the conventional illuminant in all cases. These results confirmed that the blood circulation state could be enhanced by optimizing the illuminant spectrum. We also confirmed that under the optimal illuminant, the change in color tone was more extensive than under the conventional illuminant due to the change in blood circulation.

		Elapsed time[min]				
Sample 1	**Conventional illuminant**	2	4	6	8	10
		$\Delta E'$=3.72	$\Delta E'$=3.93	$\Delta E'$=4.01	$\Delta E'$=4.00	$\Delta E'$=4.09
		12	14	16	18	20
		$\Delta E'$=3.88	$\Delta E'$=5.14	$\Delta E'$=4.06	$\Delta E'$=3.69	$\Delta E'$=3.42
	Optimal illuminant	2	4	6	8	10
		$\Delta E'$=4.44	$\Delta E'$=4.44	$\Delta E'$=4.50	$\Delta E'$=4.12	$\Delta E'$=3.75
		12	14	16	18	20
		$\Delta E'$=3.95	$\Delta E'$=5.36	$\Delta E'$=4.75	$\Delta E'$=4.38	$\Delta E'$=3.87
Sample 2	**Conventional illuminant**	2	4	6	8	10
		$\Delta E'$=3.45	$\Delta E'$=3.73	$\Delta E'$=3.91	$\Delta E'$=4.07	$\Delta E'$=4.18
		12	14	16	18	20
		$\Delta E'$=4.43	$\Delta E'$=4.67	$\Delta E'$=4.67	$\Delta E'$=4.41	$\Delta E'$=4.32
	Optimal illuminant	2	4	6	8	10
		$\Delta E'$=6.82	$\Delta E'$=6.15	$\Delta E'$=6.02	$\Delta E'$=6.16	$\Delta E'$=5.95
		12	14	16	18	20
		$\Delta E'$=5.96	$\Delta E'$=5.94	$\Delta E'$=7.15	$\Delta E'$=9.30	$\Delta E'$=8.88
Sample 3	**Conventional illuminant**	2	4	6	8	10
		$\Delta E'$=7.51	$\Delta E'$=8.67	$\Delta E'$=9.15	$\Delta E'$=8.29	$\Delta E'$=8.29
		12	14	16	18	20
		$\Delta E'$=8.90	$\Delta E'$=8.78	$\Delta E'$=8.71	$\Delta E'$=10.02	$\Delta E'$=10.28
	Optimal illuminant	2	4	6	8	10
		$\Delta E'$=9.61	$\Delta E'$=10.20	$\Delta E'$=9.38	$\Delta E'$=9.62	$\Delta E'$=10.08
		12	14	16	18	20
		$\Delta E'$=11.28	$\Delta E'$=9.42	$\Delta E'$=9.63	$\Delta E'$=10.47	$\Delta E'$=10.26

Figure 4.9: Color samples and color difference under the conventional illuminant and the optimal illuminant.

4.3 Subjective evaluation experiment: Cattle blood sample

4.3.1 Data collection

In Section 4.2, we evaluated the effect of the optimal illuminant by measuring color differences. We focused on subjective evaluation as a next step for the experiment. Two samples shown in Section 3.2 were used for this experiment. Spectral reflectance of these samples were captured by the hyperspectral camera, Pika L (Resonon Inc.), which has 900×500 pixels, 12 bits per pixel, and covers a range in 380 nm to 1000 nm. The samples were illuminated with a halogen lamp from directly above. Figure 4.10 shows the experimental setup for data collection.

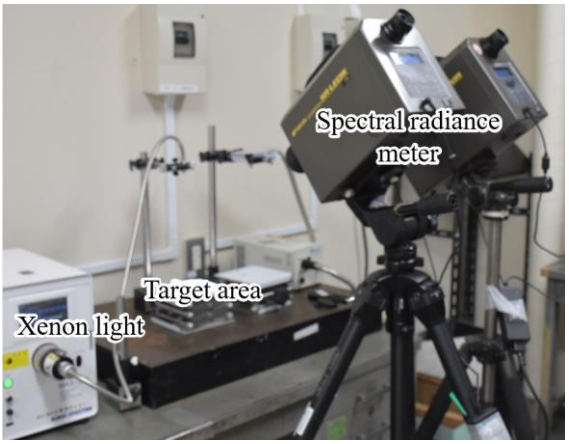

Figure 4.10: Experimental setup for data collection.

Figure 4.11 shows the measured spectral reflectance of samples. In the 400-600 nm region, the spectral reflectance whose sample enclosed in glass cells were almost zero. In contrast, spectral reflectance whose sample was covered with cattle artery tissue was higher tendencies compared to that enclosed in glass cells. These tendencies were caused by tissue scattering tendencies of a cattle artery. Spectral reflectance declined step-by-step by decreasing oxygen saturation in the 600-720 nm region. These characteristics induced by higher absorption of Hb compared to HbO_2.

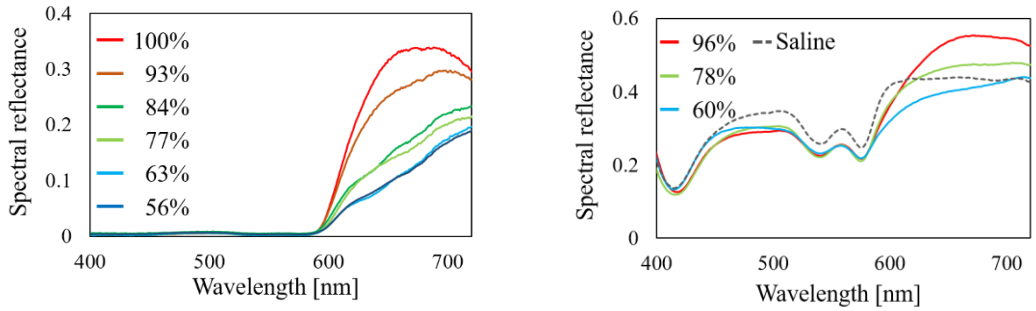

(a) (b)

Figure 4.11: Spectral reflectance of cattle blood samples: (a) Enclosed in glass cell and (b) covered with cattle artery tissue.

4.3.2 Simulation of the optimal illuminant

We used the samples whose spectral reflectance of 100% (H-blood) and 63% (L-blood) as glass-cell-enclosed-sample and 100% (H-blood) and 67% (L-blood) as tissue-covered-sample as the optimization of the illuminant. LED distribution shown in Figure 2.1 whose peak wavelength was 420, 430, 450, 470, 505, 535, 565, 590, 630, 645, 660, 680, 700, and 720 nm were used for the optimization. Figure 4.12 shows the optimized illuminant spectra for cattle blood samples. Both illuminant spectra have the highest peak in the 600-720 nm region and second largest peaks in the 450-550 nm region. The highest peaks are matched with the difference between H-blood and L-blood. Second-largest peaks were thought to satisfy the whiteness of the illuminants. Table 4.4 shows the color difference between H-blood and L-blood samples under the optimal illuminant and the conventional illuminant. For both optimal illuminants, we confirmed the color difference enlargement compare to the conventional illuminant.

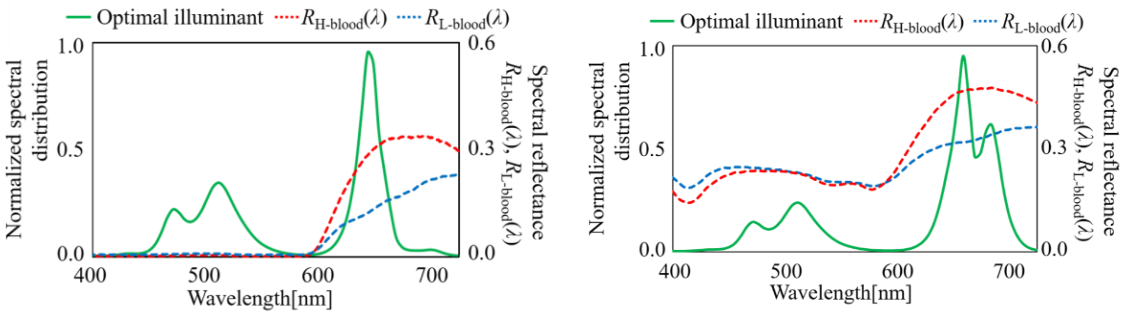

(a) (b)

Figure 4.12: Simulated illuminant spectra for cattle blood samples: (a) Blood samples enclosed in glass cell and (b) blood samples covered with cattle artery tissue.

Table 4.4: Color difference between H-blood and L-blood sample under the optimal illuminant and the conventional illuminant.

	Enclosed glass cell		Covered with tissue	
	Conventional illuminant	Optimal illuminant	Conventional illuminant	Optimal illuminant
Color difference ΔE' (H-blood-L-blood)	4.85	7.87	1.60	6.29
Color difference ΔE' (Whiteness)	0.00	1.4×10^{-3}	0.00	1.1×10^{-2}

4.3.3 Evaluation experiment

Arterial tissue were prepared as same as data collection (described in 3.2). Five types of SO_2 (90 %, 85 %, 77 %, 70 % and 66 %) were enclosed in glass cells and six kinds of SO_2 (100 %, 95 %, 89 %, 86 %, 80 % and 78 %) were covered with cattle artery tissue.

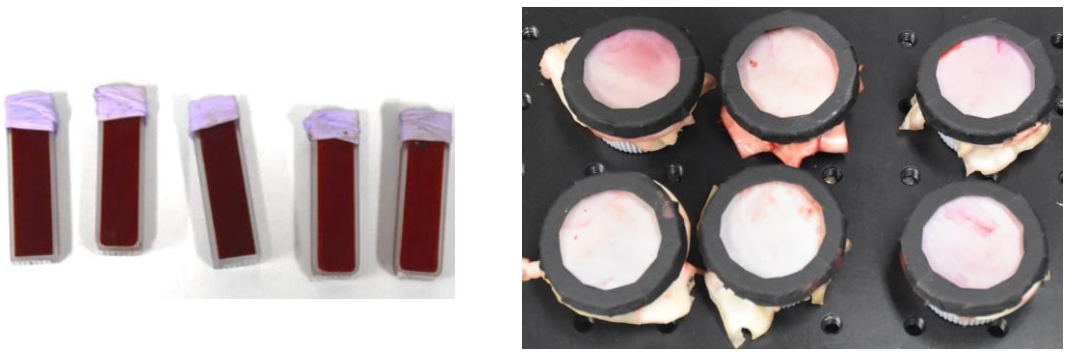

(a) (b)

Figure 4.13: Prepared samples for the evaluation experiment: (a) Blood samples enclosed in glass cells and (b) blood samples covered with cattle artery tissue.

Two illuminant conditions, the optimal illuminant and the reproduced conventional illuminant, irradiated the target from the top of the target region. Observers evaluated the samples 45° angles from the target surface. Figure 4.14 shows the experimental setup for subjective evaluations.

For enclosed-glass-cell samples, we performed two kinds of tasks for the evaluation experiment. The first task was to compare two samples and find the higher oxygen saturation samples. The second task was to sort all five samples from lower oxygen saturation to the highest oxygen saturation one. The higher oxygen saturation samples were defined as reddish and brighter ones. For tissue covered samples, only one task, to

compare each sample color (95 %, 89%, 86%, 80 %, and 78 %) to the reference sample, oxygen saturation: 100% was conducted. Eight observers joined these experiments (not medical doctors, with normal color vision).

The simulated color samples under the optimal illuminant were easier to distinguish compared to that under the conventional illuminant. For the comparison task, subjective evaluation results for two illuminant conditions were different for whole tasks ($p = 2.7 \times 10^{-2}$). For the sorting task, the percentage of correct answer under the optimal illuminant was higher than that under the conventional illuminant. Figure 4.15 shows the evaluation experiment results for the samples enclosed in glass cells. Figure 4.15 (a) shows the simulated colors of blood samples by measured hyperspectral images and Figure 4.15 (b) shows validity for each task.

The simulated color samples under the optimal illuminant were changed in color tone and color brightness, but these samples under the conventional illuminant were changed in only color brightness. Two illuminant conditions were significantly different for whole tasks ($p = 7.0 \times 10^{-2}$) and we confirmed the effectiveness of the optimal illuminant. Figure 4.16 shows evaluation experiment results for the samples covered with cattle artery tissue. Figure 4.16 (a) shows the simulated colors of blood samples by measured hyperspectral images and Figure 4.16 (b) shows validity for the task.

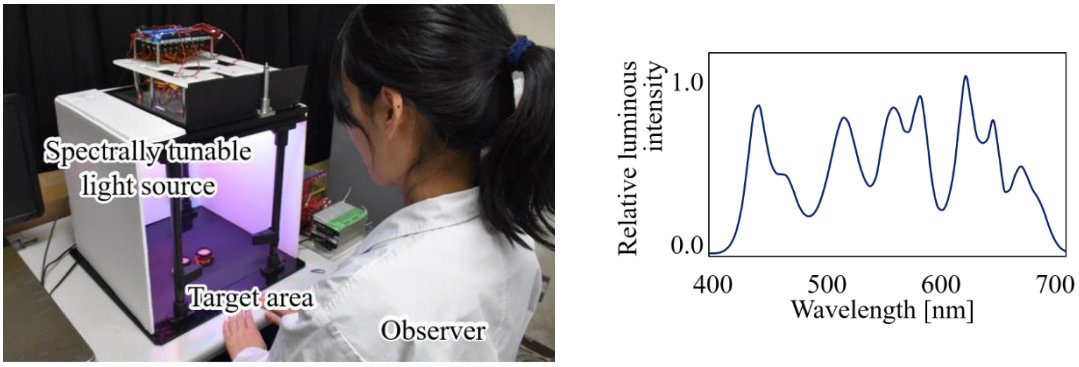

(a) (b)

Figure 4.14: Experimental setup for the evaluation of the optimal illuminants: (a) Experimental setup and (b) reproduced conventional illuminant by using spectrally tunable light source: Second generation.

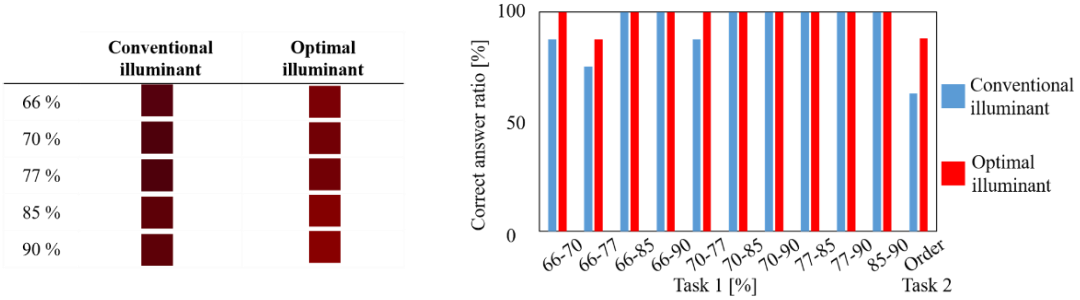

(a) (b)

Figure 4.15: Evaluation results enclosed in glass cells: (a) Simulated color under the optimal illuminant and the conventional illuminant and (b) correct answer ration for task 1 and task 2.

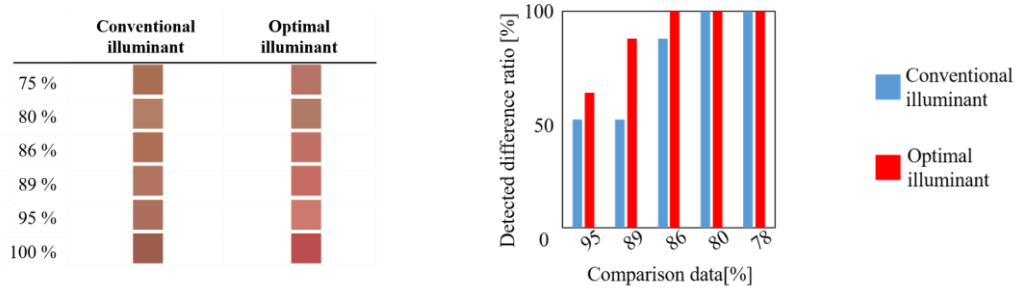

(a) (b)

Figure 4.16: Evaluation experiment results covered with tissue: (a) Simulated color under the optimal illuminant and the conventional illuminant and (b) detected difference ratio to the SO_2 100% sample.

4.4 Application for disease model: Skin flap necrosis

4.4.1 Data collection

As a developmental validation target, we set the optimization target for early diagnosis of skin flap necrosis. In Section 4.4, we designed the optimal illuminant for early stage of ischemia model detection to aid in visual diagnosis. The skin flap chamber: first generation was used for data collection. Figure 4.17 shows the experimental environment for hyper spectral image. Spectral reflectance of these samples was captured by the hyperspectral camera, Pika L (Resonon Inc.). This camera

has 900×500 pixels resolution, 12 bits per pixel, and covers a range in 380 nm to 1000 nm. A skin flap region was fixed so as not to move by body motion during scanning target regions. We captured images every 3 hours until one day after ligation of the left superficial epigastric artery. Measurements were taken every 6 hours until the end of the second day and every 12 hours until the third day. The necrosis region was registered manually by using the image captured after 72 hours of ligation. We used 3-hour-after images for early diagnosis for the designing and evaluation for this optimal illuminant.

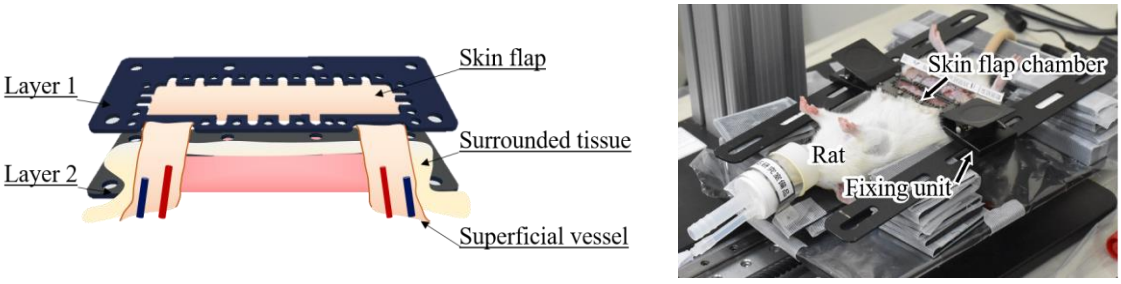

(a) (b)

Figure 4.17: Image capturing environment for skin flap model: (a) Skin flap model fixed by skin flap chamber, and (b) image capturing environment.

We set three regions, survived region, border region, and necrosis region in the early ischemia model for comparing spectral reflectance tendency. The survived region was the region whose tissue kept healthy during the whole measurement. The border region was the region whose tissue color seems healthy until the mid-term of the measurement, but finally the region turned to necrosis status. The necrosis region was set as the region whose characteristics were changed at the beginning of the measurements. Figure 4.18 (b), (c), and (d) shows spectral reflectance for each region. In the necrosis region, spectral reflectance characteristics were different compared to survival regions and border regions due to Hb absorption. In the survival region and border region, spectral reflectance characteristics were almost the same in 0-hour-after-ligation measurement. In contrast, two region's characteristics were changed in 3 hours after ligation measurement. Therefore, we set 3 hours after the ligation image as the target of the designing illuminant spectrum for early diagnosis of skin flap necrosis and conducted an evaluation experiment by computer simulation.

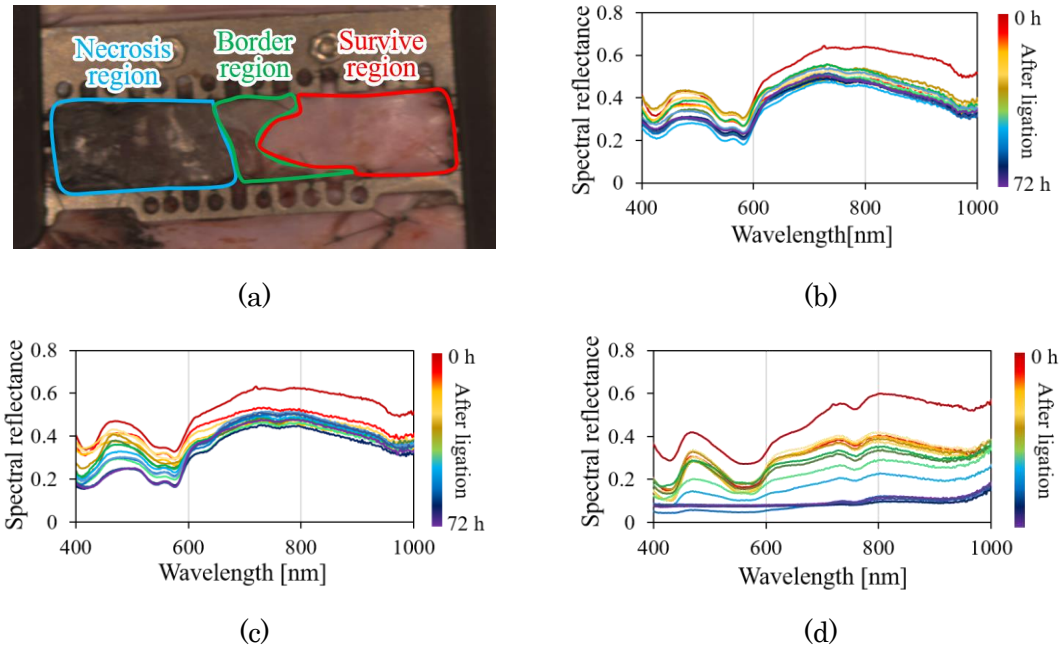

Figure 4.18: Spectral reflectance is comparing by three types of stages: (a) Manually selected three types of regions by using a hyperspectral image, which captured 36 hours after ligation, (b) spectral reflectance of survived region, (c) spectral reflectance of border region, and (d) spectral reflectance of necrosis region.

The degree of oxygenation of the contained hemoglobin status is thought to be the major difference between the survived region and other regions. Since Hb and HbO_2 have isosbestic points, we divided three regions' spectral reflectance and compared the oxygenated degree difference. Figure 4.19 shows spectral reflectance divided by isosbestic point, 525 nm. The survived region's spectrum corresponding to HbO_2 tendency compares to the other two regions. It may be caused by less arterial blood supply by ligation of the superficial epigastric artery.

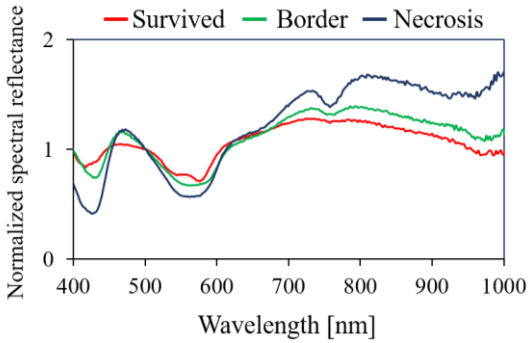

Figure 4.19: The difference between the three regions 3 hours after ligation.

4.4.2 Simulation of the optimal illuminant

To optimize the illuminant spectrum for enhancing the necrosis region in the early stage of skin flap necrosis, we used two kinds of spectral reflectance, the survival region, and the border region, whose spectral reflectance was divided by isosbestic point (Figure 4.19). We used LED distributions shown in Figure 2.1, 14 kinds of LEDs implemented in the spectrally tunable light source: second generation. We also used Skylux Crystal (Yamada Shadowless Lamp Co. Ltd.) as the conventional illuminant.
Figure 4.20 shows the calculated optimal illuminant spectrum. The calculated spectrum has two peaks and these peaks matched the difference between two normalized spectral reflectance. Therefore, the calculated illuminant spectrum seems to enhance the difference between two regions. Table 4.5 is showing the calculated color difference between the survived region and the border region. Figure 4.21 shows the simulated images using hyperspectral images. The color tone under the optimal illuminant was enhanced compared to the conventional illuminant. Therefore, we confirmed the effectiveness of the optimal illuminant for early diagnosis of the necrosis region.

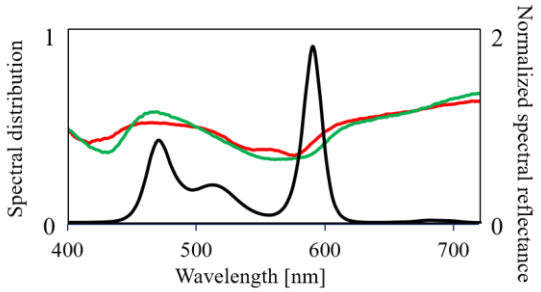

Figure 4.20: Optimal illuminant spectra for early diagnosis of skin flap necrosis(black line), normalized spectral reflectance: normal (red line), and border (green line).

Table 4.5: Color differences between two regions under the conventional illuminant and the optimal illuminant.

	Conventional illuminant	Optimal illuminant
Color difference ΔE' (Border-Survive)	3.11	7.41
Color difference ΔE' (Whiteness)	0.00	4.0×10^{-3}

(a) (b)

Figure 4.21: Simulated images under the conventional illuminant and the optimal illuminant. (a) Skin flap region under the conventional illuminant. (b) Skin flap region under the optimal illuminant.

Chapter 5 Surgical illuminant optimization for blood vessel enhancement

During surgical procedures, blood vessel structures are one of the essential factors for visual diagnosis. In this chapter, we focus on blood vessel structures for validation and the subjective evaluation. First, we describe the optimization method for enhancing the blood vessel structures. This method is based on the optimization method shown in Section 4.1, though in this chapter it is changed in enhancement degree in blood vessel structures. In Section 5.1, we design an optimal illuminant for enhancing the blood vessel structures. We conducted a subjective evaluation in Section 5.3.1. After the evaluation experiment, we calculated the evaluation index based on the method describe in Section 5.3.2. Finally, in Section 5.4, we present an evaluation experiment and the evaluation of effect of the optimal illuminant.

5.1 Optimization method

We designed the optimal illuminant that can enhance the blood vessel structures while illuminant color preserved white as same as described in Section 4.1.2. We used color appearance model CIECAM02 to calculate the index for simulation of the optimal illuminant. We used contrast values based on CIECAM02 to evaluate the contrast between blood vessel regions and surrounded tissue region. In Section 4.1.2, we used the color difference to evaluate the difference between normal and poor blood circulation conditions. However, the color difference is not matched to evaluate the difference between blood vessels and surrounded tissue because the absorption volume was different. We selected Michelson contrast value [38] to evaluate the color contrast between two regions. We used the lightness value, J', to evaluate the absorption difference for calculation of the enhancement effect. The contrast value between blood vessel regions and surrounded tissue region was calculated using the following equation (5-1):

$$\alpha = \frac{\max\left|J'_{tis}, J'_{ves}\right| - \min\left|J'_{tis}, J'_{ves}\right|}{J'_{tis} + J'_{ves}} \qquad (5\text{-}1)$$

J'_{tis}, J'_{ves} denotes the lightness values of the tissue region and blood vessel region and $|\cdot|$ denotes absolute value inside bracket.

The illuminant color difference between the calculated illuminant color and the conventional illuminant color was calculated based on CIECAM02 as same as described in Section 4.1.2. The spectral distribution of Skylux Crystal (Yamada Shadowless Lamp Co. Ltd.) was used as the conventional illuminant spectrum. The illuminant color difference was defined as the equation (5-2):

$$\beta = \sqrt{\left(\Delta J'/K_L\right)^2 + \Delta a'^2_M + \Delta b'^2_M} \qquad (5\text{-}2)$$

Where $\Delta J'$ represents the difference of lightness value between calculated illuminant distribution and the conventional illuminant. K_L denotes the parameter or the coefficient value, which was K_L =1.0. A combination of $\Delta a'_M$ and $\Delta b'_M$ describes the Cartesian coordinate difference between two illuminant conditions. The optimal illuminant distribution was defined as maximized β under the constraint of $\alpha < 3.0$, based on perceivable limit. We assumed to use the LED distributions implemented in the spectrally tunable light source: second generation. Figure 5.1 shows flow chart of the optimization.

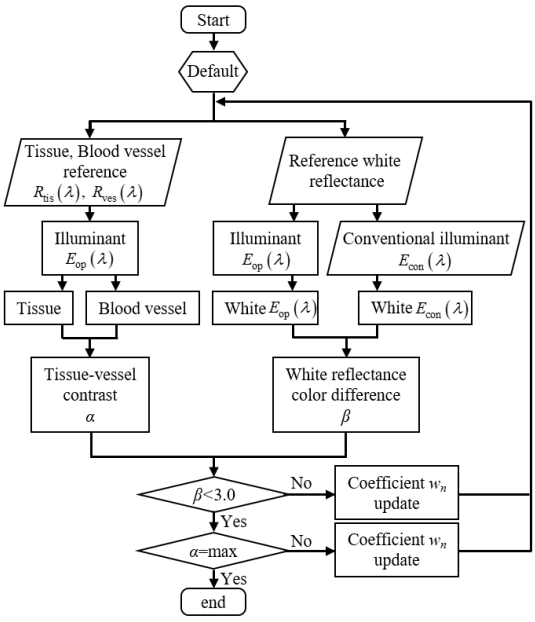

Figure 5.1: Flow chart of the optimization for blood vessel enhancement.

5.2 Optimal illuminant design

5.2.1 Data collection

In this experiment, a rat was used to evaluate the effectiveness of the optimal illuminant that enhances the blood vessel structures. The rat cecum was set on the board, which was described in Section 3.1. We captured hyperspectral images and calculated spectral reflectance. Hyperspectral camera, NH-8 (EBA JAPAN Co.), which has solution of 1200×1024 pixels, 12 bits per pixel, and covers the spectral range from 380 nm to 1000 nm with 5 nm intervals, was used for data collection. The geometry was set as same as Section 4.2.1. Figure 5.2(a) shows the rat's cecum image captured by the hyperspectral camera. The conventional surgical light source (Skylux Crystal, Yamada Shadowless Lamp Co. Ltd.) was used for simulating the RGB image. We evaluate the tissue region's spectral reflectance and vessel region. The blood vessel and peripheral regions were selected from the center part of the cecum. Figure 5.2 (b) shows averaged spectral reflectance of the blood vessel region $R_{ves}(\lambda)$ and the peripheral region $R_{tis}(\lambda)$. Two spectral references are remarkably different between 400-600 nm, while 600-720 nm were similar trends. $R_{ves}(\lambda)$ shows a lower tendency than $R_{tis}(\lambda)$ between 400 and 600 nm, whose region was high absorbance values compared to the longer wavelength region. The main content in the blood vessel is the red blood cells. By contrast, the tissue region does not contain much red blood cells. The difference between two regions occurred by the hemoglobin content, a dominant absorber in a visible range in a living organism. This tendency is caused by high absorption coefficient in 400-600 nm region and high tissue scattering characteristics in long-wavelength region.

(a)

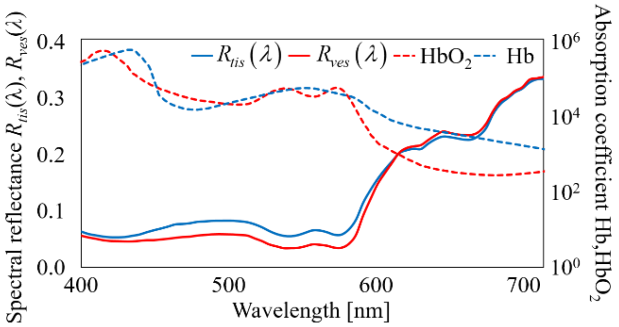

(b)

Figure 5.2: Captured hyperspectral image and spectral reflectance: (a) Rat cecum image simulated by using hyperspectral image, and (b) spectral reflectance of tissue region and blood vessel region.

5.2.2 Simulation of the optimal illuminant

The spectral reflectance of two regions, $R_{tis}(\lambda)$ and $R_{ves}(\lambda)$, were used to simulate the optimal illuminant. LED distribution shown in Figure 2.1 whose peak wavelength was 420, 430, 450, 470, 505, 525, 565, 590, 630, 645, 660, 680, 700, and 720 nm were used for the illuminant optimization. The solid line in Figure 5.3 shows the optimized illuminant spectrum for vessel structure enhancement. The illuminant spectrum has two peaks around 420 nm and 565 nm. These characteristics matched the spectral reflectance difference between 400-600 nm. Table 5.1 shows the calculated color difference between the conventional illuminant and the optimal illuminant and the contrast value between tissue region and blood vessel regions. The contrast value under the optimal illuminant was enlarged compared to the conventional illuminant; hence, we confirmed the effect of the illuminant in computer simulation. We defined the optimal illuminant spectrum as White-Color-Preserving Illuminant, WCPEI.

Hence, we investigated a tissue-color preserving illuminant for keeping tissue color as same as the conventional illuminant to add LED whose peak wavelength exceeding 600 nm since the tissue color under the WCPEI thought to be changed compared to the conventional illuminant. We selected one kind of LED whose peak wavelength was 630 nm so as not to decline the contrast between tissue and blood vessel region. The dotted line in Figure 5.3 shows the spectral distribution of tissue-color preserving illuminant. Since tissue-color preserving degree and enhancement of blood vessel structure is a trade-off relationship, we assume to adjust enhancement or tissue-color preserving rate for controlling the intensity of 630-nm-LED. We defined the Tissue-Color Preserving Illuminant as TCPI.

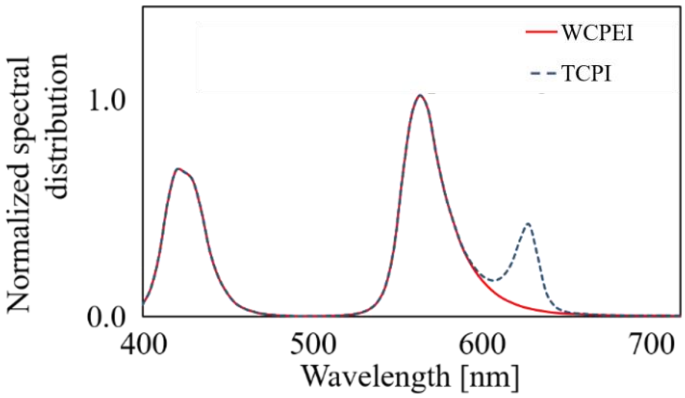

Figure 5.3: The optimized illuminant spectrum for blood vessel structure enhancement.

Table 5.1: Calculated values of α and β for the blood vessel enhancement illuminant.

	Conventional illuminant (Skylux Crystal)	WCPEI	TCPI
Contrast between tissue and blood vessel; α	2.22×10^{-1}	3.24×10^{-1}	2.27×10^{-1}
Whiteness condition; β	0.00	2.95	5.57

Figure 5.4 shows simulated RGB images under each illuminant condition using the hyperspectral image. The spectral reflectance was calculated pixel-by-pixel as a first step for simulating these illuminants. Next, the illuminant spectra multiplied by spectral reflectance to mimic the reflected light whose spectra were simulated by the experiments. The value of XYZ stimuli were calculated by multiplying the spectra of XYZ stimuli and spectral reflectance, and summarized it in the visible range. After that, XYZ values were converted to sRGB via the conversion matrix. Blood vessels under the WCPEI observed the most accentuated compare to those under the conventional illuminant. Tissue color under the TCPI was almost the same as that under the conventional illuminant, but the vessel structures are enhanced compared to the conventional illuminant.

(a) (b) (c)

Figure 5.4: Simulated images of rat cecum: (a) Assumed to use the conventional illuminant spectrum, (b) assumed to use the optimized illuminant spectrum (WCPEI), and (c) assumed to use the tissue-color preserved illuminant (TCPI).

Contrast values under each illuminant were also generated by using the hyperspectral image. The contrast values β were calculated each pixel by equation (5-1). Reference value J'_{tis} were set as an averaged spectral reflectance of tissue region. Three

ROI regions were selected from three blood vessel regions and surrounding tissues. Figure 5.5 shows contrast images and three ROI regions set on surface of the rat cecum. Contrast value remains high values in contrast image of the WCPEI and the TCPI compared to that of the STCI. These tendencies caused by enhancing effect by optimized illuminants. Contrast values especially branching vessels under the WCPEI were higher compared to that under the TCPI. From these results, the WCPEI thought to be able to enhance microvasculature regions.

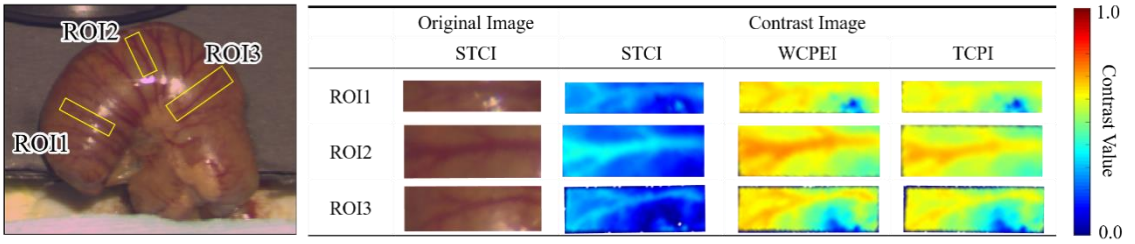

Figure 5.5: Contrast images under the STCI, the WCPEI, and the TCPI.

The effect of the WCPEI seems to be caused by narrow-band illuminant which restrict the illuminant wavelength characteristics to a specific wavelength band. For comparing the FWHM and contrast values between tissue and blood vessels, simulation analysis was also conducted by calculating the contrast values. Four kinds of illuminants, FWHM 15nm, 30 nm, 60 nm, and 90 nm, and its peak wavelength was 505 nm, were selected by the most contrast-enhanced one from the spectrally tunable light source: second generation. Figure 5.6 (a) shows spectral distributions used in this simulation analysis. Figure 5.6 (b) - (e) shows simulated images under the four kinds of FWHM: 15 nm, 30 nm, 60 nm, and 90 nm, peak wavelength: 505 nm. The contrast values were declined by changing the FWHM values declining. Therefore, we confirmed the effect of blood vessel enhancement by narrow-band illuminant.

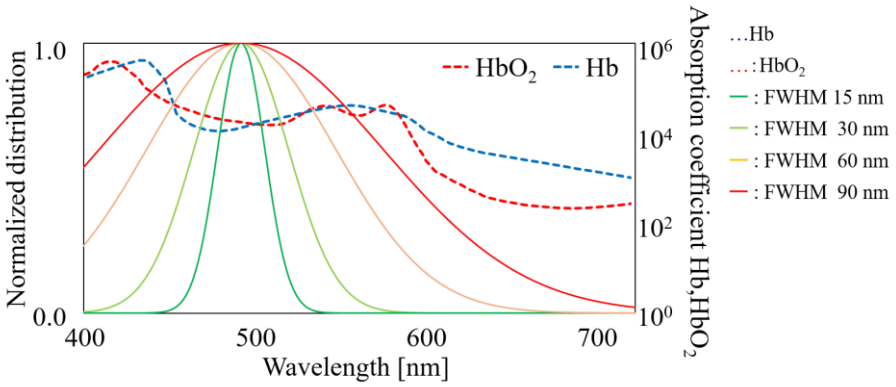

(a)

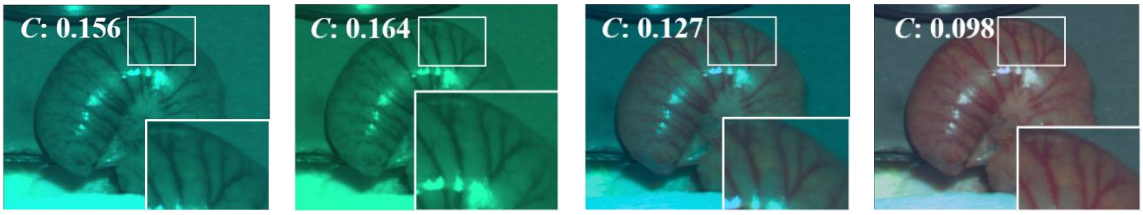

(b) (c) (d) (e)

Figure 5.6: Contrast changing by controlling full width half maximum with contrast value *C*: (a) Spectral distributions of illuminants and absorption coefficients, (b) FWHM: 15 nm, (c) FWHM: 30 nm, (d) FWHM: 60 nm, and (e) FWHM: 90 nm.

5.3 Subjective evaluation setup

5.3.1 Environment of the evaluation experiment

We evaluated the effectiveness of simulated illuminants by measuring the visible vessel ratio to a vessel image. A vessel image was captured under the 505 nm LED illuminant since we can capture the most enhanced blood vessel images by high absorbing characteristics of Hb and HbO_2 under this LED illuminant. We selected the LED that implemented in the spectrally tunable light source: second generation. The visible vessel ratio *C* was measured under the WCPEI, the TCPI, and the STCI. We used a monochromatic camera (VCXU-23M, Baumer Co., Ltd) for capturing the blood vessel images. Figure 5.7(a) shows contrast values for 15 kinds of LEDs and the spectral coefficient of Hb and HbO_2. Hence, the 505 nm LED's contrast values were the most enhanced, so we defined this blood vessel image as the 505 nm image.

We conducted subjective evaluation experiments for evaluation of the optimal illuminant. The observers evaluated visible vessel regions under three conditions of the

illuminants, the WCPEI, the TCPI, and the STCI for the subjective evaluation experiments. We set two ROIs on the surface of a rat cecum. The spectrally tunable light source was set on just above the target regions. Each illuminant intensity was equivalent by measuring luminance with a luminance meter (T-10, Minolta Co., Ltd). Observers viewed the target regions through the loupe, O-Light F (Otsuka Optics Co., Ltd) for magnifying the target regions 200 % from the naked eye view. Figure 5.8 (a) shows the experimental environment for the evaluation experiment.

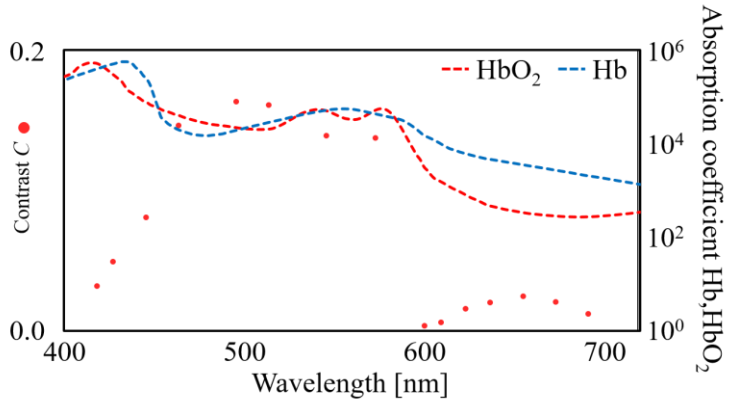

(a)

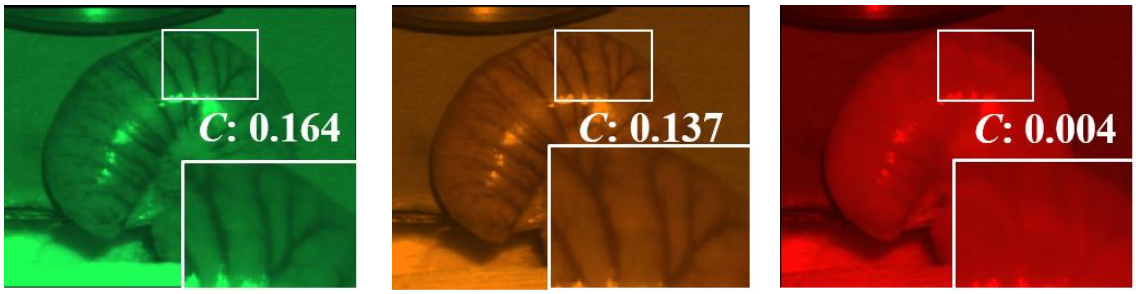

(b) (c) (d)

Figure 5.7: Contrast values for each LED: (a) Contrast value between tissue and blood vessel region for 15 kinds of LEDs, (b) simulated image under the LED: peak wavelength 505 nm, (c) simulated image under the LED: peak wavelength 590 nm and (d) simulated image under the LED: peak wavelength 625 nm.

The 505 nm image was sent to the tablet personal computer, and observers verified the detected vessel regions by marking them to the 505 nm image. Observers wrote these regions on the 505 nm images by using a stylus pen. Blood vessel regions for each ROI were marked on the 505 nm images manually after subjective evaluation experiments. We used these regions as ground truth (GT), and compared the detected vessel regions by comparing them to the GT.

Five observers per one rat sample joined this evaluation experiment. All observers were 22 to 24 years old, not medical doctors, and had normal vision. They had been trained to draw vessel regions on the tablet PC before the evaluation experiment. The order of illuminant conditions was randomly changed for each observer. Observers gazed at a white plate under each illuminant condition for one minute after changing the illuminant condition for illuminant color adaption.

These evaluation experiments were conducted in the darkroom without effect from outside light. Each evaluation step to view the vessel regions and draw the vessel regions took two minutes per one illuminant condition for each ROI. Figure 5.8 (b) show experimental time chart for the experiment.

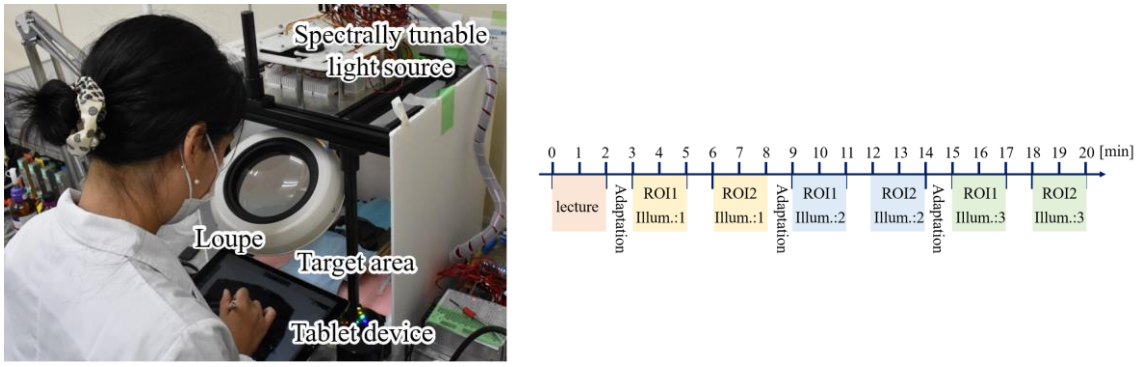

Figure 5.8: Experimental condition for the evaluation experiment: (a) Experimental environment for the subjective evaluation and (b) evaluation experiment flow.

5.3.2 Evaluation index

Detected vessel ratios were calculated by comparing the drawn vessel regions to the GT for quantitative evaluation. As a first step, the detected vessel regions were extracted from monochromatic images and skeletonized for defining the drawn regions. Unintended touches while writing the viewed vessel regions were deleted for calculation of detected vessel ratio. The vessel regions in the GT were dilated and overlaid to the extracted vessel regions on the subjective image. The dilated GT image's overlapping region and the skeletonized subjective image were extracted and defined as truly written vessel regions. These vessel regions in the subjective image were skeletonized. They projected to the blood vessels in the GT image for linking the vessel regions in the subjective images to the blood vessels in the GT image. Finally, we compared the length of the projected vessel region to the GT image. We defined the detected vessel region as follows:

$$C = \frac{\sum l_{subject}}{\sum l_{correct}} \qquad (5\text{-}3)$$

where $\sum l_{correct}$ and $\sum l_{subject}$ are the total blood vessel length in the skeletonized GT images and projected subjective images. Figure 5.9 shows the calculation flow for the detected blood vessel ratio. For the statistic evaluation, calculated C values between the WCPEI, the TCPI, and the STCI were compared by a paired-t-test.

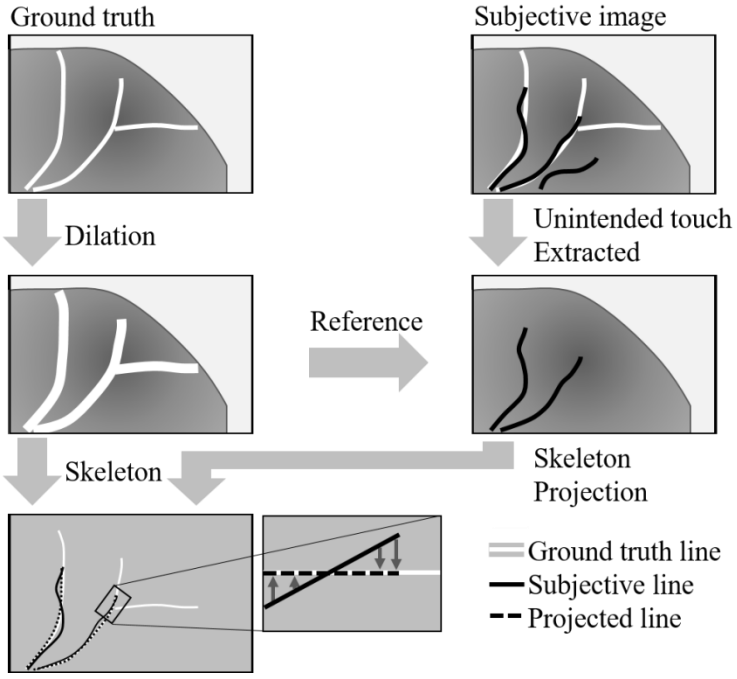

Figure 5.9: Calculation flow for the evaluation index.

5.4 Subjective evaluation experiment

We conducted a subjective evaluation experiment using three rat samples (SLC: Wistar, 12-14 weeks old, male). The ROI regions were selected from the middle of the rat cecum. Each region was surrounded by drapes to clarify the target regions. Figure 5.10 (a) shows target ROI settings selected from the rat cecum surface. Figure 5.10 (b) shows the captured 505 nm images under the LED, whose peak wavelength was 505 nm. Figure 5.10 (c) shows the manually selected blood vessel region images which were used as GT. The red lines were selected as blood vessel regions. Figure 5.10 (d) shows skeletonized blood vessel regions which were separated into two kinds of vessels: main

vessels and branching vessels.

We calculated two kinds of detected vessel ratio *C*, the whole vessel region and the branching vessel regions, which was selected manually from GT images. The effect of the optimal illuminant for branching vessel region was calculated for evaluation of thinner vessel regions.

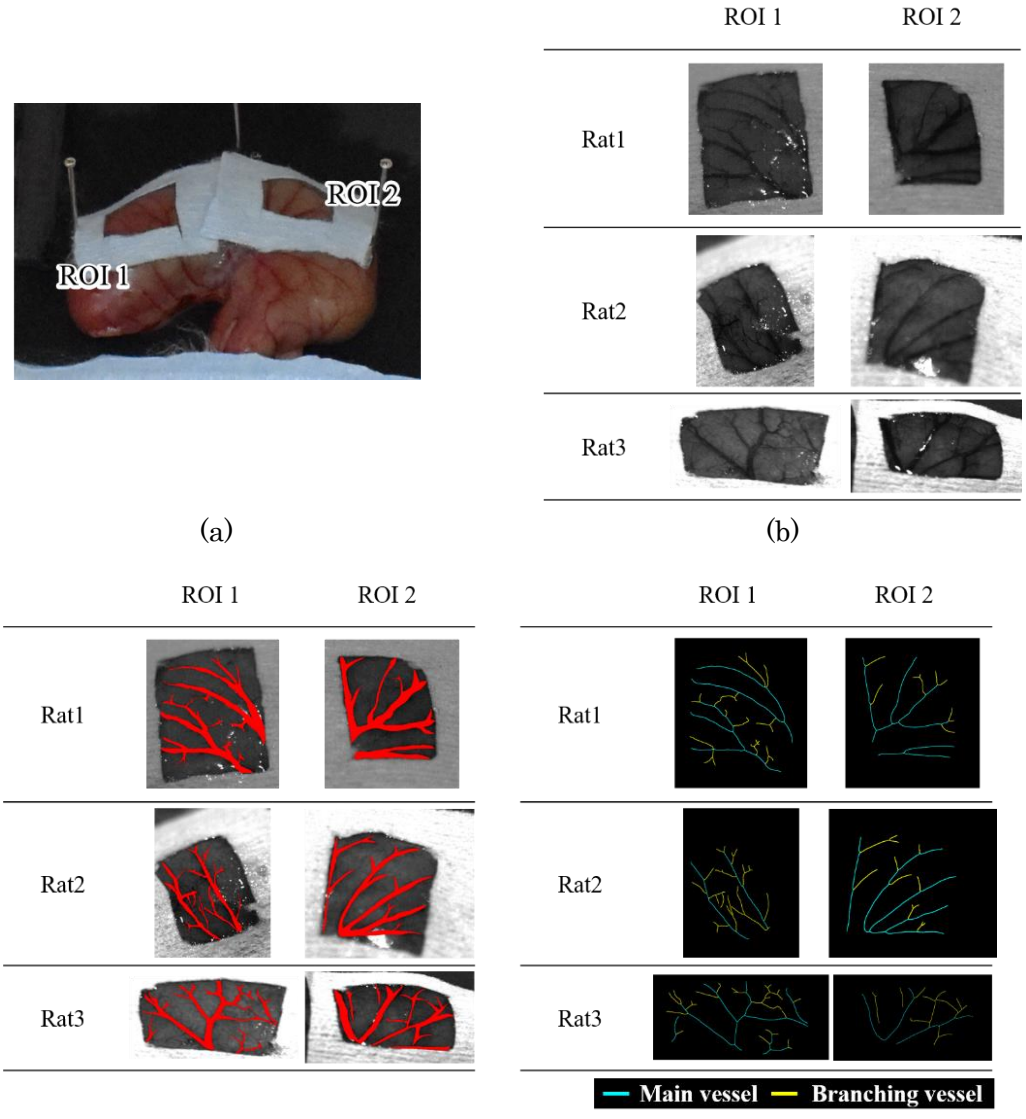

Figure 5.10: Region of interest for the subjective evaluations: (a) ROI regions on the surface of rat cecum, (b) the captured 505 nm images by monochromatic camera, (c)manually selected GT images, and (d) thinning GT images whose vessel regions were separated into main vessels and branching vessels.

5.4.1 Evaluation experiment for the WCPEI

Two kinds of detected vessel ratio *C,* total vessels and branching vessels, were calculated for each ROI. The effectiveness of the WCPEI was confirmed by using t-test. Figure 5.11 to Figure 5.13 show subjective evaluation results for the WCPEI.

Figure 5.11 (a) shows subjective images and projection images for rat 1, ROI 1, and ROI 2, pick out from 5 observers' results. For ROI 1, the branching vessels between two sets of vessels were detected under the WCPEI, though it was not detected under the STCI (yellow allow). In OB 3 for ROI 1, vessels on top of the images were detected under the WCPEI, not under the STCI. In ROI 2 – OB 1, the bottom region of vessels shows a difference between under the STCI and the WCPEI. In contrast, for ROI 2 – OB 3, the detected vessel structures were almost identical, but the shape of vessels under the WCPEI was more precise than that under the STCI.

Figure 5.11 (b) and (c) shows the detected vessel ratios, for total vessel and branching vessels for rat 1, under the STCI and the WCPEI. The detected vessel ratios under the WCPEI were more significant than those under the STCI in almost all cases, especially in branching vessel regions. We conducted a paired t-test to compare two results and confirmed the significant difference between two illuminant conditions (total vessels for ROI 1: $P = 4.58\times10^{-3}$, ROI 2: $P = 3.90\times10^{-3}$, branching vessels for ROI 1: $P = 1.13\times10^{-2}$, ROI 2: $P = 2.34\times10^{-2}$).

Figure 5.12 (a) shows excerpt subjective images and projections images from 5 observers for rat 2, ROI 1, and ROI 2, respectively. In ROI 1-OB1, small branching vessels around the left side vessel block under the WCPEI were detected finer than that under the STCI (yellow allows). In ROI 1 – OB 3, the small branching vessels under the WCPEI were detected better than those under the STCI. Under the WCPEI, fuzzy vessel structures were easy to be viewed compared to that under the STCI (in ROI 2 – OB 3: middle region of left vessel block, and in ROI 2 – OB 5, left vessel block).

Figure 5.12 (b) and (c) shows the detected vessel ratios, for total vessel and branching vessels, under two illuminant conditions. The detected vessel ratios under the WCPEI were better compared to those under the STCI. The paired t-test shows a remarkable difference between the two illuminant conditions (total vessels for ROI 1: $P = 6.07\times10^{-3}$, ROI 2: $P = 4.16\times10^{-3}$, branching vessels for ROI 1: $P = 1.19\times10^{-2}$, ROI 2: $P = 3.16\times10^{-2}$).

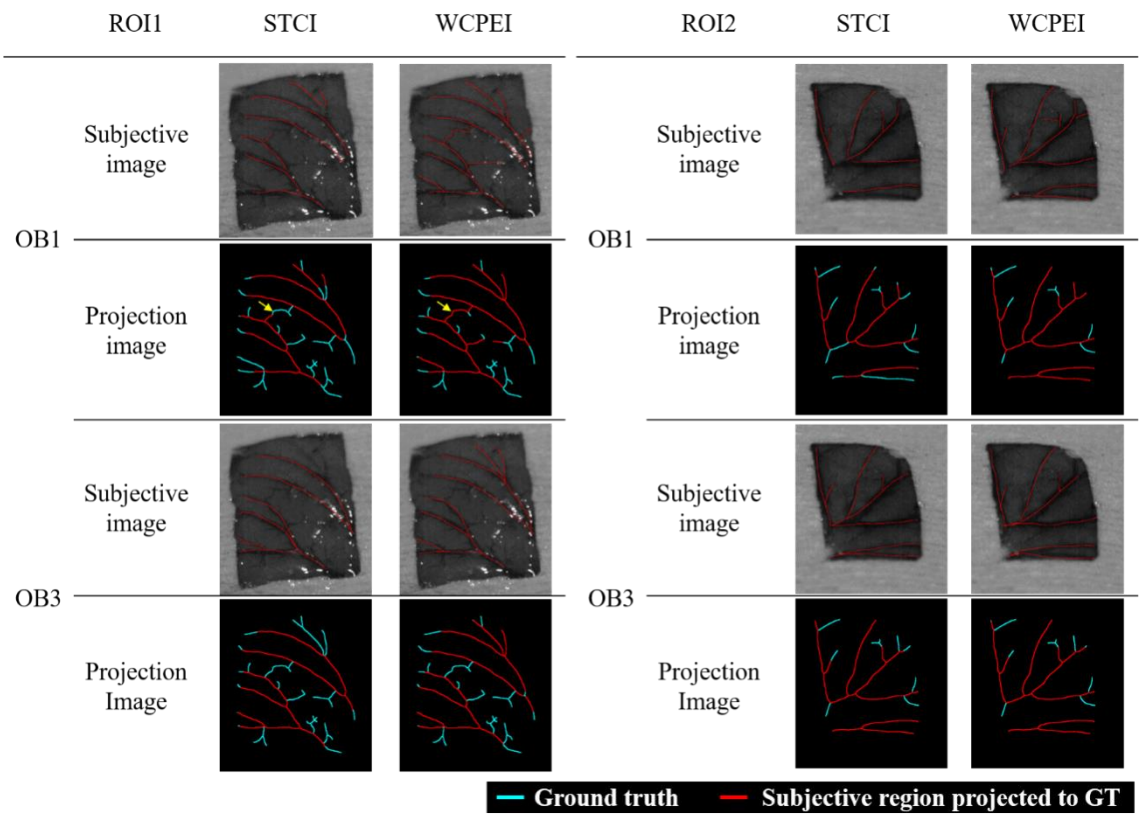

(a)

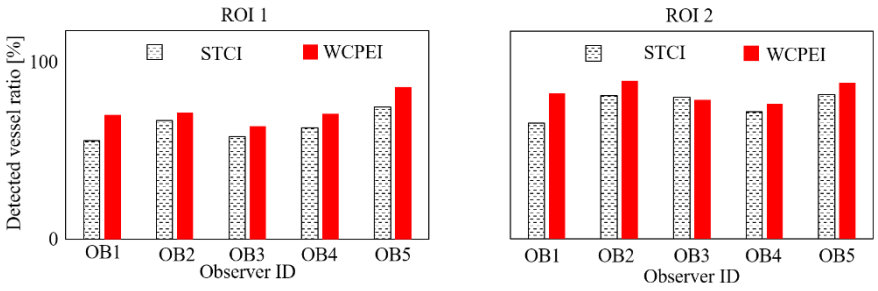

(b)

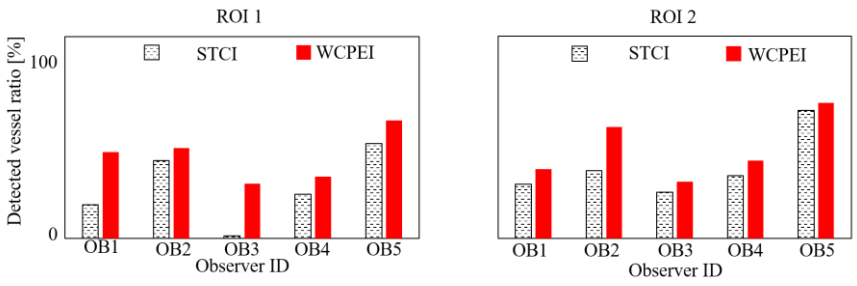

(c)

Figure 5.11: Evaluation experiment results by WCPEI for rat 1: (a) Subjective and projection images, (b) detected vessel ratio for whole vessels, and (c) branching vessels.

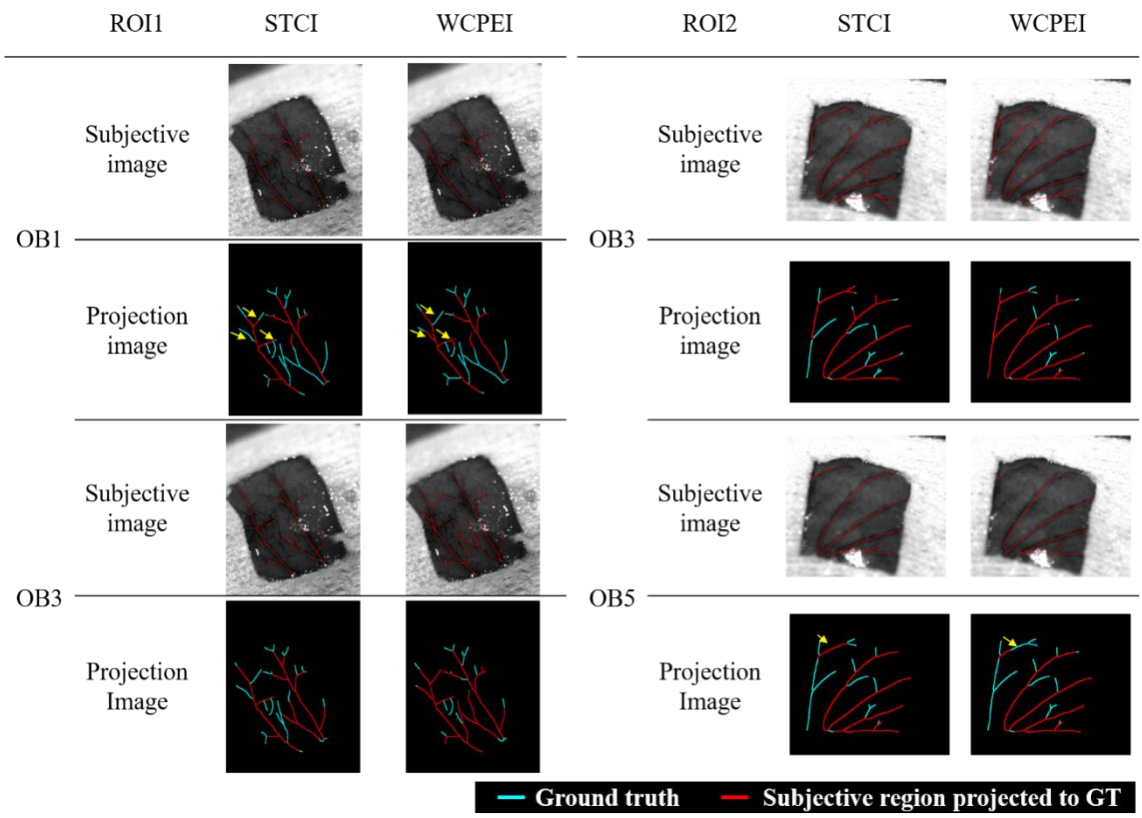

(a)

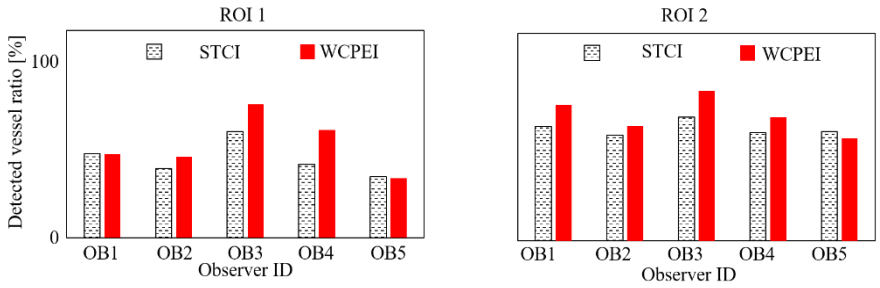

(b)

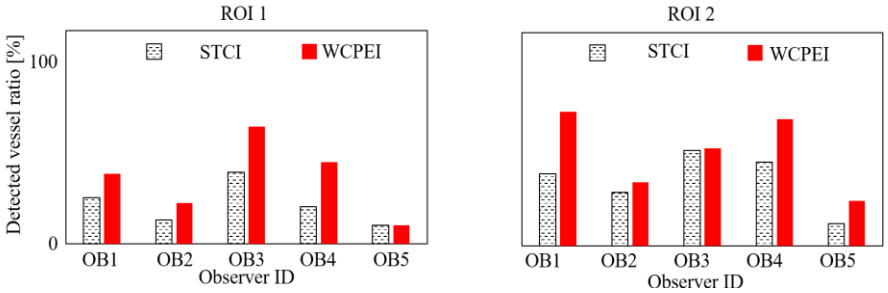

(c)

Figure 5.12: Evaluation experiment result by WCPEI for rat 2: (a) Subjective and projection images, (b) detected vessel ratio for whole vessels, and (c) branching vessels.

Figure 5.13 (a) shows subjective images and projection images for rat 3, ROI 1, and ROI 2, pick up from 5 observers' results. In ROI 1 – OB 1, the branching vessel regions under the WCPEI were observed more straightforward than those under the STCI (yellow allows). In ROI 1 – OB 4, two images had almost the same tendency. In ROI 2 – OB 3, the detected vessel regions were almost the same, but the connecting point of vessels under the WCPEI was more precisely compared to that under the STCI.

Figure 5.13 (b) and (c) shows the detected vessel ratios, for total vessel and branching vessels, for rat 3. The ratios for total vessels were similar trends, and a significant difference was not detected between two regions in ROI 1 ($P = 4.71 \times 10^{-2}$). The selection of ROI positions caused these trends. In ROI 1, there are not enough thin vessels compared to the other ROIs. In ROI 1 – OB 4, the detected vessel ratio under the WCPEI was less than that under the STCI since two subject images were almost the same tendency. Therefore, these tendencies may be caused by viewing conditions. In ROI 2, there was also no significant difference ($P = 1.71 \times 10^{-2}$). These results may be caused by viewing conditions or insufficient thin vessels compared to the other ROIs in ROI 2. However, detected vessel ratio for branching vessels in two ROIs shows significant differences (branching vessels for ROI 1: $P = 1.12 \times 10^{-2}$, ROI 2: $P = 5.20 \times 10^{-3}$). These results show that the WCPEI shows effectiveness for especially fine vessels observed in branching vessels.

We applied paired t-test to whole datasets (30 data) for comprehensive WCPEI evaluation. Figure 5.14 shows boxplot of detected vessel ratios for total vessels and branching vessels. We confirmed a significant difference between two illuminant conditions ($P = 1.17 \times 10^{-2}$) and the effect of the WCPEI was indicated through this evaluation experiment.

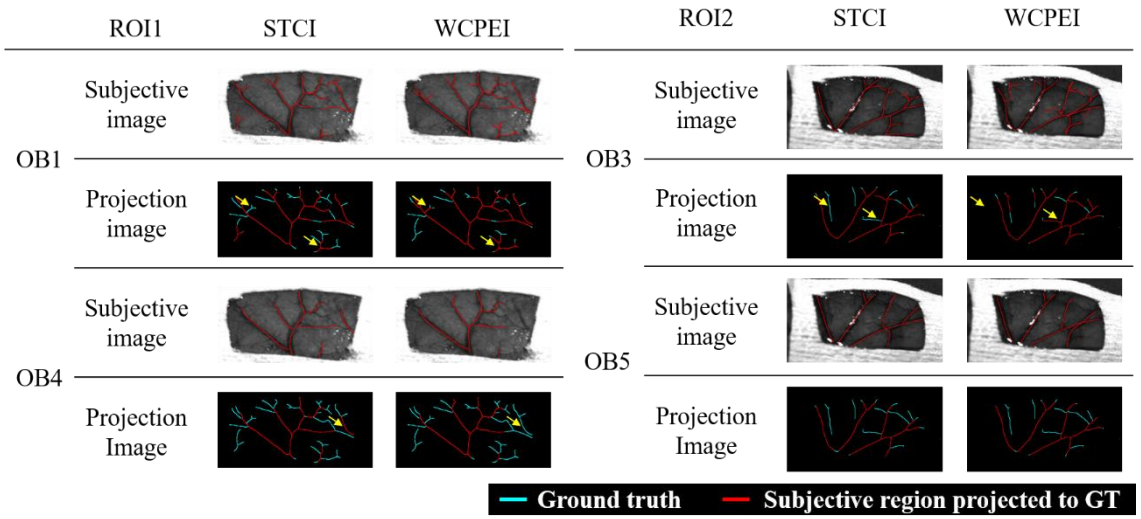

(a)

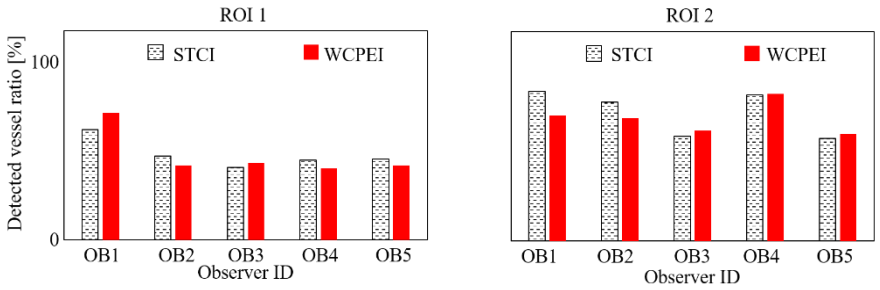

(b)

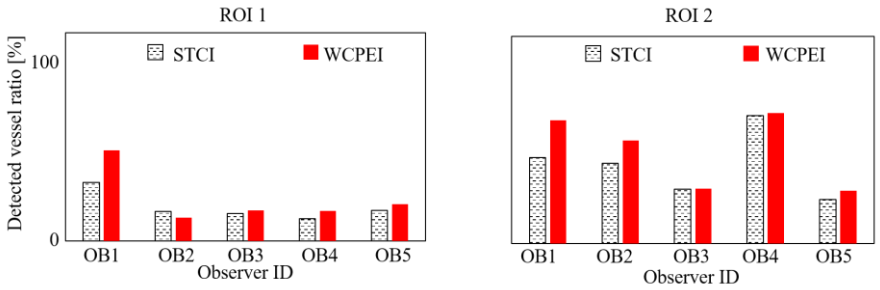

(c)

Figure 5.13: Evaluation experiment results by WCPEI for rat 3: (a) Subjective and projection images, (b) detected vessel ratio for whole vessels, and (c) branching vessels.

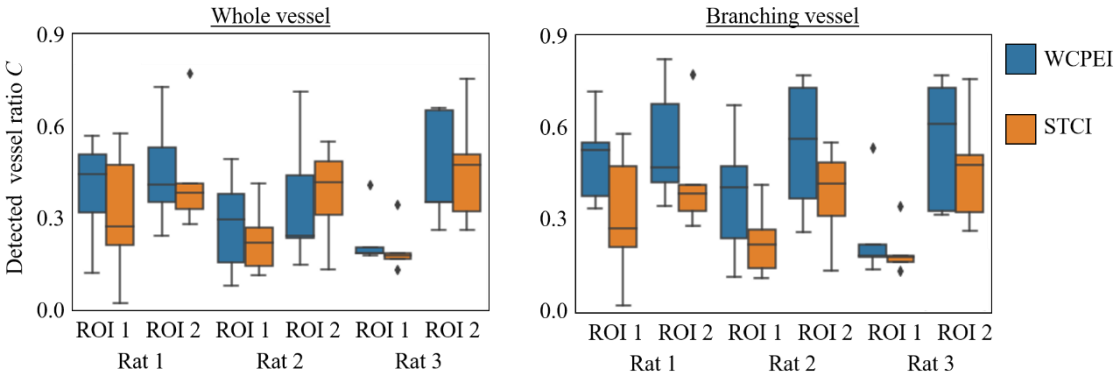

Figure 5.14: Boxplot of detected vessel ratios for total vessels and branching vessels under the WCPEI and the STCI.

5.4.2 Evaluation experiment for TCPEI

Two kinds of detected vessel ratio *C,* for total vessels and branching vessels, were calculated for each ROI. The effectiveness was also confirmed by using t-test. Figure 5.15 to Figure 5.17 show subjective evaluation results for the TCPI.

Figure 5.15 (a) shows subjective images and projection images for rat 1, ROI 1 and ROI 2, respectively. In ROI 1 – OB 1, branching vessels between the upper and lower parts of the vessel region were observed clearer under the TCPI than under the STCI (yellow allow). The fuzzy vessels in the upper site of ROI 1 were detected only under the TCPI in ROI 1-OB 3. In ROI 2 – OB 1, the details of branching vessels were observed clearer under the TCPI than that under the STCI. In contrast, the two results, under the STCI and the WCPEI, were almost the same in ROI 2 – OB 1 and ROI 2 – OB 3.

Figure 5.15 (b) shows detected vessel ratios, for total vessel and branching vessels, for rat 1. In some cases, the detected vessel ratio values were better than those under the STCI, and the difference between the two results was subtle. We conducted a paired t-test, and the difference was not detected (total vessels for ROI 1: $P = 2.9\times10^{-1}$, ROI 2: $P = 1.7\times10^{-1}$, branching vessels for ROI 1: $P = 1.2\times10^{-1}$, ROI 2: $P = 2.9\times10^{-1}$).

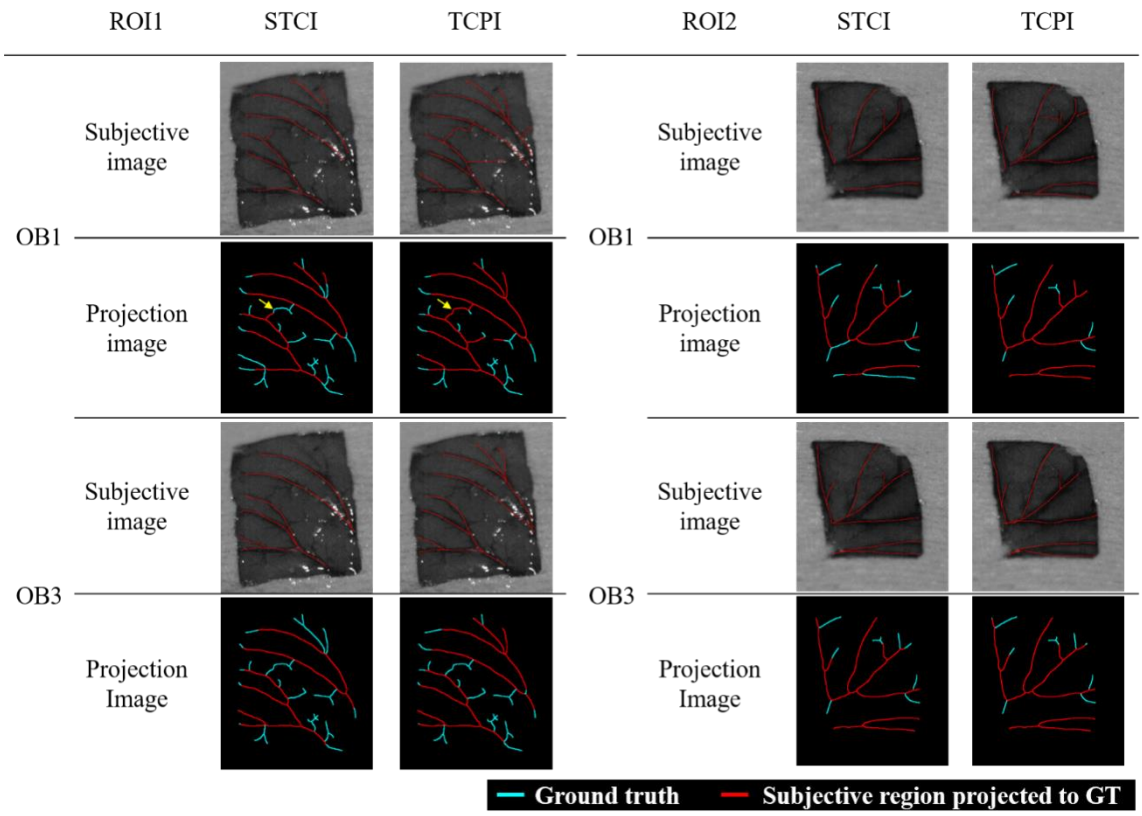

(a)

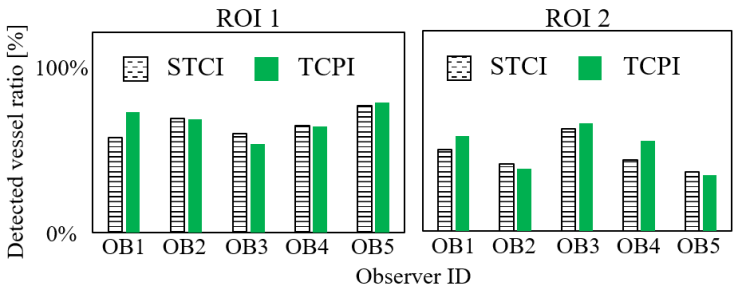

(b)

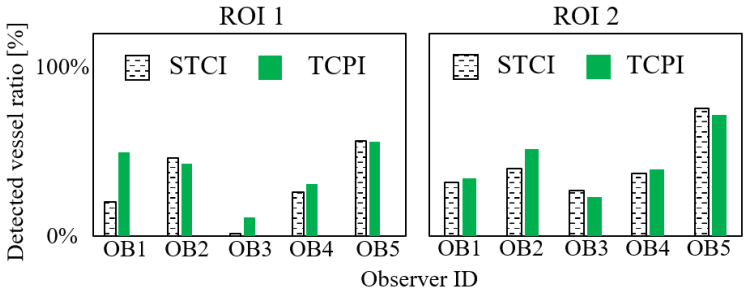

(c)

Figure 5.15: Evaluation experiment results by TCPI for rat 1: (a) Subjective and projection images, (b) detected vessel ratio for whole vessels, and (c)branching vessels.

Figure 5.16 (a) shows subjective images and projection images for rat 2, ROI 1, and ROI 2 typical results from 5 observers'. In ROI 1 – OB 1, small branching vessels under the TCPI were observed more straightforward than those under the STCI. In contrast, the detected vessel regions under the TCPI and the STCI were almost the same in ROI 1 – OB 3.

Figure 5.16 (b) shows the detected vessel ratio for the STCI and the TCPI. In some cases, the detected vessel ratios for the TCPI were better than those under the STCI, but in almost all cases, these values were almost the same. In a paired t-test, the difference between the two illuminant conditions was not confirmed (total vessels for ROI 1: $P = 1.2\times10^{-1}$, ROI 2: $P = 3.2\times10^{-1}$, branching vessels for ROI 1: $P = 1.2\times10^{-1}$, ROI 2: $P = 4.2\times10^{-1}$).

Figure 5.17 (a) shows two image samples from 5 observers for rat 3, ROI 1, and ROI 2. In ROI 1 – OB 1, the branching vessel in the upper part was only detected under the WCPEI, but the lower part was high accuracy under the STCI than under the TCPI. For OB3, the small branching vessels in the right upper part were detected under the TCPI, but branching vessels in the lower part was not detected though these regions were detected under the STCI. In ROI 2, OB 3 and OB 5 were not different between the two illuminant conditions. We conducted a paired-test for comparing two results, but we cannot detect a significant difference between two illuminant conditions (total vessels for ROI 1: $P = 1.7\times10^{-1}$, ROI 2: $P = 1.9\times10^{-1}$, branching vessels for ROI 1: $P = 2.8\times10^{-2}$, ROI 2: $P = 4.4\times10^{-1}$).

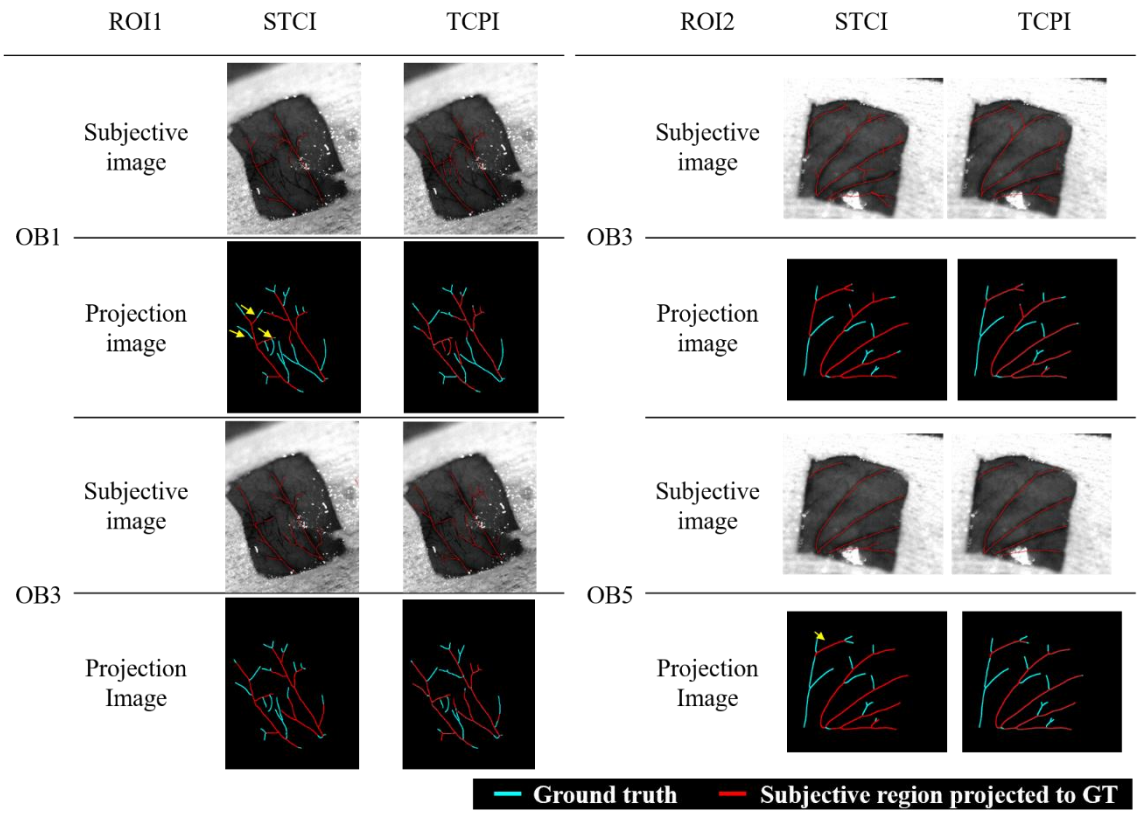

(a)

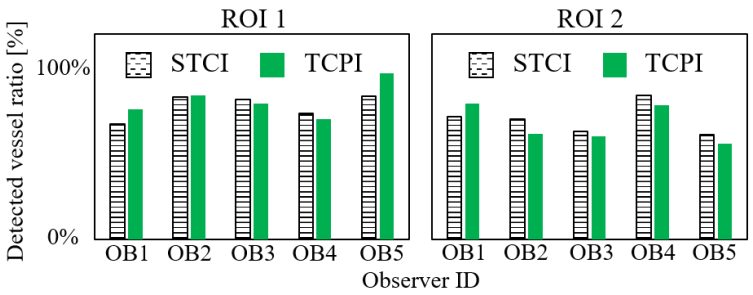

(b)

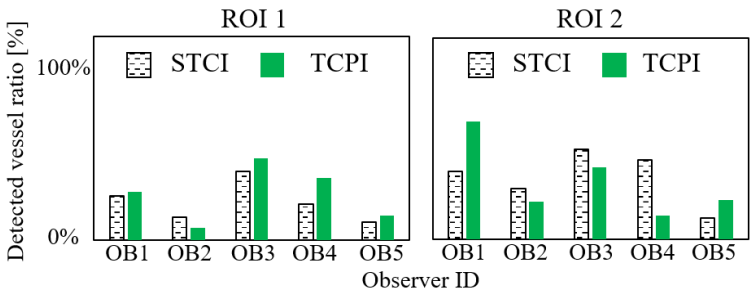

(c)

Figure 5.16: Evaluation experiment results by TCPI for rat 2: (a) Subjective and projection images, (b) detected vessel ratio for whole vessels, and (c)branching vessels.

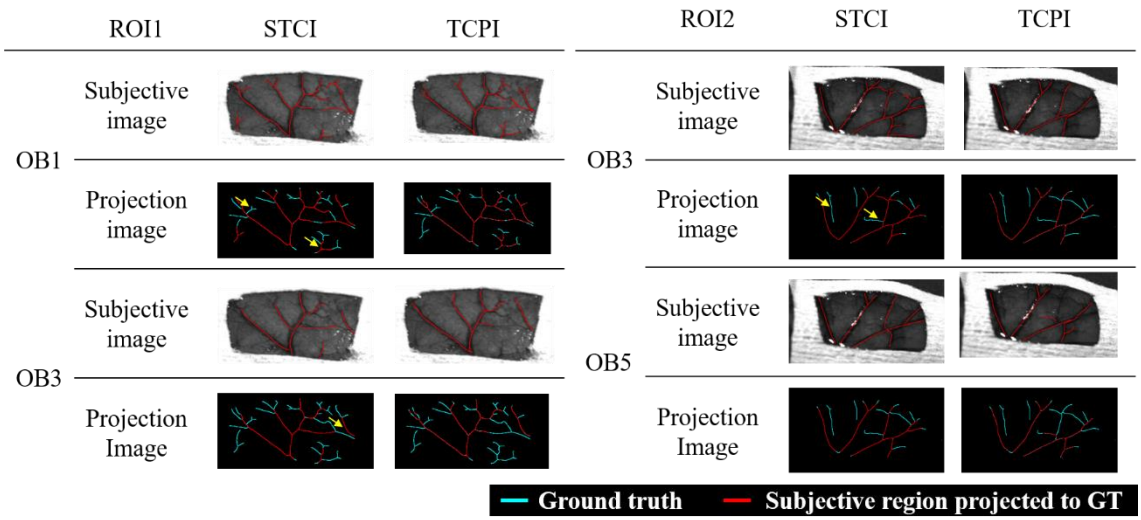

(a)

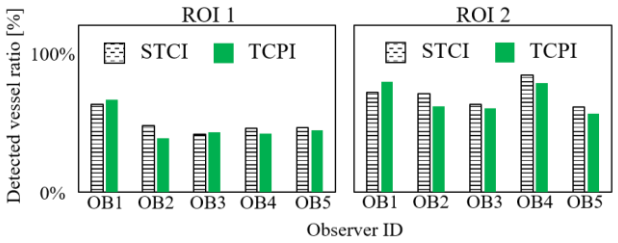

(b)

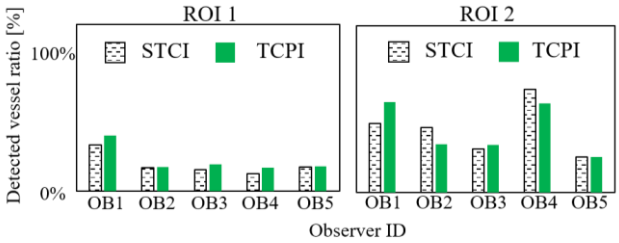

(c)

Figure 5.17: Evaluation experiment results by TCPI for Rat 1: (a) Subjective and projection images, (b) detected vessel ratio for whole vessels, and (c)branching vessels.

The TCPI evaluation, we conducted a paired t-test to whole datasets (30 data) for comprehensive. Figure 5.18 shows boxplot of detected vessel ratios for total vessels and branching vessels. We cannot detect a significant difference between two illuminant conditions ($P = 5.9\times10^{-1}$). It may be caused by the insufficiency of contrast between blood vessels and tissue by adding 630 nm LEDs. Since the intensity of 630 nm LEDs improves the tissue color as similar to that under the conventional illuminant, we can control the degree of blood vessel enhancement and tissue color-preserving by changing

the intensity of 630 nm LEDs. Hence, tissue color-preserving effect and blood vessel enhancement was a trade-off relationship. As assuming the optimal illuminant in surgery, surgeons can control tissue color-preserving and blood vessel enhancement by tuning the intensity of 630 nm LED.

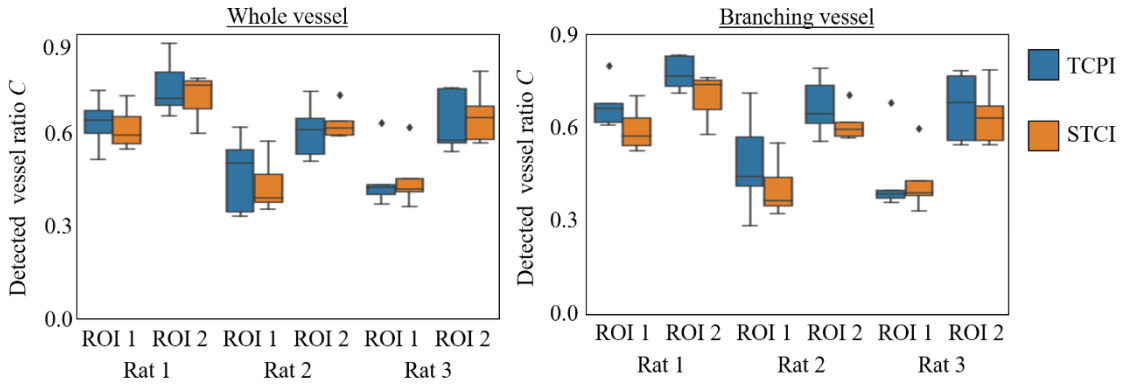

Figure 5.18: Boxplot of detected vessel ratios for total vessels and branching vessels under the TCPI .

Chapter 6 Camera-illuminant combined system for early diagnosis of skin flap necrosis

Chapter 6 describes the system proposed for early diagnosis of skin flap necrosis. We construct the system by combining narrow-band illuminants and a general color camera. We show system overview, and target models for evaluation of the proposed system in Section 6.1. In our system, we designed the optimized illuminant for early diagnosis of the necrosis region. The optimization method is described in Section 6.2. The simulation experiment for the first trial is shown in Section 6.3, and in Section 6.4 practical experiments are conducted. In Section 6.5, we describe evaluation experiments, results, and effectiveness of the proposed system.

6.1 System construction

6.1.1 System overview

In general, a color camera encodes the acquired optical signal by a sensor consisting of three RGB channels. These sensors usually have similar characteristics to human cone cells, whose peak wavelength was 420 nm, 534 nm, and 564 nm. We can capture the reflected light by using these sensors. However, the slight difference between the samples is difficult to capture because of these sensors' dimensional compression of the color information. Hyperspectral cameras have been broadly used these days for capturing detailed information of reflected light. However, the price of these devices is high, and the setup is large, so it hinders the workflow of surgery or bedside monitoring. There are several acquisition methods exist for acquiring spectral images with hyperspectral cameras. A line-scan hyperspectral camera can acquire 3D images by scanning a target object or scanning inside the camera, which adds a wavelength dimension to the plane image. The camera with this mechanism catches spectroscopic images by spectrometer for each line for the plane image. The advantages of this kind of device are its excellent wavelength resolution and the ability to acquire detailed spectral characteristics. The disadvantages are long capturing time, large-scale setup,

and it is difficult to capture image of a moving object. On the other hand, a snapshot hyperspectral camera has sensors which have multiple sensitivities for acquisition of hyperspectral signals. This mechanism is similar to a color camera. Hyperspectral cameras have an optical system that splits reflected lights into light rays in different directions according to wavelength. We use these systems under broad light, such as halogen light and xenon light, to avoid missing wavelength information due to lack of light. The advantage of this device is that we can use it for an object that makes some movement during image capturing. The disadvantages of this device are low wavelength resolution and inaccurate spectral reflectance caused by spectroscopic optical systems. Figure 6.1 shows image capturing system overview of hyperspectral camera and color camera.

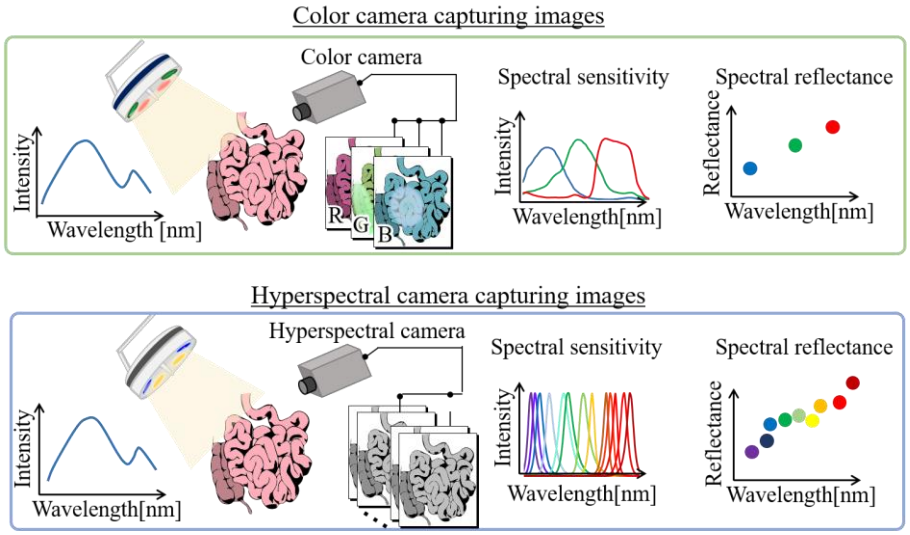

Figure 6.1: Hyperspectral camera and general color camera signal capturing system.

Based on these discussions above, we focus on detailed color information capturing systems constructed by a general color camera and LEDs who has narrow-band spectral characteristics.

Since captured signal are expressed as the product of reflected light, spectral reflectance, and sensor sensitivities, the system combined with RGB sensors and LEDs who has narrow bandwidth can make the high precision of spectral sensitivity compare to the system combined with RGB sensors and broad light. There are some kinds of camera-illuminant combined systems to capture spectral information [39-45]. We investigate the realization of higher dimensionality of spectral data acquisition than color cameras by fast switching of illumination. We designed the spectral distributions

for each target object; hence the critical spectral ranges are changed depending on the target spectral characteristics. Figure 6.2 shows an overview of our system. We aim to construct a system that can acquire high-dimensional spectral information by synchronizing the rapid switching of light sources and color camera shooting timing. Using this system, we can capture some diseases or characteristics in one set of illuminants.

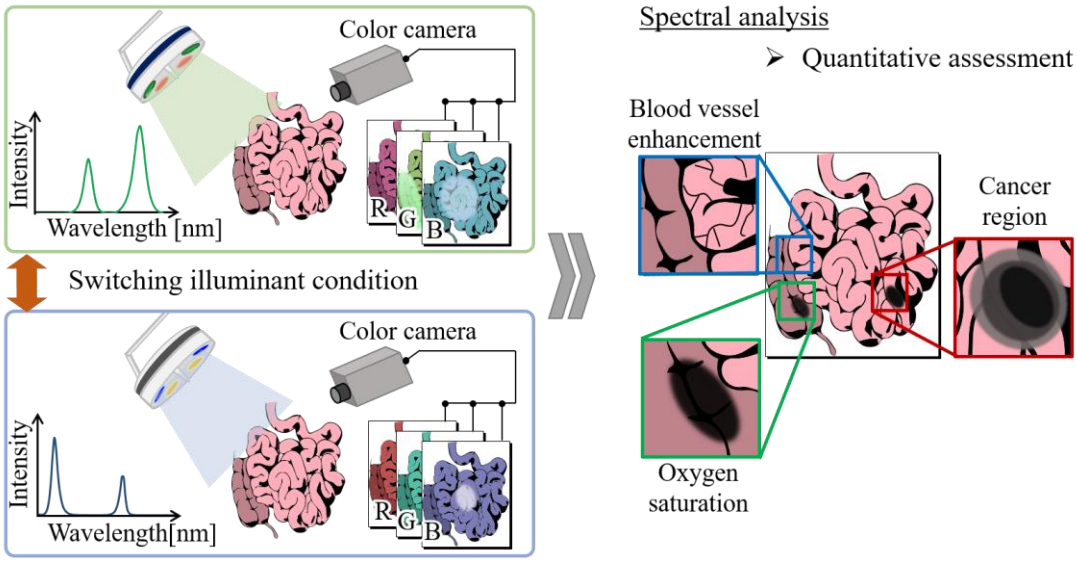

Figure 6.2: Overview of our color information capturing system.

6.1.2 Target of the prototyping system

Skin flaps, which consist of skin, subcutaneous tissue, and deep-tissue region with blood flow, are used to reconstruct areas damaged by disease or trauma. Postoperative skin necrosis may occur due to poor anastomosis or blocking blood vessels. Re-operation for early detection of deteriorated blood flow in the vessels is necessary to avoid skin flap necrosis. Still, it is challenging to monitor blood flow because of the need to observe subtle color changes in skin flap. There are some techniques to observe the skin flap conditions. For example, indocyanine green fluorescence imaging or other contrast enhancement techniques are conducted to confirm the blood flow in the skin flap region [46,47]. However, patients sometimes have allergies to the medicine, or the drug injection is undesirable for the patient, so medical doctors cannot use the medication for confirmation of intraoperative vascularity. In bedside monitoring, the medical staff observes the color of skin flap region. However, it is difficult to observe the color changes because of slight color change in skin flap region and inconsistent color recognition among staff. If the skin flap region has the possibility of necrosis, a pin prick test that is

an invasive method are conducted. There are some other choices such as microcirculation monitoring by using some optical techniques: laser Doppler and plethysmography. However, these methods are sometimes challenging to use because these devices do not show enough work on deep blood vessels. Some researchers detected skin flap conditions by hyperspectral information [42-44] or other signals captured by optical devices [48-56]. However, these methods have difficulty in continuous measurements for bedside monitoring. As mentioned above, we focused on detecting necrosis regions by quantitative evaluation of skin flaps' surface color, which is an easy and non-contact measurement.

For monitoring skin flap regions, spectroscopic measurements are useful for detection of skin flap necrosis. In this study, we focused on the color camera-illuminant combined system described in Section 6.1.1 for early diagnosis of skin flap necrosis. We carried out two-channel-illuminants design for this purpose for early diagnosis of necrosis region by congestion model and ischemia model. First, we simulated the illuminants and evaluated the effect of the illuminants. Evaluation experiments were conducted for evaluation of the effect of the proposed system. Figure 6.3 shows the assumed system for early diagnosis of skin flap necrosis.

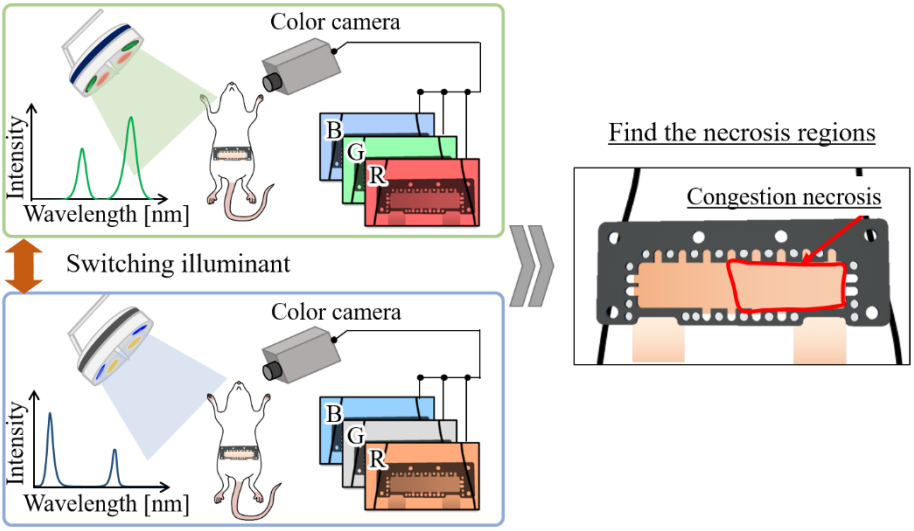

Figure 6.3: System overview for early diagnosis of skin flap necrosis

6.1.3 System construction

To prototype our system, we assumed the uses of a color camera, Grasshopper 3 (FILR Systems Inc.), VC-23C (Baumer Co., Ltd.), and LEDs. For LEDs, we assumed the use of the spectrally tunable light source constructed in previous chapters, with thirteen

different types of LEDs implemented in the second generation of the spectrally tunable light source described in Section 2.4. Figure 6.4 shows two kinds of camera sensitivities for the system. We also used LED distribution spectra shown in Figure 2.1 (b).

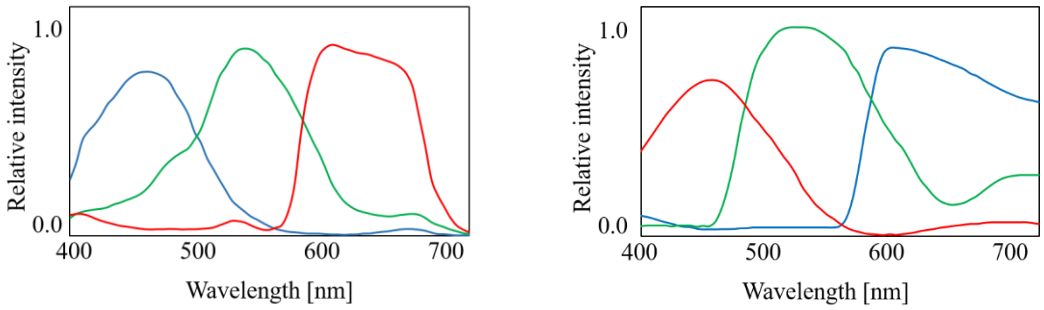

(a) (b)

Figure 6.4: Camera sensitivities for prototyped systems: (a) Grasshopper 3 (FILR Systems Inc.), and (b) VC-23 C (Baumer Co., Ltd).

6.2 Illuminant optimization and signal detection

6.2.1 Optimization method

In this thesis, we designed two kinds of illuminant distributions for camera-illuminant combined system. We used normal region spectral reflectance and necrosis region reflectance for optimization of the illuminant distributions for skin flap necrosis. We defined the optimized illuminant spectrum as the set of illuminant distributions that can maximize separation degree by using Fisher's linear discrimination analysis [57]. As a first step of the optimization, we simulated RGB values by using calculated illuminant distributions, camera sensitivities, and spectral reflectance as follows:

$$\begin{aligned} R_{KI} &= \int r(\lambda)E_I(\lambda)R_K(\lambda)d\lambda \\ G_{KI} &= \int g(\lambda)E_I(\lambda)R_K(\lambda)d\lambda \\ B_{KI} &= \int b(\lambda)E_I(\lambda)R_K(\lambda)d\lambda \end{aligned} \qquad (6\text{-}1)$$

$r(\lambda), g(\lambda), b(\lambda)$ are the sensor sensitivities of a color camera. R_{KI}, G_{KI}, B_{KI} is RGB signals under the

illuminant condition *I* for the target status *K* (normal or necrosis). Using these values, we acquired 6-dimensional vector $\mathbf{x}_{Kt}$:

$$\mathbf{x}_{Kt} = \begin{bmatrix} R_{K1t} \\ \vdots \\ B_{K2t} \end{bmatrix} = \begin{bmatrix} x_{Kt1} \\ \vdots \\ x_{Kt6} \end{bmatrix} \tag{6-2}$$

Here *t* represents the sample order for the optimization. These values are normalized before acquiring subsequent calculations. For calculation of Fisher's linear discrimination, we use class average values whose dimension is six:

$$\mathbf{m}_K = \frac{1}{N}\sum_{t=1}^{N}\mathbf{x}_{Kt} \tag{6-3}$$

Here *N* is the number of samples. We calculate within-class variance and between-class variance for the calculation of separation value. Within-class variance S_W is defined as summarize value of two kinds of within-class variance, s_{no} and s_{ne} :

$$s_K = \sum_{t=1}^{N}\left(\mathbf{x}_{Kt} - \mathbf{m}_K\right)\left(\mathbf{x}_{Kt} - \mathbf{m}_K\right)^T \tag{6-4}$$

Here *T* means transposition of the system matrix. Using projection vector ω, a-dimension-within-class variance $\tilde{S}_W$ is defined as follows:

$$\begin{aligned} \tilde{S}_W &= \sum_{K=no,ne}\sum_{t=1}^{N}\left(\omega^T\mathbf{x}_{Kt} - \omega^T\mathbf{m}_{Kt}\right)\left(\omega^T\mathbf{x}_{Kt} - \omega^T\mathbf{m}_{Kt}\right)^T \\ &= \omega^T S_W \omega \end{aligned} \tag{6-5}$$

For between-class variance, we use the mean values for each group:

$$\begin{aligned} S_B &= N\left(\mathbf{m}_{no} - \mathbf{m}\right)\left(\mathbf{m}_{no} - \mathbf{m}\right)^T + N\left(\mathbf{m}_{ne} - \mathbf{m}\right)\left(\mathbf{m}_{ne} - \mathbf{m}\right)^T \\ &= \frac{N}{2}\left(\mathbf{m}_{no} - \mathbf{m}_{ne}\right)\left(\mathbf{m}_{no} - \mathbf{m}_{ne}\right)^T \end{aligned} \tag{6-6}$$

Using projection vector ω, a-dimension-between-class variance $\tilde{S}_B$ is defined as follows:

$$\begin{aligned}\tilde{S}_B &= \frac{N}{2}\left(\omega^T \mathbf{m}_n - \omega^T \mathbf{m}_i\right)\left(\omega^T \mathbf{m}_n - \omega^T \mathbf{m}_i\right)^T \\ &= \omega^T S_B \omega\end{aligned} \qquad (6\text{-}7)$$

Fisher's linear discrimination value $J(\omega)$ is defined as follows:

$$J(\omega) = \frac{\omega^T S_B \omega}{\omega^T S_W \omega} \qquad (6\text{-}8)$$

Projection value ω *is* calculated by method of Lagrange multiplier as follows:

$$\begin{aligned}\omega &\propto S_W{}^{-1} S_B \omega \\ &\propto S_W{}^{-1}\left(\mathbf{m}_1 - \mathbf{m}_2\right)\end{aligned} \qquad (6\text{-}9)$$

The optimal illuminant was defined as maximizing the Fisher's linear discrimination value $J(\omega)$. The optimization of the illuminant was conducted using particle swarm optimization. If the calculated value was not changed for number of regulations of iterations, we defined the last value as the optimal illuminant. Figure 6.5 shows the optimization flow for the set of illuminant distributions.

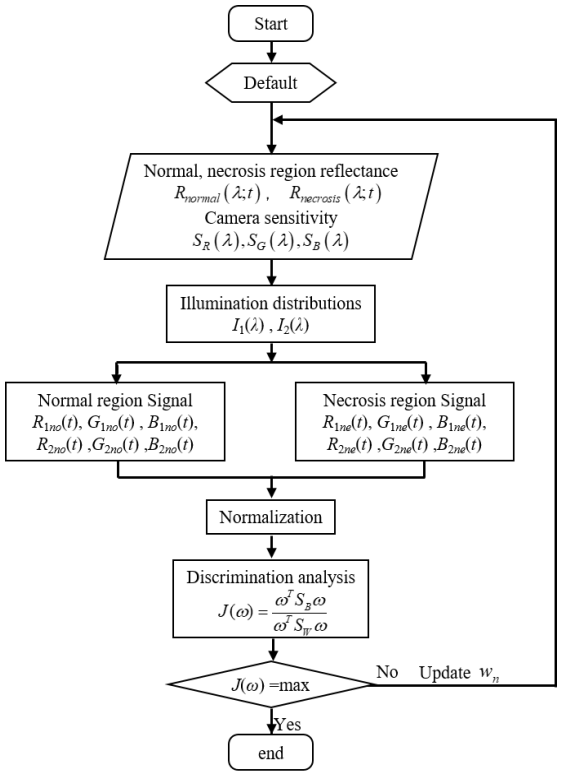

Figure 6.5: Optimization flow for the camera-illuminant combination system.

6.2.2 Detection of the necrosis regions

Our purpose of the system is to detect necrosis in the early stage of poor blood circulation caused by anastomotic failure or vascular obstruction. For detecting the poor circulation region, we constructed a discrimination model using support vector machine (SVM) based on the training data and applying it to the test data. RGB signals under each illuminant distributions simulated by the optimization step were selected as features of the discriminations. We used RBF kernel for the construction of SVM model and testing the models. To evaluate the effectiveness of the system, we compared two image capturing environments, the conventional illuminant spectrum-color camera combination and the two sets of optimized illuminant spectra-color camera combination. Sensitivity, specificity, and accuracy (in equation 6-10) were used for the evaluation of necrosis region detection. The necrosis region was set as positive and the normal region set as negative.

$$\begin{aligned} Sensitivity &= \frac{TP}{TP+FN} \\ Specificity &= \frac{TN}{TN+FP} \\ Accuracy &= \frac{TP+TN}{TP+FP+TN+FN} \end{aligned} \qquad (6\text{-}10)$$

We defined *TP* as true positive, *TN* as true negative, *FP* as false positive, and *FN* as false negative.

We used simulated images calculated from hyperspectral images for the training step. As a first step of capturing training data, hyperspectral images were divided by an illuminant spectrum distribution for calculating spectral reflectance. Hyperspectral images used in this step were corrected uneven lighting caused by variations of illuminant intensity caused by the image capturing environment.

Simulated RGB images were calculated using multiple signals; the optimized illuminant spectra, RGB sensor sensitivities, and spectral reflectance. After simulating the RGB images under the optimized illuminant spectral distributions, two sets of RGB signals were used for training a discrimination model by SVM. To reduce individual differences, normalization was conducted before constructing the discrimination model. For the testing step, simulation images calculated as same as the training step were used for a simulative evaluation experiment. An evaluation experiment, captured images by a color camera, and the spectrally tunable light source: second generation were used as the testing dataset. White plate images under each illuminant were

captured for controlling the color balance of captured images.

We set the target images to detect the early stage of skin flap necrosis as few hours after the superficial epigastric vessel ligation. Necrosis regions were defined by manually selection region using captured images three days after ligation for congestion or ischemia samples construction.

6.3 Simulation design: proposed model validation

6.3.1 Spectral reflectance of skin flap

We captured images every 3 hours until one day after ligation of the left superficial epigastric artery. Measurements were taken every 6 hours until the end of the second day and every 12 hours until the third day. For the first trial for the proposed system, we used one ischemia model for the trial experiment. We used a hyperspectral image captured three-hour-after ligation image as the early stage of necrosis. The necrosis region was registered manually by using the image captured after 72 hours of ligation. Figure 6.6 shows captured images after three hours and seventy-two hours after ligation images and manually selected necrosis region.

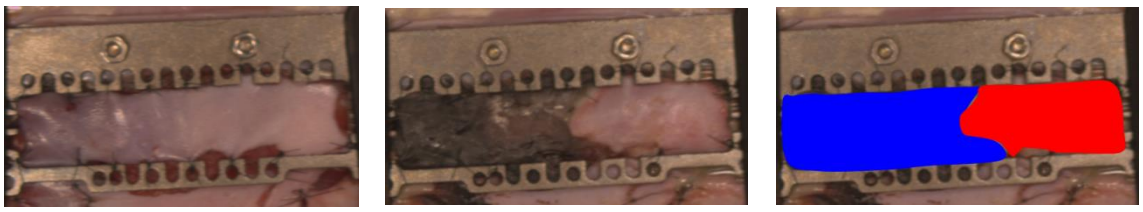

(a) (b) (c)

Figure 6.6: Captured images constructed from hyperspectral images: (a) Three hours after ligation, (b) seventy-two hours after ligation, and (c) manually selected necrosis and normal region, red: Normal region, and blue: Necrosis region.

Figure 6.7 shows spectral reflectance of normal region $R_{no}(\lambda)$ and necrosis region $R_{ne}(\lambda)$. $R_{no}(\lambda)$ has higher reflectance compare to $R_{ne}(\lambda)$. The shape of spectral reflectance around 550 nm are similar characteristics in absorption coefficient HbO_2. Ischemic region was not provided high oxygen saturation compared to normal region caused by ligation of artery. These tendencies thought to be caused by contained blood oxygen saturations.

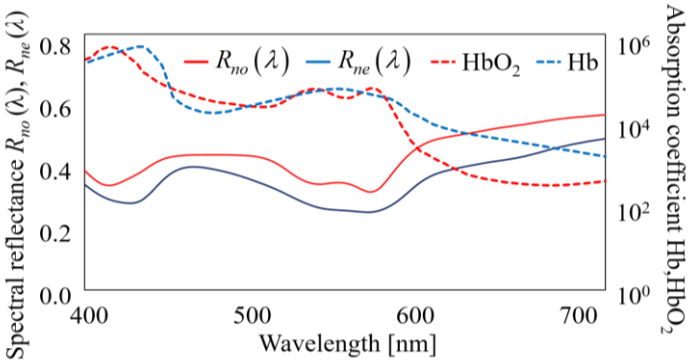

Figure 6.7: Averaged spectral reflectance of normal region and necrosis region.

6.3.2 Illuminant design for first generation

We optimized system illuminant spectral distributions for the proposed system by using simulated RGB images. The simulated images were calculated using multiple signals; RGB sensor sensitivities (Grasshopper3, FILR Systems Inc., Figure 6.4 (a)), and spectral reflectance of normal and necrosis region. The calculated illuminant spectra were simulated by combining LED illuminant distributions (Figure 2.1). We used 100 points of spectral reflectance for each region, normal and necrosis. For normalization of test data, the simulated RGB signals were compressed to the six-dimensional unit vector to uniform the illuminant unevenness.

Figure 6.8 shows optimized illuminant spectra for the proposed system. Illuminant 1 has three peaks that match the RGB sensor's sensitivities. Illuminant 2 has two peaks, and these peaks are different from the three peaks in illuminant 1. Since five peaks are matched with large spectral reflectance, the illuminant spectra were thought to be enough for the proposed system.

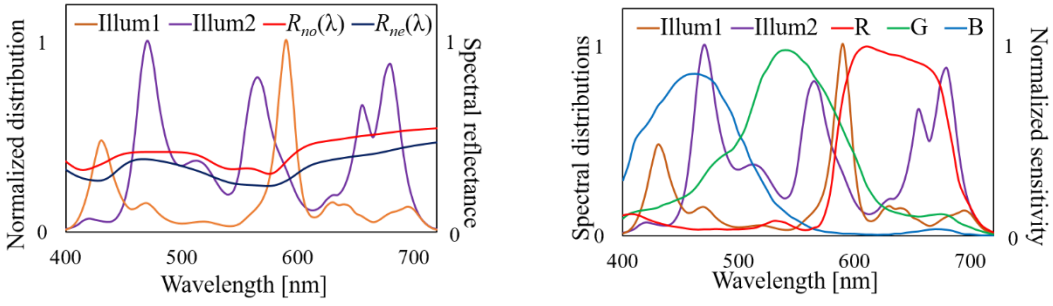

(a) (b)

Figure 6.8: Spectral distributions for the proposed system: (a) system illuminant spectra with spectral reflectance of $R_{ne}(\lambda)$ and $R_{no}(\lambda)$, and (b) system illuminant spectra with RGB camera sensitivities.

6.3.3 Simulation of the optimal illuminant: Pre-experiment

For evaluation of the proposed system, we detected the necrosis region by using two illuminant conditions, illuminant 1 (Figure 6.9 (b)) and illuminant 2 (Figure 6.9 (c)) for creating six-dimensional vectors for evaluating the status of the skin flap region. We used the image that the illuminant condition was the conventional illuminant for comparison. Three kinds of images, under the conventional illuminant, the illuminant 1, and the illuminant 2 were simulated by using hyperspectral images. Figure 6.9 shows simulated images using the hyperspectral image captured three hours after the left superficial epigastric artery ligation. Before input the RGB signals to SVM, we conducted normalization by compression the vector to unit vector as same as the discrimination model construction step. Figure 6.10 shows discrimination results by the conventional illuminant and the proposed system. Under the conventional illuminant, it was challenging to detect correct necrosis regions shown as wide false-negative regions compared to those under the proposed system. This tendency shows that the proposed system can detect slight color changes caused by less supply of arterial blood caused by the superficial artery's ligation. In contrast, the detection results using two illuminant conditions for the proposed system show less false-negative regions than those under the conventional illuminant.

Table 6.1 shows sensitivity, specificity, and accuracy for the conventional illuminant and the proposed system. Since these values by the proposed system were superior to that by the conventional illuminant, we confirmed the proposed system's effect for the detection of skin flap necrosis regions.

(a) (b) (c)

Figure 6.9: Simulated images 3 hours after ligation: (a) Under the conventional illuminant, (b) under the illuminant 1, and (c) under the illuminant 2.

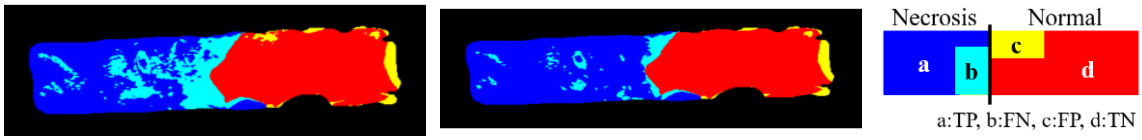

(a) (b) (c)

Figure 6.10: Detected necrosis regions: (a) Detected regions by using the conventional illuminant, (b) detected necrosis region by using the proposed system, and (c) area division of detected results.

Table 6.1: Sensitivity, specificity, and accuracy for the proposal trial experiment.

	Sensitivity[%]	Specificity[%]	Accuracy[%]
Conventional illuminant	69.2	92.0	91.0
Proposed system	89.3	93.9	94.5

6.4 Simulation design: Second generation

6.4.1 Spectral reflectance of skin flap

We optimized illuminant spectra for ischemia status and congestion status that was constructed by using the skin flap chamber: second generation. The illuminant spectra for the proposed system were optimized separately for the ischemia model and congestion model. Figure 6.11 shows averaged spectral reflectance and relative spectral reflectance normal region $R_{no}(\lambda)$ and necrosis region $R_{ne}(\lambda)$. Two rat samples for each ischemic or congestion status were used to calculate these spectral reflectance. Relative spectral reflectance was calculated by dividing spectral reflectance as isosbestic point, 525 nm, to evaluate the oxygen saturation difference between normal and necrosis regions. In the ischemia model, $R_{no}(\lambda)$ has higher reflectance compare to $R_{ne}(\lambda)$. The shape of spectral reflectance $R_{ne}(\lambda)$ around 550 nm are similar characteristics in absorption coefficient HbO_2. In addition, these tendency is as same as that in relative spectral reflectance. The difference in the normal status and necrosis status in the ischemia model was thought to be caused by tissue oxygen saturation.

In the congestion model, $R_{no}(\lambda)$ has higher reflectance compare to $R_{ne}(\lambda)$. The shape of spectral reflectance $R_{ne}(\lambda)$ around 550 nm are similar characteristics in the absorption coefficient HbO_2. Although, the same shape was observed in $R_{ne}(\lambda)$. For relative spectral reflectance, there were the same characteristics as that in ischemia status, but the difference between the two regions was slight compared to that in ischemia. Moreover, spectral reflectance $R_{no}(\lambda)$ in the congestion model was lower

tendency compared to that in ischemia status. Contained blood volumes that induce declining spectral reflectance by absorbing Hb and HbO_2 in a skin flap region may cause these characteristics. In the congestion model, the vein was blocked, but arterial blood was kept in supply. These phenomena induced blood volume enlarging and oxygen saturation's less dropping.

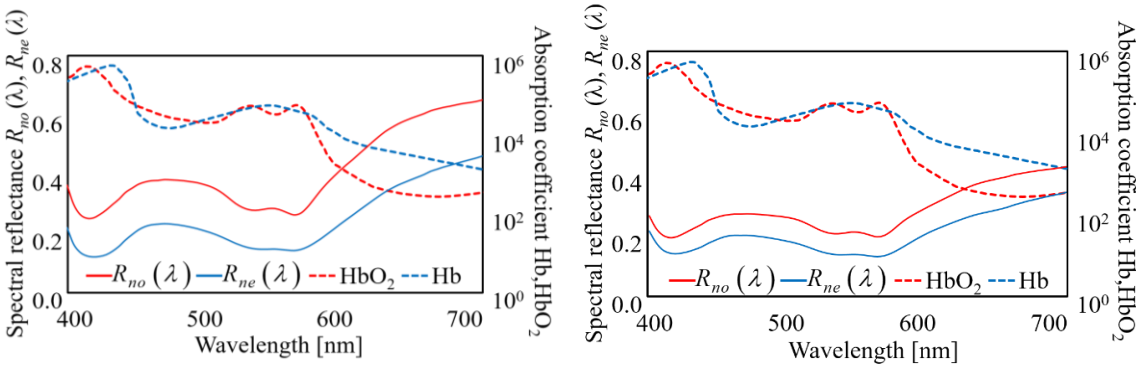

Figure 6.11: Spectral reflectance and relative spectral reflectance of ischemia model and congestion model: (a) Spectral reflectance of ischemia model, and (b) Spectral reflectance of congestion model.

6.4.2 Illuminant design for second generation

We optimized system illuminant spectral distributions for the proposed system by using simulated RGB images. The simulated images were calculated using multiple signals; RGB sensor sensitivities (VC-23 C, Baumer Co., Ltd), Figure 6.4 (a), and spectral reflectance of normal and necrosis region, the calculated illuminant spectra by combining LED illuminant distributions (Figure 2.1).

We used two samples, ischemia model and congestion model, for simulation of the system. One-hundred points of spectral reflectance from each region, normal, and necrosis were selected from captured images randomly for optimization of the illuminant spectra.

For ischemia status, simulated illuminant spectra have peaks in the long-wavelength range (peak wavelength: 630 nm, 645 nm, and 595 nm) and mid-wavelength region (peak wavelength: 565 nm). Spectrum peaks in the long-wavelength range matches to spectral differences between normal and ischemic status. Spectrum peaks in the mid-wavelength range match the spectral reflectance shape difference between normal and ischemic status. Since the difference between the two areas, the normal and the ischemia status, were occurred by oxygen saturation level, the long-wavelength region

that characteristics were shown in Chapter 4 matched with the illuminant peaks. The short-wavelength region characteristics were induced by low-scattering factors and a high ratio of the signal difference.

For congestion status, simulated illuminant spectra have peaks in the short-to-middle range (peak wavelength: 450 nm, 470 nm, 525 nm, and 595 nm). The short-wavelength range matches the spectral reflectance difference between two regions, and the mid-wavelength range matches the spectral reflectance shape difference between normal and ischemic status. The difference between the two regions was induced by blood volume in skin flap regions and low oxygen saturation and blood volume enlargement by less releasing low oxygen saturation blood. Since the oxygen saturation level difference was enhanced by the short and long wavelength-range (shown in ischemic status), these peaks were selected to detect oxygen saturation level for the tissue. Moreover, blood volume differences were enhanced in the middle-wavelength range (shown in Chapter 5). Therefore, it is thought that the mid-wavelength region peaks can detect the difference in blood volume. Figure 6.12 to 6.14 show optimized spectra and system sensitivity for the ischemia model and congestion model.

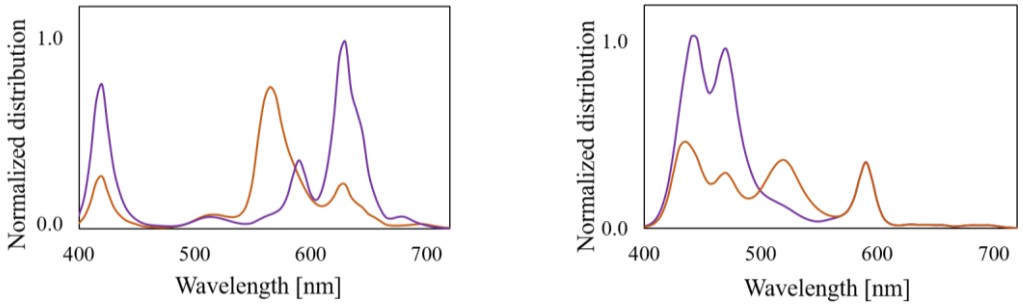

(a) (b)

Figure 6.12: Spectral distributions for the proposed system. (a) System illuminant spectra for ischemia status, and (b) system illuminant spectra for congestion status.

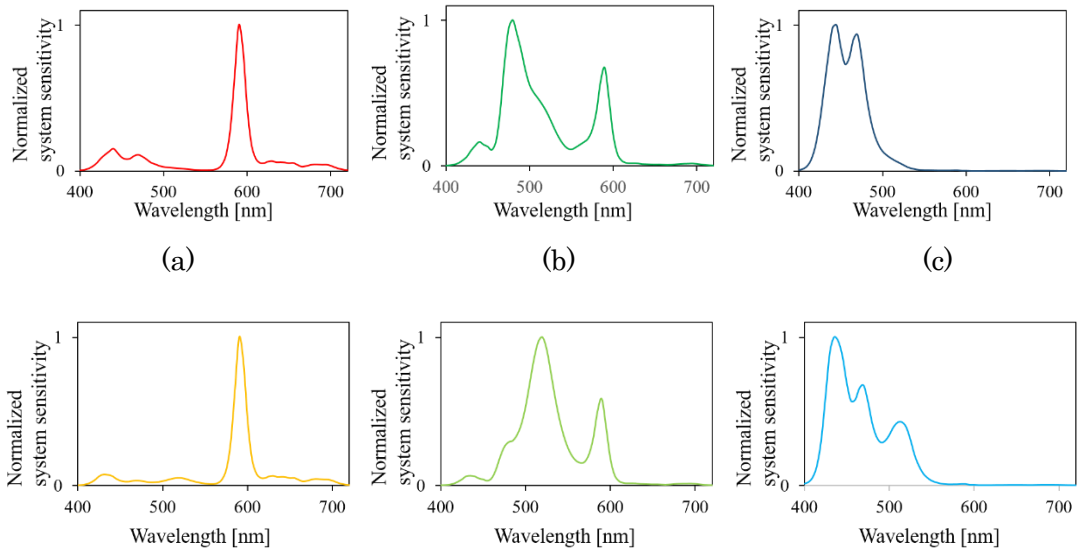

Figure 6.13: System sensitivities for ischemia status: (a) Combined with illuminant 1 and R, (b) combined with illuminant 1 and G, (c) combined with illuminant 1 and B, (d) combined with illuminant 2 and R, (e) combined with illuminant 2 and G, and (f) combined with illuminant 2 and B.

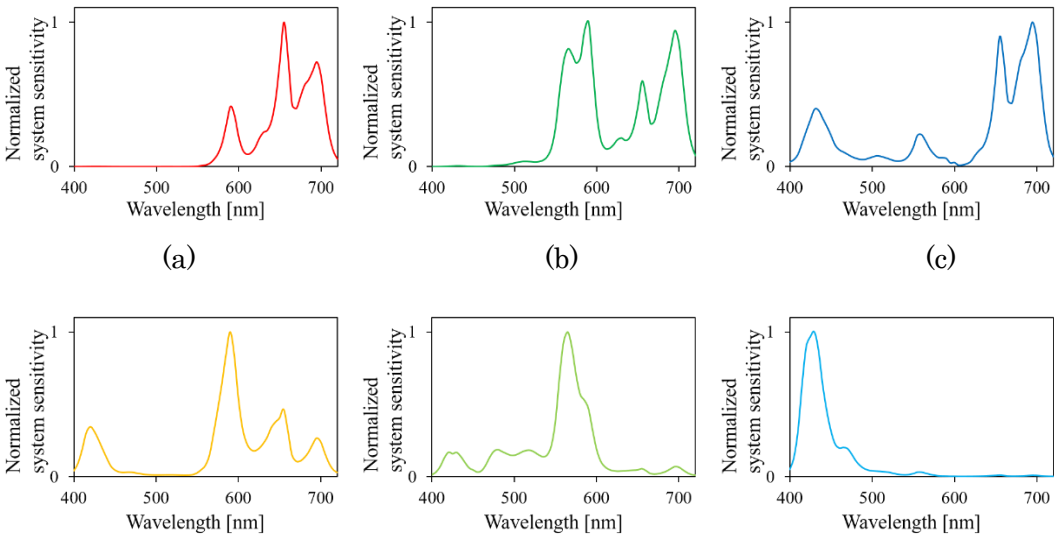

Figure 6.14: System sensitivities for congestion status: (a) Combined with illuminant 1 and R, (b) combined with illuminant 1 and G, (c) combined with illuminant 1 and B, (d) Combined with illuminant 2 and R, (e) combined with illuminant 2 and G, (f) Combined with illuminant 2 and B.

6.4.3 Simulation evaluation for the proposed system

For evaluation of the simulated illuminant spectra, we detected the necrosis region by using two kinds of simulated illuminants. The images under the optimized illuminant spectra and the conventional illuminant were simulated by using hyperspectral images. For learning dataset, two samples were used for each model, ischemia and congestion. For testing dataset, two samples were used for each model. After-two-hour-ligation images were used for this experiment. The SVM model construction environment was the same as Section 6.4. Six dimensional difference values, normal region average and target region signals, were used for evaluation index. The averaged values for normal region were calculated from the edge of normal status regions. Target region signals were divided by normal region averaged value for normalization of signals. Ground truth for necrosis regions were prepared manually by using after 72 hours after ligation images.

Figure 6.15 shows simulation results for the ischemia model. Under the conventional illuminant, FN region were observed wider compared to the proposed system. These results shows that the proposed system can detect necrosis region more accurate compared to the conventional illuminant. Table 6.2 shows evaluation values for the ischemia model.

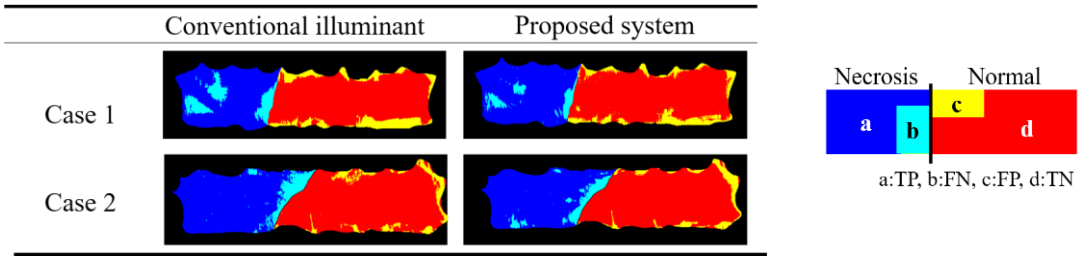

Figure 6.15: Detected necrosis regions for ischemia model.

Table 6.2: Sensitivity, specificity, and accuracy for the simulation experiment: Ischemia model.

	Sensitivity [%]		Specificity [%]		Accuracy[%]	
	Case 1	Case 2	Case 1	Case 2	Case 1	Case 2
Conventional illuminant	84.0	80.9	82.6	83.2	83.1	82.3
Proposed system	89.6	87.6	85.2	90.7	86.9	89.4

In the congestion model, wider FN regions were observed under the conventional illuminant compared to the proposed system. TP region shows more accurate extraction under the proposed system compares to that under the conventional illuminant. These results shows that the proposed system can detect necrosis region almost completely. Figure 6.17 shows the simulation results for the congestion model and Table 6.3 shows evaluation values for the congestion model.

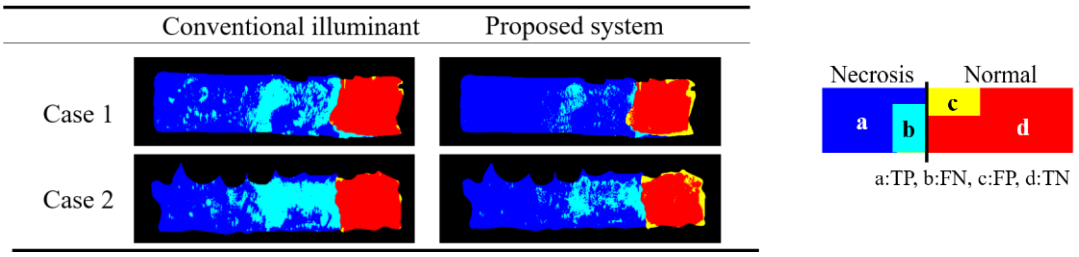

Figure 6.16: Detected necrosis regions for congestion model.

Table 6.3: Sensitivity, specificity, and accuracy for the simulation experiment: congestion model.

	Sensitivity [%]		Specificity [%]		Accuracy[%]	
	Case 1	Case 2	Case 1	Case 2	Case 1	Case 2
Conventional illuminant	71.5	62.8	81.2	85.2	87.7	87.0
Proposed system	89.9	87.6	98.3	98.4	99.2	99.0

6.5 Evaluation experiment

6.5.1 Experimental environment

We conducted an evaluation experiment for the proposed system using the spectrally tunable light source: second generation and a color camera (VC-23 C, Baumer Co., Ltd). The illuminant conditions were manually controlled for changing some kinds of illuminants that was optimized by simulation shown in Section 6.4. Target region were set 40 cm apart from the camera-illuminant combined system. The polarizers were placed in a cross Nicol arrangement on the camera side and light source side to block the specular reflection light. Figure 6.17 shows image capturing environment for the evaluation experiments.

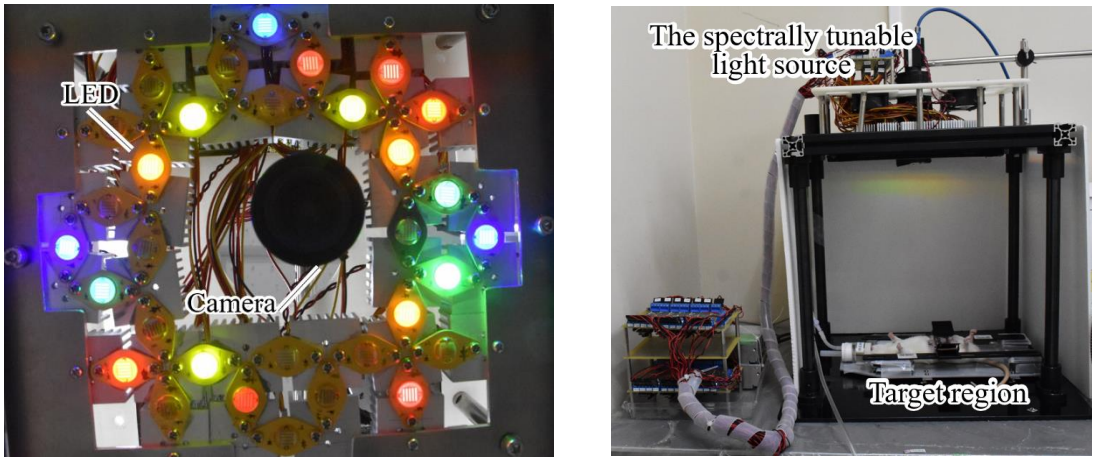

(a) (b)

Figure 6.17: Experimental environment for the evaluation experiment: (a) The spectrally tunable light source and color camera combined system, and (b) The setting of target region and the proposed system.

We prepared two rats for the congestion model and two rats for the ischemia model. For each model, images were captured under the conventional illuminant, illuminant 1 for congestion model or ischemia model, and illuminant 2 for ischemia model or congestion model. Figure 6.18 shows the samples of captured images of congestion model and ischemia model. Captured images were converted to adjust color balances for making same image capturing environment as the simulation after capturing images.

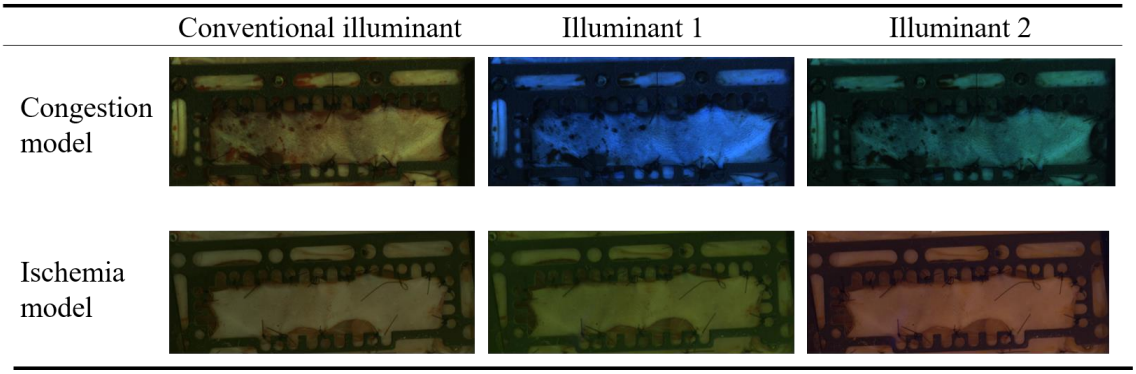

Figure 6.18: Captured images under the conventional illuminant and two kinds of optimized illuminants.

6.5.2 Discrimination model construction

We conducted a practical validation of the proposed system using different data for discrimination model construction and validation data. For the discrimination model

construction, we used four image sets for each target model. These images were the same images used in the optimization step and simulation evaluation step (shown in 6.4.3) for the proposed system's illuminant distributions. Whole points for the normal region and necrosis region were used for SVM model construction. Six dimensional difference values, normal region average and target region signals, were used for evaluation index. The normal region average values were calculated from the edge of normal status regions. Ground truth for necrosis regions were prepared manually by using after 72 hours after ligation images. The RGB signals for each illuminant condition in the two-hour-after ligation image.

Figure 6.19 shows detected necrosis regions in congestion status. Under the conventional illuminant, wider FN regions were observed than that under the proposed system. TP region shows more accurate extraction under the proposed system compares to that under the conventional illuminant. Table 6.4 shows the evaluation values for the congestion model.

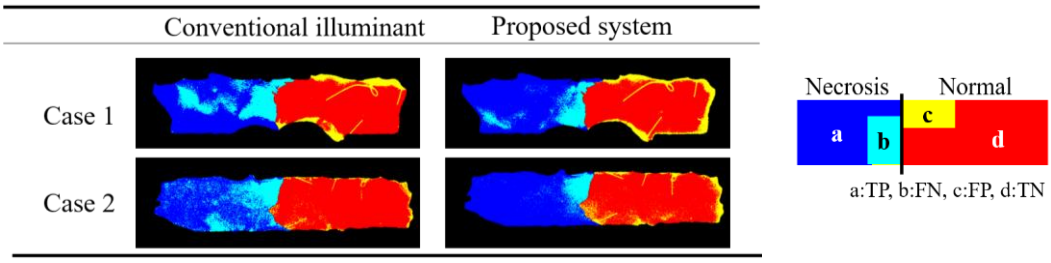

Figure 6.19: Detected necrosis regions for congestion model: discrimination model construction by four samples of simulation images.

Table 6.2: Sensitivity, specificity, and accuracy for the congestion model: discrimination model construction: discrimination model construction by three samples of simulation images.

	Sensitivity [%]		Specificity [%]		Accuracy[%]	
	Case 1	Case 2	Case 1	Case 2	Case 1	Case 2
Conventional illuminant	67.7	63.0	85.6	94.2	77.1	79.4
Proposed system	79.8	87.4	82.5	87.3	81.2	87.4

Figure 6.20 shows detected necrosis regions in ischemia status. For each result, TP region shows high accurate. However, wider FN regions were also observed under the

conventional illuminant than that under the proposed system. These results shows that the proposed system can detect necrosis region better than that under the conventional illuminant. Table 6.5 shows the evaluation values for the congestion model.

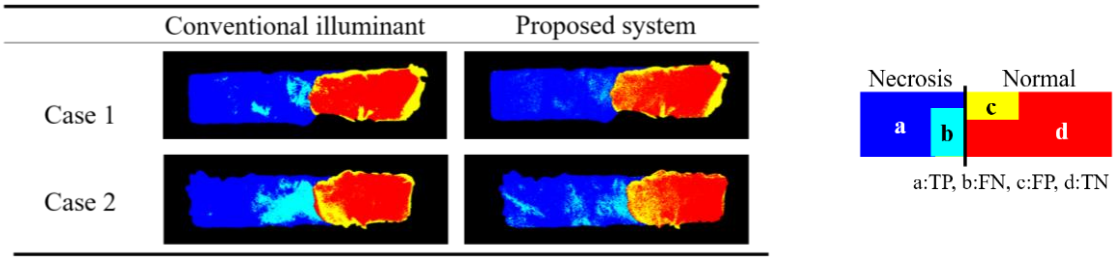

Figure 6.20: Detected necrosis regions for ischemia model: discrimination model construction by four samples of simulation images.

Table 6.5: Sensitivity, specificity, and accuracy for the ischemia model: discrimination model construction: discrimination model construction by three samples of simulation images.

	Sensitivity [%]		Specificity [%]		Accuracy[%]	
	Case 1	Case 2	Case 1	Case 2	Case 1	Case 2
Conventional illuminant	91.2	74.1	76.0	75.2	82.3	74.5
Proposed system	94.6	82.1	73.0	73.1	84.8	78.3

Through two results, the proposal system thought to detect necrosis region earlier compared to that under the conventional illuminant from these results above.

Chapter 7 Conclusions

This study proposes the method for surgical illuminant spectrum optimization and conducts evaluation experiments by using the spectrally tunable light source. In Section 7.1, we summarize the proposed method and experimental environment for evaluating the proposed system. The target for the optimization for the evaluation of the proposed system is shown in Section 7.2. We optimize illuminant spectra for blood circulation conditions as a first step of the evaluation. Quantitative evaluation is conducted by measuring the color difference between poor circulation regions and the normal circulation regions is shown in Section 7.3. We conduct a detailed subjective evaluation for the optimal illuminant that enhances blood vessel structures, as summarize in Section 7.4. An additional study of the camera-illuminant combined system and that verification system is outlined in Section 7.5. At the end of this chapter, we show the future work and issues of our proposed method.

7.1 Proposed method for optimization of the surgical illuminant

We have proposed a surgical illuminant optimization method by spectrally designed illuminant spectra for enhancing color information. In the simulation design of spectral distributions, we aimed to ensure that the surgeons' diagnostic environment does not change significantly by constraining the whiteness of the illuminant color. As a first step of the verification, we constructed the spectrally tunable light source for clarifying the effect of spectrally designed illuminants. The device consists of a combination of LEDs with multiple narrow-band spectral characteristics. We designed the illuminant spectral distributions by combining these LED spectral distributions. For the optimization of the illuminants, we set intensities for each LED. We applied this method to several subjects by changing the evaluation index for each target.

7.2 Target model construction

We used three kinds of target samples to validate the effect of the optimization method on surgical illuminant distribution. The first sample was organ blood circulation using a poor blood circulation model of a rat cecum by blocking the blood flow to mimic low perfusion conditions. As further validation, we also included vascular structures, which are essential for diagnosing disease and the advancement of procedures. These target regions' spectral characteristics were captured to optimize the surgical illuminant for illuminant spectra design. For a detailed evaluation of the optimal illuminant for an oxygen saturation level, we used the cattle blood sample to measure the oxygen saturation level before the evaluation experiment by an analysis apparatus of blood gas.

We prepared a model of skin flap necrosis to evaluate the optimal illuminant and proposed system for practical validation. We designed a skin flap chamber for stable hyperspectral measurements.

7.3 Optimization for the blood circulation

We have designed spectral distributions for the enhancement of blood oxygen saturation level. We used color difference based on CIECAM02 as an index of the simulation design and quantitative evaluation for the optimal illuminant. We conducted simulation and evaluation experiments using rat cecum, cattle blood sample, and skin flap model.

First, we conducted an evaluation experiment using rat cecum that mimics the poor circulation region by blocking the blood flow. We designed spectral distribution to emphasize blood circulation conditions that maintain illuminant color whiteness by combining LED spectra. The spectral reflectance between poor circulation and normal circulation region had quite a difference in longer than 600 nm regions caused by the absorption difference between Hb and HbO_2. We simulated optimized illuminant spectra by controlling three kinds of illuminant whiteness levels. The peaks of the simulated illuminant spectra had matched the difference between the two regions. The evaluation experiment was conducted using a spectrally tunable light source to reproduce the optimized illuminant spectrum and the conventional illuminant spectra. The effect of the optimized illuminant spectrum was confirmed by color difference

enlargement between two regions.

As a second step in validating the optimization method, we conducted subjective evaluation by using the cattle blood sample to control the experimental environment for already known oxygen saturation samples. We used two kinds of blood samples, enclosed in a glass cell, and covered with tissue to simulate organ color changed due to oxygen saturation. The spectral reflectance had a massive difference between high and low oxygen saturation levels in more than 600 nm range, and these characteristics were similar to that in rat cecum. The two kinds of optimized illuminant spectra had similar characteristics to that in rat cecum. We conducted a subjective evaluation by comparing several kinds of samples and confirmed the optimal illuminants' effect.

At last, we conducted the same experiment by using a skin flap to detect necrosis regions in the early stage. Simulation experiments were conducted by using hyperspectral images in the same experimental environment. The color difference between the normal region and the final area of necrosis was enlarged using the optimized illuminant spectrum. We confirmed the applicability of the optimization method to an actual disease.

7.4 Optimization for the blood vessel structure

To realize a more detailed subjective evaluation experiment and verify the effect of the narrow-band illuminant, an illuminant was designed and evaluated to clarify the organ surface layer's vascular structure. We used color difference as an index for the whiteness level of the illuminant, and the contrast value was used as the enhancement degree of the blood vessel structure. For calculation of contrast value, we used lightness value from CIECAM02. The tissue region's spectral reflectance and blood vessel region showed a difference in 400 to 600 nm region and the same tendency in 600 to 720 nm region. We simulated the optimal illuminant for the enhancement of blood vessel structures as a first step. Since the tissue color was changed under the simulated illuminant caused by illuminant characteristics, we selected one LED for controlling tissue color preservation. We conducted a subjective evaluation for the optimal illuminant and added 630 nm LED for tissue-color preservation. For the evaluation experiment, observers viewed rat cecum under three kinds of the illuminant. They evaluated the blood vessel structure by drawing lines on the image taken under the 505

nm LED that enhanced the blood vessel region. The evaluation index was calculated by the projection of the drawn line to the ground truth. The subjective evaluation was conducted by using three rat samples, five observers each. The effect was confirmed under the optimal illuminant by a statistically significant difference between two illuminants, the conventional illuminant, and the optimized illuminant. On the other hand, the illuminant that added 630 nm LED to the optimal illuminant confirmed that the tissue color was preserved. However, few differences were observed for the enhancement of blood structures.

7.5 Camera-illuminant combined system

As a developmental validation, we proposed a camera-illuminant combined system that contained narrowband illuminants and a color camera for capturing detailed color information in a few snap. In this study, the illuminant distribution design and evaluation experiments were carried out, assuming a system capable of acquiring 6 band images by switching two kinds of the designed illuminant. We set a target as early diagnosis of skin flap necrosis. We captured spectral reflectance images and calculated system illuminants by simulation. For the optimization of the illuminants, we used a separation degree between the normal region and necrosis region for evaluating the effect of the system illuminants. We calculated two kinds of system illuminants, for congestion and ischemia, and evaluated the effect by simulation and evaluation experiment using the spectrally tunable light source and a color camera. Since our purpose was to detect necrosis in the early stage of blood vessel obstruction or anastomosis failure, we used two-hour after ligation images for illuminant design and evaluation experiments. The necrosis regions were selected manually by using 72-hour after ligation images.

As a first step for optimizing the system illuminant spectra and evaluation experiments, we conducted these steps by using one image set. A limited number of spectral reflectance were used to optimize illuminant, and the necrosis region was detected using SVM. The evaluation values, sensitivity, specificity, and accuracy were exceeded under the proposed system compared to that under the conventional illuminant and color camera.

As a next step of the evaluation, we designed illuminant and constructed SVM discrimination model using a pre-acquired data set by simulation analysis. The effect of proposed system for detection of necrosis region caused by ischemia or congestion status

was confirmed by simulation using hyperspectral images. As the system evaluation, the target region images were captured under the system illuminants, and the conventional illuminant reproduced by the spectrally tunable light source. The index values under the proposed system were exceeded than that under the conventional illuminant. These results suggested the effectiveness of the system.

7.6 Future issues

We proposed the method for surgical illuminant spectrum optimization and conducted evaluation experiments. However, there are several issues with the proposed method and its evaluation experiments. Those issues are listed below:
For the optimization of the surgical illuminant for visual diagnosis:

- The illuminant intensities of the spectrally tunable light source were not enough for medical use
- Observers for the subjective evaluation were not medical-worker
- The optimized illuminant spectra changes with the target objects

For the camera-illuminant combined system:

- Dealing with the progression of necrosis and difference in skin color of the subject is not enough by our system.
- We have to update necrosis region detection method.
- Detection of the difference between ischemia or congestion model.
- Combined light source and camera system have not constructed yet.
- Blood vessel construction in analysis of skin flap region has potential to evaluate the necrosis level.

Since we used the prototype of the spectrally tunable light source, the illuminant

intensity was not enough for surgical procedures. More relevant validation experiments must be conducted for evaluation using a light source with similar luminance levels to the actual surgical illuminants. However, specific effects were confirmed in the subjective evaluation conducted in this study. However, since the subjects who participated in this experiment were not medical-workers, it would be necessary to conduct the same evaluation experiment by surgeons to validate the optimal illuminants' effect.

In this research, we performed evaluation experiments using rat ceca. However, the optimal illuminant spectra may vary depending on the organ's difference and the target region we want to enhance. Besides, in human subjects, some phenomena such as individual differences in the color of organs and the amount of fat are expected to occur, which were not induced in the present study. Nevertheless, since the absorption coefficient of Hb and HbO_2 cause changes in blood circulation and vascular structure, it is possible to achieve a particular effect even in the presence of organ change or personalized difference.

For the camera-illuminant combined system, we confirmed the effect of detecting the necrosis region by using 2-hour after ligation image using our proposed system. However, this effect was limited because of the variation of necrosis progression. Since we used two images set for optimizing the illuminant spectra for the proposed system and discrimination model construction, the limited effect of our proposed system may be caused by less variation of datasets.

For more stable detection of necrosis region, data expansion for the design of the illuminant spectra and construction of the discrimination model are considered significant. Furthermore, it may be useful to establish a system to distinguish between arterial and venous necrosis for clinical use.

Since we constructed the system based on the proposed spectrally tunable light source, it is expected that the accuracy of the system will be improved by introducing the near-infrared region and design the illuminant spectrum in the same way as the present method for a more effective system.

Using the skin flap chamber, we can capture blood vessel structures on the backside of skin flap region. There are some researches, which captured and analyzed blood vessel structures [58-65]. We will conduct blood vessel structure analysis as a future work.

References

[1] Calin, M. A., Parasca, S. V., Savastru, D., and Manea, D, “Hyperspectral imaging in the medical field: present and future.”, Applied Spectroscopy Reviews, 49(6), 435-447, 2014.

[2] Lu, Guolan, and Baowei Fei., “Medical hyperspectral imaging: a review.”, Journal of biomedical optics 19.1: 010901, 2014.

[3] Zuzak, K. J., Francis, R. P., Wehner, E. F., Litorja, M., Cadeddu, J. A., and Livingston, E. H., “Active DLP hyperspectral illumination: a noninvasive, in vivo, system characterization visualizing tissue oxygenation at near video rates.”, Analytical chemistry, 83(19), 7424-7430, 2011.

[4] Zuzak, K. J., Schaeberle, M. D., Lewis, E. N., and Levin, I. W., “Visible reflectance hyperspectral imaging: characterization of a noninvasive, in vivo system for determining tissue perfusion.”, Analytical chemistry, 74(9), 2021-2028, 2002.

[5] Akbari, H., Kosugi, Y., Kojima, K., and Tanaka, N., “Detection and analysis of the intestinal ischemia using visible and invisible hyperspectral imaging.”, IEEE Transactions on Biomedical Engineering, 57(8), 2011-2017, 2010.

[6] Li, C., Strassl, M., Rauchenzauner, S., and Wintner, E. “Evaluation of LED illumination for dental instruments.”, Lighting Research & Technology, 41(1), 89-97, 2009.

[7] Wang, H., Cuijpers, R. H., Luo, M. R., Heynderickx, I., and Zheng, Z., “Optimal illumination for local contrast enhancement based on the human visual system.”, Journal of biomedical optics, 20(1), 015005, 2015.

[8] Wang, H. C., and Chen, Y. T., “Optimal lighting of RGB LEDs for oral cavity detection.”, Optics express, 20(9), 10186-10199, 2012.

[9] Litorja, M., Brown, S. W., Lin, C., and Ohno, Y., “Illuminants as visualization tool for clinical diagnostics and surgery.”, Advanced Biomedical and Clinical Diagnostic Systems VII, International Society for Optics and Photonics, 7169, 71691B, 2009.

[10] Wang, H. C., Tsai, M. T., and Chiang, C. P., “Visual perception enhancement for detection of cancerous oral tissue by multi-spectral imaging.”, Journal of Optics,15(5), 055301, 2013.

[11] Ito, K., Higashi, H., Ota, Y., and Nakauchi, S., “Spectral-difference enhancing illuminant for improving visual detection of blood vessels.”, 2nd International Conference on Advanced Informatics: Concepts, Theory and Applications (ICAICTA), 1-4, 2015.

[12] Liu, P., Wang, H., Wu, R., Yang, Y., Zhang, Y., Zheng, Z., Li, H.and Liu, X., “Uniform illumination design by configuration of LEDs and optimization of LED lens for large-scale color-mixing applications.”, Applied Optics, 52(17), 3998-4005, 2013.

[13] Kaarna, A., Nishino, K., Miyazawa, K., and Nakauchi, S., “Michromatic scope for enhancement of color difference.”, Color Research & Application, 35(2), 101-109, 2010.

[14] Wang, H., Cuijpers, R. H., Vogels, I. M. L. C., Ronnier Luo, M., Heynderickx, I., and Zheng, Z., “Optimising the illumination spectrum for tissue texture visibility.”, Lighting Research & Technology, 50(5), 757-771, 2018.

[15] Shen, J., Chang, S., Wang, H., and Zheng, Z., “Optimal illumination for visual enhancement based on color entropy evaluation.”, Optics express, 24(17), 19788-19800, 2016.

[16] Hyttinen, J., Fält, P., Jäsberg, H., Kullaa, A., and Hauta-Kasari, M., "Optical implementation of partially negative filters using a spectrally tunable light source, and its application to contrast enhanced oral and dental imaging.", Optics Express, 27(23), 34022-34037, 2019.

[17] 三宅洋一, "分光画像処理入門", 東京大学出版社, 東京, 2006.

[18] S. Prahl, "Optical absorption of hemoglobin," http://omlc.ogi.edu/spectra/hemoglobin/index.html (accessed on December 20, 2014).

[19] Bartczak, P., Čerāne, D., Fält, P., Ylitepsa, P., Hietanen, E., Penttinen, N., Laaksonen, L, Lensu,L., Hauta-Kasari, M.,and Uusitalo, H., "Spectrally tunable light source based on a digital micromirror device for retinal image contrast enhancement.", Lithuanian Journal of Physics, 55(3), 2015.

[20] Liu, P., Wang, H., Zhang, Y., Shen, J., Wu, R., Zheng, Z., Li, H., and Liu, X., "Investigation of self-adaptive LED surgical lighting based on entropy contrast enhancing method.", Optics Communications, 319, 133-140, 2014.

[21] Brown, Steven W., Carlos Santana, and George P. Eppeldauer., "Development of a tunable LED-based colorimetric source.", Journal of research of the National Institute of Standards and Technology 107.4: 363, 2002.

[22] Borges, Marcos E. G., and Lamartine N F Guimaraes. "Generalized extremal optimization algorithm to design a LED-based spectrally tunable light source for star simulation.", Journal of Computational Interdisciplinary Sciences 4.2: 1-12, 2013.

[23] Hsiao, Y. P., Wang, H. C., Chen, S. H., Tsai, C. H., and Yang, J. H., "Identified early stage mycosis fungoides from psoriasis and atopic dermatitis using non-invasive color contrast enhancement by LEDs lighting.", Optical and Quantum Electronics 47.7: 1599-1611, 2015.

[24] Bartczak, P., Gebejes, A., Falt, P., Parkkinen, J., and Silfstein, P., “LED-based spectrally tunable light source for camera characterization.”, Colour and Visual Computing Symposium (CVCS), 1-5, 2015.

[25] Yuan, K., Yan, H., and Jin, S., “LED-based spectrally tunable light source with optimized f itting.”, Chinese Optics Letters, 12(3), 032301, 2014.

[26] Finlayson, G., Mackiewicz, M., Hurlbert, A., Pearce, B., and Crichton, S. “On calculating metamer sets for spectrally tunable LED illuminators.”, JOSA A, 31(7), 1577-1587, 2014.

[27] Ramane, D., and Shaligram, A., “Optimization of multi-element LED source for uniform illumination of plane surface.”, Optics express, 19(104), A639-A648, 2011.

[28] Zhong, P., He, G., and Zhang, M., “Spectral optimization of the color temperature tunable white light-emitting diode (LED) cluster consisting of direct-emission blue and red LEDs and a diphosphor conversion LED.”, Optics express, 20(105), A684-A693, (2012).

[29] Murai,, K. Kawahira, H., and Haneishi, H., “Improving color appearance of organ in surgery by optimally designed LED illuminant.”, World Congress on Medical Physics and Biomedical Engineering, 2012.

[30] Kennedy J, “Particle swarm optimization.”, Encyclopedia ofmachine learning. Springer, New York, 760–766, 2011.

[30] Gono, K., Obi, T., Yamaguchi, M., Oyama, N., Machida, H., Sano, Y., Yoshida S., Hamano Y., and Endo, T., “Appearance of enhanced tissue features in narrow-band endoscopic imaging.”, Journal of biomedical optics, 9(3), 568-578, 2004.

[31] Yamaguchi, H., Saito, T., Shiraishi, Y., Arai, F., Morimoto, Y., and Yuasa, A., "Quantitative study on appearance of microvessels in spectral endoscopic imaging.", Journal of Biomedical Optics, 20(3), 036005, 2015.

[32] McFarlane, R. M., DeYoung, G., Henry, R. A., and McFarlane, R. M., "The design of a pedicle flap in the rat to study necrosis and its prevention.", Plastic and reconstructive surgery, 35(2), 177-182, 1965.

[33] Matsumoto, N. M., Aoki, M., Nakao, J., Peng, W. X., Takami, Y., Umezawa, H., Satoshi, A., Ohashi, R., Naito Z,., and Ogawa, R., "Experimental rat skin flap model that distinguishes between venous congestion and arterial ischemia: the reverse U-shaped bipedicled superficial inferior epigastric artery and venous system flap.", Plastic and Reconstructive Surgery, 139(1), 79e-84e, 2017.

[34] Hsueh, Y. Y., Wang, D. H., Huang, T. C., Chang, Y. J., Shao, W. C., Tuan, T. L., Hughes, M. W., and Wu, C. C., "Novel skin chamber for rat ischemic flap studies in regenerative wound repair.", Stem Cell Research & Therapy, 7(1), 72, 2016.

[35] Kelly, C. P., Gupta, A., Keskin, M., and Jackson, I. T., "A new design of a dorsal flap in the rat to study skin necrosis and its prevention.", Journal of plastic, reconstructive & aesthetic surgery, 63(9), 1553-1556, 2010.

[36] Luo, Ming R., and Li C., "CIECAM02 and its recent developments.", Advanced Color Image Processing and Analysis. Springer, New York, NY, 19-58, 2013.

[37] Luo, M. R., Cui G., and Li, C., "Uniform colour spaces based on CIECAM02 colour appearance model.", Color Research & Application 31.4: 320-330, 2006.

[38] Koschan, M., and Abidi, M., "Digital Color Image Processing.", New York, NY, USA: Wiley, 11-12, 2008.

[39] Zhu, C., Chen, S., Chui, C. H. K., Tan, B. K., and Liu, Q., "Early prediction of skin

viability using visible diffuse reflectance spectroscopy and autofluorescence spectroscopy.", Plastic and Reconstructive Surgery, 134(2), 240e-247e, 2014.

[40] Fält, P., Hiltunen, J., Hauta-Kasari, M., Sorri, I., Kalesnykiene, V., Pietilä, J., and Uusitalo, H. "Spectral imaging of the human retina and computationally determined optimal illuminants for diabetic retinopathy lesion detection.", Journal of Imaging Science and Technology, 55(3), 30509-1, 2011.

[41] Xu, Y., Liu, X., Cheng, L., Su, L., and Xu, X., "A light ‐emitting diode (LED) ‐based multispectral imaging system in evaluating retinal vein occlusion.", Lasers in surgery and medicine, 47(7), 549-558, 2015.

[42] Shrestha, R., and Hardeberg, J. Y., "Multispectral imaging using LED illumination and an RGB camera.", Color and Imaging Conference. Society for Imaging Science and Technology, pp. 8-13, 2013.

[43] Bartczak, P., Fält, P., Penttinen, N., Ylitepsa, P., Laaksonen, L., Lensu, L., Hauta-Kasari, M., and Uusitalo, H., "Spectrally optimal illuminations for diabetic retinopathy detection in retinal imaging.", Optical Review, 24(2), 105-116, 2017.

[44] Bartczak, P., Čerāne, D., Fält, P., Ylitepsa, P., Hietanen, E., Penttinen, N., .. Laaksonen, L., Lensu L., Hauta-Kasari, M., and Uusitalo, H., "Spectrally tunable light source based on a digital micromirror device for retinal image contrast enhancement.", Lithuanian Journal of Physics, 55(3), 2015.

[45] Finlayson, G., Mackiewicz, M., Hurlbert, A., Pearce, B., and Crichton, S. "On calculating metamer sets for spectrally tunable LED illuminators.", JOSA A, 31(7), 1577-1587, 2014.

[46] Giunta, R. E., Holzbach, T., Taskov, C., Holm, P. S., Brill, T., Busch, R., Gansbacher, B., and Biemer, E., "Prediction of flap necrosis with laser induced indocyanine green

fluorescence in a rat model.", British journal of plastic surgery, 58(5), 695-701, 2005.

[47] Feng, S., Chen, J., Wo, Y., Li, Y., Chen, S., Zhang, Y., and Zhang, W., "Real-time and long-time in vivo imaging in the shortwave infrared window of perforator vessels for more precise evaluation of flap perfusion.", Biomaterials, 103, 256-264, 2016.

[48] Zhu, C., Chen, S., Chui, C. H. K., Tan, B. K., and Liu, Q., "Early detection and differentiation of venous and arterial occlusion in skin flaps using visible diffuse reflectance spectroscopy and autofluorescence spectroscopy.", Biomedical Optics Express, 7(2), 570-580, 2016.

[49] Chen, S., Zhu, C., Hoe‐Kong Chui, C., Sheoran, G., Tan, B. K., and Liu, Q., "Spectral diffuse reflectance and autofluorescence imaging can perform early prediction of blood vessel occlusion in skin flaps.", Journal of Biophotonics, 10(12), 1665-1675, 2017.

[50] Chin, M. S., Chappell, A. G., Giatsidis, G., Perry, D. J., Lujan-Hernandez, J., Haddad, A., Matsumine, A., Orgill, D., and Lalikos, J. F., "Hyperspectral imaging provides early prediction of random axial flap necrosis in a preclinical model.", Plastic and reconstructive surgery, 139(6), 1285e-1290e, 2017.

[51] Lee, S. Y., Pakela, J. M., Helton, M. C., Vishwanath, K., Chung, Y. G., Kolodziejski, N. J., McAdams, D. R., Fernandez, D., E., Christian, J. F., and O'Reilly, J., "Compact dual-mode diffuse optical system for blood perfusion monitoring in a porcine model of microvascular tissue flaps.", Journal of Biomedical Optics, 22(12), 121609, 2017.

[52] Zheng, J., Xi, S., Ding, M., Li, H., Xu, W., Tang, M., and Chen, S., "Effects of venous superdrainage and arterial supercharging on dorsal perforator flap in a rat model.", PLoS One, 11(8), e0160942, 2016.

[53] Bajwa, N., Au, J., Jarrahy, R., Sung, S., Fishbein, M. C., Riopelle, D., Ennis D. B.,

Aghaloo, T., St. John M. A., Grundfest, W. S., andTaylor, Z. D., “Non-invasive terahertz imaging of tissue water content for flap viability assessment.”, Biomedical optics express, 8(1), 460-474, 2017.

[54] Li, X., Chen, M., Jiang, Z., Liu, Y., Lu, L., and Gong, X., “Visualized identification of the maximal surgical delay effect in a rat flap model.”, Wound Repair and Regeneration, 27(1), 39-48, 2019.

[55] Pharaon, M. R., Scholz, T., Bogdanoff, S., Cuccia, D., Durkin, A. J., Hoyt, D. B., and Evans, G. R. “Early detection of complete vascular occlusion in a pedicle flap model using quantitation spectral imaging.”, Plastic and reconstructive surgery, 126(6), 1924, 2010.

[56] Yafi, A., Vetter, T. S., Scholz, T., Patel, S., Saager, R. B., Cuccia, D. J., Evans, G. R., and Durkin, A. J., “Postoperative quantitative assessment of reconstructive tissue status in cutaneous flap model using spatial frequency domain imaging.”, Plastic and reconstructive surgery, 127(1), 117, 2011.

[57] Fisher, R. A., “The use of multiple measurements in taxonomic problems.”, Annals of eugenics, 7(2), 179-188. 1936.

[58] Wang, L., Wu, H., Yan, H., Dong, X., He, Z., Ding, J., and Gao, W., “Effect of a nondominant perforator on multiterritory perforator flap survival in rats.”, Microsurgery, 39(5), 441-446, 2019.

[59] Xi, S., Cheng, S., Lou, J., Qiu, L., Yang, Q., Yu, W., Mei, J., and Tang, M., “A preliminary study of the effects of venous drainage position on arterial blood supply and venous return within the conjoined flap.”, Plastic and reconstructive surgery, 143(2), 322, 2019.

[60] Pabst, A. M., Kämmerer, P. W., Krüger, M., Jäger, L., and Ackermann, M., “Vascular architecture in free flaps: Analysis of vessel morphology and morphometry in murine

free flaps.", Microvascular research, 118, 128-136, 2018.

[61] Ichioka, S., Minh, T. C., Shibata, M., Nakatsuka, T., Sekiya, N., Ando, J., and Harii, K., "In vivo model for visualizing flap microcirculation of ischemia‐reperfusion. Microsurgery", Official Journal of the International Microsurgical Society and the European Federation of Societies for Microsurgery, 22(7), 304-310, 2002.

[62] Merz, K., Schweizer, R., Schlosser, S., Giovanoli, P., Erni, D., and Plock, J. A., "Distinct microhemodynamic efficacy of arteriogenesis and angiogenesis in critically ischemic skin flaps.", Microvascular Research, 83(2), 249-256, 2012.

[63] Hashimoto, I., Nakanishi, H., Shono, Y., Yamano, M., and Toda, M., "The features of thrombus in a microvessel injury model and the antithrombotic efficacy of heparin, urokinase, and prostaglandin E1.", Plastic and reconstructive surgery, 111(7), 2307-2314, 2003.

[64] Poole, K. M., McCormack, D. R., Patil, C. A., Duvall, C. L., and Skala, M. C., "Quantifying the vascular response to ischemia with speckle variance optical coherence tomography.", Biomedical optics express, 5(12), 4118-4130, 2014.

[65] Miyamoto, S., Minabe, T., and Harii, K., "Effect of recipient arterial blood inflow on free flap survival area.", Plastic and reconstructive surgery, 121(2), 505-513, 2008.

Figure List

Table List

Publication List

Published papers

Y. Kurabuchi,　K. Murai, K. Nakano, T. Ohnishi,　T. Nakaguchi,　M. Hauta-Kasari, H. Haneishi, “Optimal design of illuminant for improving intraoperative color appearance of organ”,　Journal of Artificial Life and Robotics,　2018.

Y. Kurabuchi, K. Nakano, T. Ohnishi, T. Nakaguchi, M. Hauta-Kasari, H. Haneishi: “Optimization of Surgical Illuminant Spectra for Organ Microstructure Visualization”, IEEE Access, 2019.

Conference papers

Y. Kurabuchi: “Optimal design of illuminant for improving intraoperative color appearance of organs”, The 2nd Finish - Japanese Medical Photonics Symposium, Auditorium, Kuopio, Finland, September, 2018.

Y. Kurabuchi, K. Nakano, T. Ohnishi, T. Nakaguchi, H. Haneishi: “Surgical Illuminant Design for Enhancement of Organ Microcirculation”, WeP4O-03.6, The IEEE International Symposium on Biomedical Imaging (ISBI) 2019, Venice Italy, April, 2019.

Y. Kurabuchi, K. Nakano, T. Ohnishi, T. Nakaguchi, M. Hauta-Kasari, H. Haneishi: “Evaluation of the optimized surgical illuminant for enhancement of blood oxygen saturation”, SPIE Photonics West BiOS 2020, 11229-33, California, USA, February.

Y. Kurabuchi, K. Nakano, T. Ohnishi, S. Akita, M. Hauta-Kasari, H. Haneishi: “Design of a system combining narrow band illuminants and a color camera for early diagnosis of skin flap necrosis”, SPIE Photonics West BiOS 2021, PW21B-BO301-6, California, USA, March, 2021.

倉渕瑶子, 中野和也, 大西峻, 秋田新介, 羽石秀昭: “遊離皮弁壊死の分光解析による早期検出支援に向けた強調光源の設計”, 日本光学会年次学術講演会(Optics & Photonics Japan 2019), 2pF2, 大阪, 12 月, 2019 年.

倉渕瑶子, 中野和也, 大西峻, 秋田新介, 羽石秀昭: 弁壊死領域早期診断のための狭帯域光源・カラーカメラ連動システム設計, 第 39 回 日本医用画像工学会大会, Paper ID: p2-23, オンライン, 9 月, 2020 年.

Acknowledgement

本論文は筆者が千葉大学大学院　融合理工学府　基幹工学専攻　医工学コース　博士後期課程在籍中の研究成果をまとめたものである．本研究を行うにあたり，終始ご指導いただいた同大学フロンティア医工学センター教授　羽石　秀昭　先生に深く感謝申し上げる．また，本論文の学位論文審査を担当していただいた，同大学　フロンティア医工学センター教授　山口　匡　先生，同大学　フロンティア医工学センター教授　林　秀樹　先生，同大学　フロンティア医工学センター教授　兪　文偉　先生　に感謝の意を表す.

医学的見地から貴重なご意見をいただいた同大学　医学部附属病院　形成外科　講師　秋田　新介　先生　に感謝の意を示す.

研究を遂行するにあたる助言や，研究留学時にご支援いただいた University of Eastern Finland School of Computing Professor Markku Hauta-Kasari 先生に感謝申し上げる.

研究を遂行するにあたり，照明機器作製の助言をいただいた同大学　フロンティア医工学センター　教授　中口　俊哉　先生に感謝を申し上げる.

研究を遂行するにあたり，照明機器作製と皮膚固定用チャンバー作成の助言をいただいた同大学　フロンティア医工学センター　技術専門職員　関根　雅　氏に感謝を申し上げる.

研究を遂行するにあたり，日頃より有益な討論，助言をいただいた，宮崎大学 キャリアマネジメント推進機構　テニュアトラック推進室　助教　中野　和也　先生，Memorial Sloan Kettering Cancer Center　Senior Research Scientist 大西　峻　先生に感謝申し上げる.

日頃より，実験や機器作製の補佐，研究の遂行にあたる討論，助言をいただいた，植田 祐未　氏，川崎　真未　氏をはじめとした羽石研究室の皆様に感謝を申し上げる.

最後に，日頃より支えてくれた両親をはじめ，家族の皆様に感謝の意を示す.

2021 年　2 月　倉渕　瑶子